

arXiv:1607.06501v1 [cond-mat.quant-gas] 21 Jul 2016

Momentum Evolution Numerics of an Impurity in a Quantum Quench

Matthew Malcomson

PhD Thesis

Submitted for the degree of Doctor of Philosophy

February 15, 2016



Declaration

Except where stated otherwise, this Thesis is a result of the author's original work and has not been submitted in whole or in part for the award of a higher degree elsewhere.

Acknowledgements

I would like to thank Evgeni Burovski, my supervisor for introducing me to the power of computers in research, it has become the catalyst what is now my overriding interest. Furthermore, I thank Vadim Cheianov, Oleksandr Gamayun, Mikhail Zvonarev and Oleg Lychkovskiy for interesting discussions that have provided new avenues of research.

Abstract

A discussion on the momentum evolution of an impurity interacting via a finite delta potential repulsion with a non-interacting fermionic background gas is presented. It has recently been shown that the momentum evolution of this system displays two interesting features, namely a non-zero thermalised value and a long-lived quantum mechanical oscillation around this plateau named “quantum flutter” [Mathy, Zvonarev, Demler, *Nat. Phys.* **2012**]. We discuss revivals in the momentum of the impurity, which have been seen before but not yet thoroughly investigated. Subsequently it is shown the quantum flutter and revivals are caused by disjoint sets of eigenstate transitions, and this fact is used to interpret some of their aspects. This attribution of momentum features to different eigenstate subsets allows quantitative reproduction of these features with much less computational expense than has so far been possible. Finally some results on the distribution of the momentum of eigenstates and their relation to the momentum of the impurity once the system has been thermalised are presented along with a discussion on the time averaged infinite time value of the momentum and its comparison to different eigenstate subsets.

Contents

| | | |
|----------|--|-----------|
| 1 | Introduction | 19 |
| 1.1 | Introduction | 19 |
| 1.2 | Method and Model | 23 |
| 1.2.1 | Model | 23 |
| 1.2.2 | Method | 37 |
| 2 | Observables of the System | 39 |
| 2.1 | Introduction | 39 |
| 2.2 | Justification | 40 |
| 2.3 | Overall Momentum | 43 |
| 2.4 | Momentum Revivals | 50 |
| 2.5 | Infinite Time | 54 |
| 2.6 | Quantum Flutter | 61 |
| 2.7 | Conclusion | 62 |
| 3 | Eigenstates Responsible For Momentum Features | 64 |
| 3.1 | Introduction | 64 |
| 3.2 | The Pseudo Sea | 65 |
| 3.3 | Eigenstate Families | 66 |
| 3.4 | General Shape | 69 |
| 3.5 | Flutter | 77 |
| 3.6 | Conclusion | 86 |

| | | |
|----------|---|-----------|
| 4 | Other Investigations | 88 |
| 4.1 | Thermalisation | 88 |
| 4.2 | Asymptotic $\langle P_{\downarrow}(\infty) \rangle$ | 91 |
| 4.3 | Conclusion | 94 |
| 5 | Concluding Remarks | 95 |
| 5.1 | Results | 95 |
| 5.2 | Limitations and Further Work | 97 |
| | Appendices | 98 |
| A | Code Details | 99 |
| A.1 | Introduction | 99 |
| A.2 | Data Structures | 100 |
| A.3 | Multiple Processors | 103 |
| A.4 | Improvements | 105 |

List of Figures

- 2.1 The number of states required for a range of saturation values for ς . We show the semi-log plot of how ς changes with the number of states. The progression is linear until a $\varsigma \approx 0.96$, at which point many more states are required to provide further accuracy. 40
- 2.2 The number of states required for a range of saturation values for ς . We show the semi-log plot of how the number of states required for a given ς changes with increasing system size, the progression is not linear, so this is not an exponential relation, but the plot does show a large increase in the number of states required as larger systems are used. 41
- 2.3 a) As ς is increased past 0.9 to 0.999, the main observable change in $\langle P_{\downarrow}(t) \rangle$ is a downwards shift over the entire time range. b) This downwards shift can be normalised out by the value of ς to provide approximate results when the number of states required for a satisfactory ς value is too high. 42

- 2.4 Impurity momentum evolution for multiple system sizes. Plots showing $\langle \widetilde{P}_{\downarrow}(t) \rangle$ over systems of 21, 45, and 99 particles with constant $\gamma = 3$ and constant initial momentum of $Q = \frac{4}{3}k_F$. Until the revival in the impurity's momentum, the evolution of the impurity is identical for all system sizes, the revivals increase in period with a linear progression on the system size (see Fig 2.9), and they are the only finite size effect apparent here. The consistency of the flutter and plateau is in agreement with [69]. In this plot we ensure ς is consistent for $N = 21$ and $N = 45$, however we were unable to match the ς for $N = 99$, so we plot all data once appropriately normalised. When not normalised by the value of ς , the only noticeable difference is a total shift downwards in the entire plot for $N = 99$. 44
- 2.5 $\langle P_{\downarrow}(t) \rangle$ over multiple values of Q , with a fixed system size $N = 45$ and interaction strength $\gamma = 3$. a) While $Q > k_F$, increasing Q decreases both the plateau and time to the momentum revival (see Sections 2.4 and 2.5). b) As Q decreases past k_F , the flutter goes away, which is a central feature of reference [69]. 46
- 2.6 Change in $\langle P_{\downarrow}(t) \rangle$ with γ for fixed system size $N = 45$ and $Q = \frac{4}{3}k_F$. As γ increases, the revival period decreases, the plateau in the momentum decreases, and the flutter frequency increases. The change in the revival periods and the plateau can be qualitatively interpreted as an increase in the momentum transfer to the background gas, while the flutter follows the progression described in Equation (2.3), formed from the argument presented in [69, 70]. 47

| | | |
|-----|---|----|
| 2.7 | The change in $\langle P_{\downarrow}(t) \rangle$ over ς with fixed $N = 99$, $\gamma = 3$ and $Q = \frac{4}{3}k_F$. Here a larger system size than previous is used, as the features which differ with changing overlap are sometimes obscured by finite size effects. As ς increases, the revival period is constant, the flutter frequency increases, and the plateau decreases. The flutter frequency increases with increasing overlap, but reaches a constant value at a ς of about 0.95, while the plateau tends to some value, but has not saturated in the ς range shown. | 48 |
| 2.8 | The change in $\langle \widetilde{P_{\downarrow}}(t) \rangle$ with ς with fixed $N = 99$, $\gamma = 3$ and $Q = \frac{4}{3}k_F$. Of the two features that change with ς , the plateau change can be almost factored out with normalisation. | 49 |
| 2.9 | The progression of the revival period t_{rev} with changing system size N increases linearly, which is in good agreement with Eqn (2.2), and shows how the revivals are a finite size effect, diverging as $N \rightarrow \infty$. This plot was created with $Q = 4k_F/3, \gamma = 3$, but the particulars of how γ is set to its value are important for the prediction of Equation (2.2). We find empirically, that fixing $L/N = 2, g = 3$ gives the best predictions for Eqn (2.2), but for $L/N = 3, g = 2$ (as an example) the estimations are further off. | 51 |

- 2.10 The change with Q of the revival period t_{rev} progresses in a non-trivial manner, mostly following the progression of the momentum plateau (to be shown in Section 2.5, see Figure 2.16). For a low initial momentum $Q < k_F$, the approximation in Eqn (2.2) is very poor, failing to even qualitatively reproduce the progression, but as the initial momentum becomes greater than the Fermi momentum it gives a better prediction. Note the estimated revival periods for $Q = \frac{38}{45}k_F$ are not shown as they are greater than $1000t_F$, once again demonstrating this estimate is not useful for a low initial momentum. As with Figures 2.9 and 2.11, the choice of how to set γ is important for this prediction. The current plot was created with $L/N = 2$ for the red points, and $L/N = 3$ for the blue ones. While in Figures 2.9 and 2.11, the choice of $L/N = 2$ has been shown to be the most accurate for $Q = \frac{4}{3}k_F$, this plot demonstrates a dependence of the optimum choice on the initial momentum Q , though the exact relation is currently unknown. 52
- 2.11 The change in revival period t_{rev} with respect to γ , shows that Eqn (2.2) qualitatively reproduces the progression of the momentum revivals. It should be noted that the revival period plotted for $\gamma = 1$ is highly suspect as the revival is not nearly as clear as other points, having a relative peak spanning $100t_F$, we chose the highest point of this peak, which was near its end. Like in Fig 2.9 and 2.10 the way γ is set has a strong influence on the accuracy of Eqn (2.2), with two example data sets shown, we fix L/N , at 2 for the red points, and 3 for the blue ones. 53
- 2.12 a) A plot of $\langle P_{\downarrow}(t) \rangle$ for many revivals shows how the momentum revivals initially decohere with increasing time, but the plot of very long $t \gg t_{rev}$ in b) shows that despite this, the momentum at very long term values is not completely stable. 56

- 2.13 Both saturation measures have a near linear dependence on the value of ς reached in the calculation, which can be normalised out to find the limit that would be reached for $N_s = \infty$. The gradient of this progression changes with different parameters, but once the overlap is large enough, $\varsigma \gtrsim 0.95$ then the linearity has always been seen to exist. This graph has been plotted for $N = 45$, $\gamma = 3$, and $Q = \frac{4}{3}k_F$ and does not normalise the results by ς 57
- 2.14 Changing time-independent and momentum plateau values with system size for constant $\gamma = 3$ and $Q = \frac{4}{3}k_F$. While the plateau value in the momentum momentum stays constant with system size, the theoretical value is initially much greater than the plateau, and decreases towards it with a power law relation as $N \rightarrow \infty$. Hence, while the momentum of the impurity is not the same as its theoretical thermalised value, this is a finite size effect, and disappears as the system moves into the thermal regime. This fact could be used to obtain an approximate value for the saturation momentum in a thermalised system by finding the plateau of a much smaller system, using less computational resources than otherwise, but measuring the plateau is intrinsically imprecise due to the flutter around it, so this is only useful as an approximation. 58
- 2.15 How the saturation values are modified by interaction strength γ . As γ diverges, the saturation values both converge to a non-zero value, and to each other. The progression of the theoretical infinite time value was discussed in reference [79], and the current plot shows the same progression. While the plateau is independent of the way γ is chosen, $\langle P_{\downarrow}(\infty) \rangle$, like Eqn (2.2) in Section 2.4, does depend on how γ is formed, with the current plot formed for $L/N = 2$. For $L/N = 3$ the values of $\langle P_{\downarrow}(\infty) \rangle$ follow a progression of the same shape, but between those shown in this figure. 59

| | | |
|------|--|----|
| 2.16 | The change with Q of both $\langle P_{\downarrow}(\infty) \rangle$ and the momentum plateau. Once the initial momentum is above k_F , the plateau decreases with increasing Q , while $\langle P_{\downarrow}(\infty) \rangle$ increases. There is a maximum in the momentum plateau for an initial momentum some point below k_F as seen in [69]. The difference between $\langle P_{\downarrow}(\infty) \rangle$ and the momentum plateau increases with initial momentum, showing how the interplay between states becomes more important for the impurity's momentum as the initial momentum goes above k_F . The progression of the plateau matches what is seen in [79], the progression of $\langle P_{\downarrow}(\infty) \rangle$ was not mentioned there. This plot was created fixing $\gamma = 3$ and $N = 45$ | 60 |
| 2.17 | The flutter frequency we see matches what is predicted from Eqn (2.3), to a high accuracy, the error bars on the period seen show the maximum and minimum value measured for the flutter, which come from finite size effects obscuring the flutter. Note there is no “plotted” point for $\gamma = 1$ as the oscillation was completely obscured by the revival (as can be seen in Figure 2.6). Despite these difficulties, the flutter period we see closely follows the prediction from [113]. . . . | 62 |
| 3.1 | The graphical solutions of the Bethe root equations in Eqn (1.15) shows the validity of the representation for the Bethe roots given in Equation (3.2). Each root can be distinguished by the range it is in, and as the gradient of the green line here is fixed by the physical parameters of the system, then the set of ranges in which roots are found uniquely determine the roots themselves. | 66 |

3.2 The plot of eigenstate energy against importance shows some distinct branches. These branches are comprised of parametric families defined by the pseudo hole each related state shares. For all branches other than the main one (at the top of the figure), the branch is composed of a single parametric family, where all related states have the same pseudo hole. The main branch consists of two families, one where the pseudo hole is on the positive edge of the pseudo sea, $n_{hole} = (N-1)/2$, and one where the pseudo hole is on the negative edge, $n_{hole} = -(N+1)/2$. Each successive branch consists of states from a single family, whose pseudo hole is further inside the pseudo sea the less the average $|\langle FS|f_Q\rangle|^2$, as schematically shown in the top left hand corner. The most important states shown here have a single pseudo excitation, and as a single parametric family is followed from left to right, the pseudo particle is increased by one for each element, the energy of each state being the sum of the squares of Bethe roots z_i where $0 \leq n_i - z_i \leq 1$ 68

3.3 The Fourier transform of the impurity's momentum with inset showing which state pairs cause each small peak. The main plot shows the Fourier transform of the impurity's momentum against time. Each point here is a contribution from a single state pair to the total $\langle P_{\downarrow}(t) \rangle$. There are two strong features, the large peak at $\omega = 0$ and the set of negative amplitude peaks around each integer multiple of the revival frequency. Inset shows all states with a single pseudo excitation on the same axis as Figure 3.2 (more clearly showing the branches discussed previously), the coloured arrows show example state pairs for some of the coloured peaks in the main plot. In all state pairs from the coloured peaks, both states are in the main family (those not coloured grey), with a pseudo hole of $(N-1)/2$, so the difference between state pairs is only in the difference between the pseudo particles of each state in the pair. Transitions which give the contributions in the first negative peak of the Fourier transform are between states whose pseudo particles differ by one, while transitions causing the second peak are between states whose pseudo particles differ by two. This pattern continues for all the different peaks. 70

| | | |
|-----|---|----|
| 3.4 | The contribution to $\langle P_{\downarrow}(t) \rangle$ from each negative amplitude peak in the Fourier transform. The main plot shows the Fourier transform of the momentum, highlighting each negative amplitude peak, while the inset compares the contribution of each of these peaks to the total momentum evolution of the impurity. The colour of each contribution in the inset correlates with the corresponding colour of the peak in the Fourier transform, and these contributions are plotted on an axis of the same scale, but shifted for clarity. Each peak adds a wave almost harmonic to the revival frequency, and Figure 3.5 shows that their superposition describes both the plateau and the revivals. Figure 3.5 shows this superposition of all peaks describes the general shape of the total $\langle P_{\downarrow}(t) \rangle$, but does not describe the flutter. Figure 3.6 demonstrates the contribution from these peaks to the plateau value of the total momentum is proportional to the ς value reached when just accounting for the eigenstates whose transitions form these peaks. | 71 |
| 3.5 | Comparison of $\langle P_{\downarrow}(t) \rangle$ to the contribution from all transitions between states in the main parametric family, which is equivalent to the contribution from all peaks seen in the Fourier transform. This comparison shows how this limited number of transitions describes the majority of features in $\langle P_{\downarrow}(t) \rangle$, their contribution provides the majority of the revival amplitude, and there is a non-zero plateau in the momentum. There are notable differences though: the plateau is not at the same momentum as the plateau of the total momentum, and there is no quantum flutter around it. | 72 |

| | | |
|-----|--|----|
| 3.6 | Comparison between the normalised contributions of the main parametric family, main branch in Figure 3.2, and all states calculated for a typical system. The normalised branch reproduces the plateau of the entire $\langle P_{\downarrow}(t) \rangle$ quite well, while the main parametric family does not. Both the normalised contributions from the main family and main branch have a greater revival amplitude than the actual $\langle P_{\downarrow}(t) \rangle$, demonstrating that they contribute relatively more to the momentum revivals than other states. | 74 |
| 3.7 | Comparison between the normalised contributions of each branch from Figure 3.2 and the total momentum contribution. Each contributes a similar shape to the momentum, though without the normalisation of each branch the shape of most would not be visible here. The gradual increase in the revival period can be attributed to the fact that the less important branches seen in Figure 3.2 have points closer together on the energy axis. | 75 |
| 3.8 | Comparison of the approximations gotten from normalising the main branch contribution via Equation (2.1) to that of adding the time-independent contribution of other states to the full contribution of the main branch. Accounting for the time-independent contributions of all states provides a better approximation around the momentum revivals. | 76 |
| 3.9 | Plot comparing the quantum flutter in the total momentum evolution with the contributions to the momentum from transitions between state branches, and contributions from transitions between states in different branches, but sharing a pseudo particle as highlighted in Figure 3.10. The total quantum flutter is reproduced by all inter-branch transitions, and the restricted set of transitions between states sharing a pseudo particle reproduces the frequency, and most of the amplitude of the flutter. | 78 |

- 3.10 All singly excited states with a $|\langle FS|f_Q\rangle|^2$ above a certain threshold.
Some parametric families different to the type discussed before are highlighted in colours other than dark blue. In these parametric families, related states share a pseudo particle and have different pseudo holes. To avoid confusion, we will not refer to these sets as parametric families in the text. Intra-family transitions from these families create the major contribution to the quantum flutter in $\langle P_\downarrow(t) \rangle$. While one family of the type described in Figure 3.2 clearly contributes more to $\langle P_\downarrow(t) \rangle$ than others, the contributions of the families shown here are relatively similar, and we cannot isolate a single one as providing the main contribution to the flutter. . . . 79
- 3.11 The plot of the imaginary and real parts of the terms in Eqn (1.19) for those state pairs found to be major flutter contributors. a) While the contributions with the greatest amplitude are far from the flutter frequency, there is a strong peak around that frequency coming from state pairs where one state is excited from the negative edge of the pseudo sea. b) For a small initial momentum $Q < k_F$, the structure of the Bethe Ansatz means states excited from the negative edge with a positive particle can't exist, so the branches are lost. In both plots, the red radial line denotes the flutter frequency. . . . 81
- 3.12 Comparison of the contribution from all state pairs sharing a pseudo particle, to the further subset of these state pairs where one of the states has its pseudo hole as the negative edge of the pseudo sea. The oscillation that relates to the flutter is the same between these two subsets, sharing both the amplitude and frequency. This shows how the state pairs contributing to the flutter in the subset of state pairs who share a pseudo particle all have one state from the negative edge of the pseudo sea. 82

| | | |
|------|---|----|
| 3.13 | Comparison of the unnormalised total momentum evolution of the impurity to the momentum evolution that comes from assuming the only time-dependent contributions come from transitions between states with a single pseudo excitation. While the plateau of the approximation is not as level as the total, the majority of all features are shown, with both the flutter and revivals presenting good approximation in both amplitude and frequency. | 84 |
| 3.14 | The plateau values of different approximations and their progression with the initial momentum Q . We can see that the approximation from normalising a subgroup defined via pseudo excitation patterns becomes progressively less accurate as the initial momentum of the impurity decreases. On the other hand, the approximations from taking account of the time-independent contributions of all states still provides a reasonable plateau value. Moreover, normalising the contribution found from only obtaining a saturation of $\varsigma = 0.95$ also provides a reasonable plateau over all initial momenta Q | 85 |
| 3.15 | Comparison of $\langle P_{\downarrow}(t) \rangle$ to the sum over transitions between the two main state pair contributors identified. The inclusion of all transitions between states in the main branch matches the overall shape of the momentum evolution, while the inclusion of those transitions between states excited from the negative edge of the pseudo sea and those which share a pseudo particle with them, add flutter to the plot. The approximate flutter does not reproduce the same amplitude as the total, and the value of the momentum plateau is not matched, but the frequency of the revivals and flutter are accurately reproduced. In this graph, the total plot required calculating 400000000 state pairs, while the approximate value required calculating only 11865 state pairs, a computational speedup of about 4 orders of magnitude. | 87 |

- 4.1 Distribution of each state's momentum contribution, and the weight that contribution has. This plot is limited to states that are singly excited for clarity, as the structure in states with extra excitations can't be seen at this scale. The red line shows the time-independent contribution of all states, and the green line denotes the plateau seen in the momentum. While there are states that have the momentum which would occur at infinite time (whichever of the two definitions we use), there is no obvious feature in the distribution around this point. 90
- 4.2 Contribution to infinite time momentum from singly excited states. Each bar is the sum of the $|\langle FS|f_Q\rangle|^2$ for the states in that region, the red vertical line denotes the infinite time contributions from all states, and the green line denotes the position of the plateau seen when the total momentum against time is plotted. While the contributions increase markedly near the upper bound on the momentum, the peak is slightly beforehand. There are two apparent contributions: one from the progression of the most important family, and one from others, but both have a peak at the same point. 91
- 4.3 Distribution of the singly excited states across their expectation values of the impurity's momentum. Each bar represents the number of states within that region of momentum, the red vertical line denotes the infinite time contributions, and the green line denotes the position of the plateau when the total momentum against time is plotted. The momentum of these states is bounded in both directions, and there are more states near these bounds than elsewhere. While the number of states with negative momentum is greater than those with positive momentum, the $|\langle FS|f_Q\rangle|^2$ weights mean the contribution from positive momentum states is much greater (see Fig 4.2). 92

| | | |
|-----|--|----|
| 4.4 | How the normalised time-independent contributions to the momentum from the main family compare with the total as the system size changes. For those systems which we can plot the time evolution of the momentum (with $N < 100$), the infinite time contributions of the main branch are almost representative of the total, and their representative nature increases with increasing system size. For larger systems, outside of this calculable range, the infinite time contribution of the main branch decreases further, away from the total. An analytical analysis shows that this progression continues, and as the system size diverges, the main branch's contribution tends to zero [135]. | 93 |
|-----|--|----|

| | | |
|-----|--|-----|
| A.1 | Schematics of data structures serialised for both large and small systems. For small systems a hash table containing all data required for analysis was directly serialised to disk and unserialised when required. This had the advantage of simplicity, and would not easily result in un-synchronised data, as the calculation stage created the data in one step, and no modifications are needed in the analysis stage. Frequencies, amplitudes, and eigenstate pairs are kept ordered by increasing energy, and can hence be matched accordingly, this means only information required for choosing interesting states is needed in the state pairs. When the system is large, storing all data in RAM at the same time in the analysis stage is impossible, so a different method of reading in data was devised (see Figure A.2). Said method centred around calculating the position in the stored amplitude matrix where each interesting eigenstate pair will be, and only reading the data stored in those positions. As this new method of reading those amplitudes required for partial contributions took time and required the calculation of each eigenstates' energies, storing the frequencies associated with each amplitude became redundant, and was removed for storage space concerns. | 102 |
| A.2 | Schematic of how work is spread over multiple processors, in this example 3 processors are used. The distribution of work across multiple processors is done in a simple manner; each processor takes a block of the amplitude matrix and calculates the contribution to the RHS of Equation (1.19) for a set of time points. Each of these contributions is then summed, and taken from the total momentum of the system Q to find the momentum of the impurity over the range in time calculated over. | 104 |

A.3 Alternate order of amplitude matrix. Currently amplitudes of contributions are stored ordered by the energy of the eigenstates in each transition shown in Figure A.2. If the matrix were ordered by $|\langle FS|f\rangle|^2$ instead, then finding the amplitudes for a smaller subset of eigenstates, taken in this order, would be much simpler. This would mean finding the contribution from a smaller set of eigenstates could be done without recalculation of their amplitudes. . . 106

Chapter 1

Introduction

1.1 Introduction

When introduced to a new phenomenon, a natural tendency is to attempt to find the simplest system in which it is exhibited, and use said system as a playground to explore the phenomenon's features without unnecessary complexity. An ever-present danger in this methodology is that a simple system may show qualitatively different features to more complex ones, for example, because features in the complex system are emergent from some complexity not in the smaller system, or because the limitation on the degrees of freedom in the smaller system prohibit the phenomenon. Upon encountering this, the investigator must decide whether to add complications piecemeal to their original description, focus on those features which are shared by the model and observations, or start from scratch with a different model. It is a rare, but happy, event when the features of said simple model opens up a new and exciting area of research, from which novel features are found with regularity. The physics of strongly correlated one-dimensional quantum systems is one such field, revealing numerous phenomena not present in higher dimensions, both in their mathematical descriptions and their observable nature. While initially thought of more as a testing ground for methods to apply to the “real” 3 dimensional world (see the introductions of references [1, 2] for examples), experimental progress creating 1D systems (both quasi and true) has given

these “toy models” new-found experimental relevance [3–27], that has significantly increased the interest in the field.

One of the most important aspects of one-dimensional physics is the Luttinger liquid universality class. While many different microscopic models have been used in 1D, for both fermions and bosons, and across a wide range of interaction types and potentials, [28–30] [2, 31, 32] [33–35] [32, 36, 37] [38] most one dimensional models share common features at low energy, and from this, a low energy universality class, called a “Luttinger Liquid”, has been formed, which is in some ways a replacement for the Fermi liquid theory in one dimension [39–41]. In one dimension the limitation in dimensionality imposes an inherently collective nature on the excitations of a liquid, as in order for one particle to move, another must make space. This breaks the fermionic quasiparticle approximation of a Fermi liquid, and in its place a bosonic quasiparticle of collective excitations is created. Non-interacting bosonic quasiparticles are formed by assuming a linear excitation dispersion of the fermionic particles [29], and a small non-linearity can be accounted for by adding interactions between them [39]. Initially formulated to describe fermions, the generality of this description has extended to gases of bosons [42], creating a general description of low energy one-dimensional systems. Despite the success of this Luttinger liquid theory, the analogy does not carry over to higher energy excitations, which allow excitations too far from the approximately linear dispersion to be accounted for.

Given such a widely encompassing description of the low energy physics in one-dimensional systems, an interest in systems outside the Luttinger liquid paradigm has emerged, focusing on systems at a higher energy, or with some other feature breaking the linear approximation of the dispersion relation [43–48]. One method of probing these regimes, is by going back to the microscopic models that have been formed, and finding how they behave as excitations move them away from the Luttinger liquid paradigm. It is one of the miracles of one dimension that many of these models can be solved exactly using the ansatz proposed by Bethe, initially

in order to find a solution of the Heisenberg spin-1/2 chain [49]. This ansatz gives exact eigenstates of the systems, and enables numerical calculation of their energy and momentum [41, 50].

This thesis works on one particular system of this type, modelling the dynamics of a high energy spin impurity quenched in a spin polarised fermionic gas, presenting a discussion on the features of the impurity's momentum evolution, and the patterns in the eigenstate transitions that describe individual features. An impurity in one-dimensional systems has been an active area of research for some time [20, 25, 26, 51–68], and modelling how a system behaves with a high energy impurity, taking it far away from the Luttinger liquid paradigm is an interesting variation on a theme that has already provided qualitatively new phenomena [69, 70]. The interaction between our impurity and background particles is described by a delta function potential, and hence the system is modelled by the fermionic Yang-Gaudin model [36, 71, 72] spin polarised but for a single impurity, as used in references [69, 73–77]. As a consequence of yet another quirk of a single dimension, this system behaves similarly whether the particles are free fermions or infinitely repulsive bosons, and hence could also be described with the Lieb-Liniger model [33] of interacting bosons in the limit of infinite potential and with added terms for an impurity. This fermionisation of bosons has been directly observed in references [10, 12], and while no exact realisation of this system has been created as yet, reference [20] has demonstrated many necessary ingredients, measuring the velocity of a single impurity accelerated with a constant force, using time-of-flight measurements.

The rest of this thesis is structured in the following way: Chapter 1.2 describes the model used to probe the system and its solutions, some terminology for different equations, and the difficulties faced when calculating the impurity's momentum. The time dependent features of this momentum are presented in Chapter 2, which adds to the existing literature with a deeper analysis of the momentum revivals in the system. Further original work is presented in Chapter 3, which attributes

each momentum feature to a subset of eigenstate transitions, and Chapter 4 which presents the results of a preliminary look at the structure inherent in the eigenstates themselves. Finally, Chapter 5 summarises the main results of this work and presents some proposed topics of further work. A discussion on the technical aspects of the code written for this work is presented in Appendix A.

1.2 Method and Model

1.2.1 Model

The system we work within has two valid representations: one of hard-core bosons, and one of free fermions. In the bosonic case, our Hamiltonian, in units of $\hbar = 1$ and $m = m_{\uparrow} = m_{\downarrow} = 0.5$ is

$$H = \hat{P}_{\downarrow}^2 + \sum_{i=1}^N \hat{P}_i^2 + g \sum_{i=1}^N \delta(x_i - x_{\downarrow}) + a \sum_{i,j=1}^N \delta(x_i - x_j) \quad (1.1)$$

where \hat{P}_{\downarrow} is the momentum operator of the impurity, the sums are over all particles in the background gas, \hat{P}_i is the momentum operator for a single background gas particle, g defines the interaction strength between the impurity and the background gas, and a sets the interaction strength between two particles of the background gas.

For the specific case of our system, $a = \infty$, and it is this infinite potential which is the root cause of the equivalence between representations. While we are using a delta potential interaction, the correspondence holds for a gas of bosons with any interaction, as long as the interaction has an impenetrable core, forcing a constant order on the particles [78]. Essentially, the correspondence comes from the fact that multiplying a fermionic wavefunction by the unit anti-symmetric function

$$\prod_{j>l} \text{sign}(x_j - x_l) \quad (1.2)$$

produces an eigenfunction of the Hamiltonian that obeys bosonic anti-commutation relations and can be made to satisfy the same boundary conditions (depending on the parity of the number of particles). The Pauli exclusion principle, and discontinuities in the anti-symmetric function above do not cause a problem when satisfying regularity conditions because of the stipulated hard-core interactions between bosons, which require the wavefunction to be 0 when two particles share a position. Both representations share many observables (including the energy of

the system), with the determining factor whether the unit anti-symmetric function above commutes with the corresponding operator. This argument can be extended to the case of a gas with a single distinguishable impurity, as the impurity puts no extra constraints on the symmetry of the wavefunction [79]. Recent experiments have managed to record gases in this regime [7, 8, 10], called a Tonks-Girardeau gas, and have even observed the transition between a bosonic state and the Tonks-Girardeau gas with increasing interaction strength [12].

Of these two representations, we use the fermionic one (called the Yang-Gaudin model) throughout. This fermionic description gives us some important values, like the Fermi momentum, which is useful in the phenomenological description of the impurity's momentum, and Fermi time, useful to describe the motion of the impurity in a manner independent of the system size. In this case, there is no interaction between pairs of similar particles, only between the single impurity and each particle in the background gas, so the Hamiltonian is

$$H = \hat{P}_{\downarrow}^2 + \sum_{i=1}^N \hat{P}_i^2 + g \sum_{i=1}^N \delta(x_i - x_{\downarrow}). \quad (1.3)$$

A *dimensionless* interaction strength parameter $\gamma = g/2n$ (where $n = N/L$ is the density of particles in the system) can be defined to use in place of g , which gives a more physically relevant parameter to inspect in Chapter 2.

This model is integrable, and exactly solvable via the Bethe Ansatz [73, 80], we use an alternate formalism presented in ref [75] which has been previously used to good effect in calculating the spectral properties of the system [76] and the momentum of the impurity and background gas in the system [69].

Bethe Ansatz

Soon after the formulation of quantum mechanics, Hans Bethe discovered a method to find the exact eigenstates and eigenvalues of the Heisenberg model for one-dimensional chain of spin-1/2 fermions [49]. As this model only accounts for interactions between neighbouring particles, he noted that when no two down spins

were next to each other the eigenstate must be a linear combination of single down spin wavefunctions. He used this observation to propose an Ansatz for the form of the eigenstates of the system, and showed that when this wavefunction satisfies a set of equations now known as the Bethe equations, his Ansatz indeed solves the Hamiltonian [49].

Bethe’s paper showed that the many-particle problem of the Heisenberg chain reduced to solving how two spin-down quasiparticles interact when upon neighbouring sites [49]. This fact allows all interactions to be interpreted as multiple two-body interactions, which has been suggested as a criterion for integrability [81]. Hence the Bethe Ansatz is intrinsically tied with integrability, and indeed almost all integrable systems can be solved in terms of the Bethe Ansatz [82]. While this statement holds, the applicability of the Bethe Ansatz to most integrable systems was not initially seen, and required slightly different forms to be realised.

The first alternate use came in the 1960’s when Bethe’s hypothesis was applied to the continuum case of a 1D model of interacting bosons [33, 34, 36, 73]. This use, known as the coordinate Bethe Ansatz, is the form used for the current work and is such described in more detail in Section 1.2.1. The coordinate Bethe Ansatz draws a parallel between the down spin quasiparticles of Bethe’s original work and the physical bosons in the 1D gas that Lieb and Liniger studied.

After that more applications and generalisations appeared. The more complicated *nested* Bethe Ansatz was used to account for the additional spin degree of freedom in the non-polarised fermionic 1D gas [36, 37, 71, 83]. For an non-polarised gas, the symmetry between all orderings of particles is broken so there are many different orderings, the number depending on number of each spin. Because of this extra degree of complexity a generalised Bethe Ansatz is used and solved using a set of conditions distinct yet still related to those in Eqn (1.14). Finally an alternate derivation of the Bethe equations called the *algebraic* Bethe Ansatz was found applicable to integrable systems of quasiparticles above some reference state [84–87].

While we use a fermionic gas system, the nested Bethe Ansatz is not used, as gas is polarised apart from the single impurity.

Since it's inception, the Bethe Ansatz has been found useful in many situations, but as one author notes [88] “numerous publications have been dedicated to the subject, so that it is becoming difficult to make exhaustive citations”. Instead we provide the reader with some previously collated references in the introduction of Reference [89].

Bethe Ansatz Solution

For a description of how the Bethe Ansatz is used in our system, we first present a work-through of the coordinate Bethe Ansatz for a two-body example of our system then state the generalisation with a more simple representation used in references [69, 75, 76]. Finally we work through the computationally efficient matrix equations developed in [69] to calculate the momentum of the impurity.

In essence, the coordinate Bethe Ansatz uses the fact that given a suitable inter-particle potential, the wavefunction of the system in the asymptotic limit can be described by the wavefunction of free particles when said particles are far enough apart. For example, for two particles, at positions x_1, x_2 the wavefunction when they are far enough apart from each other is

$$\Psi(x_1, x_2)_{asymptotic} = \alpha e^{i(k_1 x_1 + k_2 x_2)} + \beta e^{i(k_2 x_1 + k_1 x_2)} \quad (1.4)$$

where x_i, k_i are the position and momentum respectively of particle i , and the energy of this wavefunction is

$$E = k_1^2 + k_2^2. \quad (1.5)$$

Within this assumption, any interaction must be accounted for in the coefficients α and β , which are found using restrictions imposed by the inter-particle potential and boundary conditions. While this ansatz is clear in the two-body case, it has also been found correct when generalising to many particles for multiple two

body potentials, as in one-dimension, interactions between multiple particles can be shown to be non-diffractive. This non-diffractive nature is the criterion as mentioned above for the Bethe Ansatz where the interaction between multiple particles can be described as a set of subsequent two-body scattering events.

Reference [73] used a more general form of this ansatz to find the exact eigenstates for the system that we are using, asserting the asymptotic wavefunction in all configurations where the impurity does not share a position with any particle in the background gas. Here we follow that method for a two body system, that is one impurity at position x_1 and one background fermion at position x_2 . In this system, there are two different regions in which the wavefunction must have its asymptotic form, one where $x_1 < x_2$ and one where $x_1 > x_2$, hence

$$\Psi(x_1, x_2) = \Psi_1(x_1, x_2) + \Psi_2(x_1, x_2) \quad (1.6)$$

where Ψ_1, Ψ_2 describe the wavefunction in their respective region, and are of the same form as before. Due to periodic boundary conditions on x_2 , we know the wavefunction when $x_2 = L$ must be the same as when $x_2 = 0$, hence

$$\begin{aligned} \Psi_1(x_1, L) = \Psi_2(x_1, 0) &\implies \alpha_1 e^{i(k_1 x_1 + k_2 L)} + \beta_1 e^{i(k_2 x_1 + k_1 L)} = \alpha_2 e^{ik_1 x_1} + \beta_2 e^{ik_2 x_1} \\ &\implies \\ \alpha_1 e^{ik_2 L} &= \alpha_2 \\ \beta_1 e^{ik_1 L} &= \beta_2 \end{aligned} \quad (1.7)$$

similarly, applying the same boundary conditions to x_1 we have the conditions

$$\begin{aligned} \Psi_1(0, x_2) &= \Psi_2(L, x_2) \\ &\implies \\ \alpha_1 &= \alpha_2 e^{ik_1 L} \\ \beta_1 &= \beta_2 e^{ik_1 L} \end{aligned} \quad (1.8)$$

which together imply that

$$k_1 + k_2 = \frac{2\pi n}{L}, \quad n \in \mathbb{N} \quad (1.9)$$

where the value $\frac{2\pi n}{L}$ is hence the total momentum of the system.

To account for the delta function interaction potential, we assert the condition [73]

$$\frac{1}{2} \left[\left(\frac{\partial}{\partial x_1} - \frac{\partial}{\partial x_2} \right)_{x_1-x_2=0^+} - \left(\frac{\partial}{\partial x_1} - \frac{\partial}{\partial x_2} \right)_{x_1-x_2=0^-} \right] \Psi = g\Psi \quad (1.10)$$

which, using the split of Ψ depending on the relative positions of each particle, implies the following

$$\left(\frac{\partial}{\partial x_1} - \frac{\partial}{\partial x_2} \right) \Psi_1(x_1, x_2) - \left(\frac{\partial}{\partial x_1} - \frac{\partial}{\partial x_2} \right) \Psi_2(x_1, x_2) = 2g\Psi \quad (1.11)$$

where g is the interaction strength from Equation (1.3). We can combine the requirements found in Equations (1.7) and (1.8) with the one above to form the combined requirement below.

$$\begin{pmatrix} e^{ik_2 L} \alpha \\ e^{ik_1 L} \beta \end{pmatrix}_1 = \begin{pmatrix} \alpha \\ \beta \end{pmatrix}_2 = \begin{pmatrix} 1 + g/i(k_1 - k_2) & g/i(k_1 - k_2) \\ -g/i(k_1 - k_2) & 1 - g/i(k_1 - k_2) \end{pmatrix} \begin{pmatrix} \alpha \\ \beta \end{pmatrix}_1 \quad (1.12)$$

which requires for self-consistency that

$$\begin{vmatrix} 1 + g/i(k_1 - k_2) - e^{ik_2 L} & g/i(k_1 - k_2) \\ -g/i(k_1 - k_2) & 1 - g/i(k_1 - k_2) - e^{ik_1 L} \end{vmatrix} = 0. \quad (1.13)$$

In order to satisfy the above condition, it is sufficient to require that

$$\begin{aligned} \cot\left(\frac{k_1 L}{2}\right) &= \frac{2k_1}{g} - \text{const} \\ \cot\left(\frac{k_2 L}{2}\right) &= \frac{2k_2}{g} - \text{const} \end{aligned} \quad (1.14)$$

where *const* is some arbitrary value. Finding an eigenstate of the system is hence reduced to finding 2 values k_1, k_2 which satisfy the equations (1.14), and (1.9), where the energy of the state is given by (1.5). This solution can be generalised to any number of background particles using the assertion that when no background particle shares a position with the impurity, the wavefunction of the system is a linear combination of free particles and accounting for interactions in the way described above [73]. In this more general solution, with a background gas of N particles, the eigenstates of the system are defined by the $N + 1$ values k_1, k_2, \dots, k_{N+1} satisfying the more generalised versions of Equations (1.14), and (1.9) presented alongside the energy of these states below

$$\begin{aligned} \sum_{i=1}^{N+1} k_i &= \frac{2\pi n}{L} = Q, \quad n \in \mathbb{N} \\ \cot\left(\frac{L}{2}k_i\right) &= \frac{2k_i}{g} - \text{const} \\ E &= \sum_{i=1}^{N+1} k_i^2 \end{aligned} \tag{1.15}$$

for all $i \in 1, 2, \dots, N + 1$, and with N representing the number of particles in the background gas. These values k_1, k_2, \dots, k_{N+1} are known as the Bethe momenta of the equation and in our case (with a repulsive potential) they are real.

While this solves the system exactly, it results in a very complicated wavefunction, with many different amplitudes to calculate. Reference [75] found the same wavefunctions were reproduced in an easier format, by forming them in the reference frame of the impurity. In this alternate reference frame, an ansatz is taken to be

$$f(y_2, \dots, y_{N+1}) = \det_N(\Phi_j(y_l)) \tag{1.16}$$

where y_i are the coordinates of each background gas particle in this new frame of reference, and Φ_j are functions dependent on an individual coordinate. Coordinates of this wavefunction span from y_2 onward as the dependence of the function on the position of the impurity has been factored out when switching reference

frame. This new ansatz can be shown [75] to solve the system when each $\Phi_j(y)$ is described as

$$\Phi_j(y) = \sum_{t=1}^{N+1} a_j^t e^{ik_t y} \quad (1.17)$$

where the $N + 1$ k_t values satisfy the conditions in Equation (1.15), and the $N(N + 1)$ coefficients a_j^t satisfy the equations

$$\begin{aligned} \sum_{t=1}^{N+1} a_j^t (1 - e^{ik_t L}) &= 0, & j = 1, \dots, N \\ \sum_{t=1}^{N+1} a_j^t [ik_t (1 - e^{ik_t L}) - g] &= 0, & j = 1, \dots, N \end{aligned} \quad (1.18)$$

to ensure the wavefunction satisfies restrictions from the periodic boundary conditions and the delta potential in the Schrödinger equation respectively. This is the form of eigenstates used throughout the current work.

Equations for Momentum

This work focuses on the time evolution of the impurity's momentum, which we calculate using the computationally efficient equations described in [79]. That reference describes in detail both the derivation of equations to find the impurity's momentum in terms of matrix elements, and a manner to calculate said matrix elements. Here we state the equations which define the impurity's momentum in order to set the scene for the discussion on separation of contributions in Chapter 3. The expectation value of the impurity's momentum can be found with the equation

$$\langle P_{\downarrow}(t) \rangle = Q - \sum_{f_Q, f'_Q} e^{it(E_f - E_{f'})} \langle FS | f_Q \rangle \langle f_Q | P_{\uparrow} | f'_Q \rangle \langle f'_Q | FS \rangle. \quad (1.19)$$

Here the sum is over all eigenstates f described above, which have been given a subscript of Q to highlight the fact that they depend on the total momentum of the system. This total momentum is equal to the initial momentum of the impurity

as the system has evolved from an initial state consisting of the impurity at said momentum and a Fermi sea at $0K$. The fermionic gas state alone is represented as $|FS\rangle$ in the above equation. The energy E_f of the system is for each different eigenstate, and can be found with the equation given in (1.15) for each eigenstate f_Q . In the limit $t \rightarrow \infty$, the dependence of Eqn (1.19) on E_f is removed through time averaging, becoming

$$\langle P_{\downarrow}(\infty) \rangle = Q - \sum_{f_Q} \langle FS | f_Q \rangle \langle f_Q | P_{\uparrow} | f_Q \rangle \langle f_Q | FS \rangle \quad (1.20)$$

which finds the infinite time momentum of the impurity by only having to calculate a single sum over eigenstates, instead of the double one required for Eqn (1.19).

Within this equation there are two non-trivial values to calculate. The first is the overlap of the eigenstate with the original Fermi sea, the other is the matrix element of the background gas momentum operator between the two Bethe eigenstates. For this work, the overlap values and diagonal matrix elements of the background gas momentum operator were calculated using a pre-existing program [90], which uses the equations found in references [76, 79] that we describe below. The code to calculate off-diagonal matrix elements was written by the author, and combined with the above code into the repo [91].

In order to calculate either values numerically, a normalisation constant for the eigenstates in Equation (1.16) must be found. This is done first finding the dot product of an eigenstate with itself

$$\langle f_Q | f_Q \rangle = \frac{Y_{f_Q} Y_{f_Q}}{N!} \int_0^L dx_1 \cdots dx_N \det_N(\overline{\Phi_j}(x_l)) \det_N(\Phi_j(x_l)) \quad (1.21)$$

where Y_{f_Q} is the normalisation constant of the eigenstate f_Q . Using the identity

$$\begin{aligned} \frac{1}{N!} \int_0^L dx_1 \cdots dx_N \det_N [\psi_j(x_l)] \det_N [\Phi_j(x_l)] \\ = \det_N \left[\int_0^L dy \psi_j(y) \Phi_l(y) \right] \end{aligned} \quad (1.22)$$

valid for any functions Φ_j, ψ_j , Equation (1.21) can be written

$$\langle f_Q | f_Q \rangle = Y_{f_Q} Y_{f_Q} \det_N \left[\int_0^L dx \overline{\Phi_j}(x) \Phi_l(x) \right]. \quad (1.23)$$

Using the same choice of a_j^t for Eqn (1.17) as references [69, 76], $\Phi_j(x)$ can be written as

$$\Phi_j(x) = \frac{1}{\sqrt{L}} \left[e^{i(k_j x + \delta_j)} - \frac{\theta_j}{\Theta} \sum_{t=1}^{N+1} e^{i(k_t x + \delta_t)} \right]. \quad (1.24)$$

Inserting equation (1.24) into equation (1.21) and solving for Y_{f_Q} , we get

$$|Y_{f_Q}|^{-2} = \frac{1}{\Theta^2} \left(\sum_{t=1}^{N+1} \frac{\theta_t^2}{1 + \theta_t^2} \right) \prod_{t=1}^{N+1} (1 + \theta_t^2). \quad (1.25)$$

Where the convenience variables θ, Θ are defined below

$$\frac{L}{2} k_j = n_j \pi - \delta_j \quad (1.26)$$

$$\theta_j = \sqrt{\frac{8}{gL}} \sin(\delta_j) \quad (1.27)$$

$$\Theta = \sum_{t=1}^{N+1} \theta_t. \quad (1.28)$$

For singular eigenstates, where $\delta_j = 0$, $j = 1, \dots, N$, we have the relation

$$\lim_{c \rightarrow -\infty} \frac{\theta}{\Theta} = \frac{1}{N+1} \quad (1.29)$$

which implies

$$Y_{f_Q} = \sqrt{N+1}. \quad (1.30)$$

The equation to calculate the overlaps $\langle FS | f_Q \rangle$ in Eqn (1.19) is taken from reference [79], and restated below

$$\langle FS | f_Q \rangle = Y_{f_Q} \det_N \chi \quad (1.31)$$

where χ is an $N \times N$ matrix whose elements are defined by

$$\chi_j^l = \frac{\theta_l}{\sqrt{a}} \left[\frac{1}{u_j - \frac{L}{2}k_l} - \frac{1}{\Theta} \sum_{t=1}^{N+1} \frac{\theta_t}{u_j - \frac{L}{2}k_t} \right], \quad j, l = 1, \dots, N. \quad (1.32)$$

In the singular case, equation (1.31) has an easier representation, using Equation (1.30) and the alternate equation for the determinant in Eqn (1.31) below.

$$\det_N \chi = \begin{cases} \frac{1}{N+1}, & u_j = \frac{L}{2}k_j \\ \frac{-1}{N+1}, & u_j = \frac{L}{2}k_{j+1} \\ 0, & otherwise \end{cases} \quad (1.33)$$

The matrix elements of Equation (1.19) $\langle f_Q | P_\uparrow | f'_Q \rangle$ are given in Reference [79] as

$$\langle f_Q | P_\uparrow | f'_Q \rangle = Y_{f_Q} Y_{f'_Q} \frac{\partial}{\partial \lambda} \left(\det_N (\mathcal{Y} + \lambda \mathcal{Z}) \right) |_{\lambda=0} \quad (1.34)$$

where

$$\begin{aligned} \mathcal{Y}_j^l &= \int_0^L dy \overline{\Phi_j}(x) \Phi_l'(y) \\ &= K(k_l', k_j) - \frac{\theta_j}{\Theta} \sum_{t=1}^{N+1} K(k_l', k_t) \\ &\quad - \frac{\theta_l'}{\Theta'} \sum_{t=1}^{N+1} K(k_l', k_j) + \frac{\theta_j \theta_l'}{\Theta \Theta'} \sum_{t, t'=1}^{N+1} K(k_t', k_t) \end{aligned} \quad (1.35)$$

$$\begin{aligned} \mathcal{Z}_j^l &= \int_0^L dy \overline{\Phi_j}(x) \partial_y \Phi_l'(y) \\ &= k_l' K(k_l', k_j) - k_l' \frac{\theta_j}{\Theta} \sum_{t=1}^{N+1} K(k_l', k_t) \\ &\quad - \frac{\theta_l'}{\Theta'} \sum_{t=1}^{N+1} k_t' K(k_t', k_j) + \frac{\theta_j \theta_l'}{\Theta \Theta'} \sum_{t, t'=1}^{N+1} k_{t'}' K(k_{t'}', k_t) \end{aligned} \quad (1.36)$$

$$K(k', k) = \begin{cases} 1, & \text{if } k' = k \\ \frac{e^{i(k' - k)L} - 1}{i(k' - k)L} e^{i(\delta' - \delta)}, & \text{otherwise} \end{cases} \quad (1.37)$$

Note that since K is real

$$\begin{aligned} K(k', k) &= \frac{e^{i(k' - k)L} - 1}{i(k' - k)L} e^{i(\delta' - \delta)} \\ &= \frac{e^{2\pi i(n' - n)} e^{-2i(\delta' - \delta)} - 1}{i(k' - k)L} e^{i(\delta' - \delta)} = \frac{e^{-i(\delta' - \delta)} - e^{i(\delta' - \delta)}}{i(k' - k)L} \\ &= \frac{2i \sin(\delta' - \delta)}{i(k' - k)L} = \frac{2 \sin(\delta' - \delta)}{(k' - k)L} \end{aligned} \quad (1.38)$$

then so are \mathcal{Y} and \mathcal{Z} .

We look at this formula separately for when $|f'_Q\rangle = |f_Q\rangle$ and $|f'_Q\rangle \neq |f_Q\rangle$. First, for the diagonal matrix elements, we have

$$\langle f_Q | P_\uparrow | f_Q \rangle = q - \left(\sum_{t=1}^{N+1} \frac{\theta_t^2}{(1 + \theta_t^2)} k_t \right) \left(\sum_{t=1}^{N+1} \frac{\theta_t^2}{(1 + \theta_t^2)} \right)^{-1}. \quad (1.39)$$

which, when f_Q is singular, becomes

$$q \left(1 - \frac{1}{N+1} \right). \quad (1.40)$$

To find a computationally efficient manner to calculate the off-diagonal case, we take equation (1.34) and manipulate it in two different ways. First we separate it out into two different determinants

$$\det(\mathcal{Y} + \lambda \mathcal{Z}) = \det[\mathcal{Y}(\mathbb{1} + \mathcal{Y}^{-1} \lambda \mathcal{Z})] \quad (1.41)$$

$$= \det(\mathcal{Y}) \det(\mathbb{1} + \mathcal{Y}^{-1} \lambda \mathcal{Z}) \quad (1.42)$$

$$(1.43)$$

and second we use the identity (1.44) to transform the more complicated determinant into a trace

$$\ln(\det(X)) = \text{tr}(\ln(X)) \quad (1.44)$$

$$\begin{aligned}
\frac{\partial}{\partial \lambda} \det(\mathcal{Y} + \lambda \mathcal{Z}) &= \frac{\det(\mathcal{Y} + \lambda \mathcal{Z})}{\det(\mathcal{Y} + \lambda \mathcal{Z})} \frac{\partial}{\partial \lambda} \det(\mathcal{Y} + \lambda \mathcal{Z}) \\
&= \det(\mathcal{Y} + \lambda \mathcal{Z}) \frac{\partial}{\partial \lambda} \ln(\det(\mathcal{Y}) \det(\mathbb{1} + \mathcal{Y}^{-1} \lambda \mathcal{Z})) \quad (1.45)
\end{aligned}$$

$$\begin{aligned}
\frac{\partial}{\partial \lambda} \ln(\det(\mathcal{Y}) \det(\mathbb{1} + \mathcal{Y}^{-1} \lambda \mathcal{Z})) \\
&= \frac{\partial}{\partial \lambda} \ln(\det(\mathcal{Y}))|_{\lambda=0} + \frac{\partial}{\partial \lambda} \ln(\det(\mathbb{1} + \mathcal{Y}^{-1} \lambda \mathcal{Z}))|_{\lambda=0} \\
&= 0 + \frac{\partial}{\partial \lambda} \text{tr}(\ln(\mathbb{1} + \mathcal{Y}^{-1} \lambda \mathcal{Z}))|_{\lambda=0} \\
&= \text{tr} \frac{\partial}{\partial \lambda} (\ln(\mathbb{1} + \mathcal{Y}^{-1} \lambda \mathcal{Z}))|_{\lambda=0} \quad (1.46)
\end{aligned}$$

Next the logarithmic expansion is taken from the last form of equation (1.46), and we again use the position the derivative is taken at to simplify the form

$$\begin{aligned}
\ln(\mathbb{1} + \mathcal{Y}^{-1} \lambda \mathcal{Z}) &= \lambda \mathcal{Y}^{-1} \mathcal{Z} + \frac{(\lambda \mathcal{Y}^{-1} \mathcal{Z})^2}{2} + \dots \\
&\implies \frac{\partial}{\partial \lambda} (\ln(\mathbb{1} + \mathcal{Y}^{-1} \lambda \mathcal{Z}))|_{\lambda=0} = \mathcal{Y}^{-1} \mathcal{Z} \\
&\implies \frac{\partial}{\partial \lambda} \ln(\det(\mathcal{Y} + \lambda \mathcal{Z}))|_{\lambda=0} = \text{tr}(\mathcal{Y}^{-1} \mathcal{Z}) \\
&\implies \frac{\partial}{\partial \lambda} \det(\mathcal{Y} + \lambda \mathcal{Z})|_{\lambda=0} = \text{tr}(\mathcal{Y}^{-1} \mathcal{Z}) \det(\mathcal{Y} + \lambda \mathcal{Z}) \quad (1.47)
\end{aligned}$$

where we have taken advantage of the fact that the derivative is taken at $\lambda = 0$.

In order to solve the above equation we split the definition of \mathcal{Y}^{-1} via singular value decomposition (SVD)

$$\text{tr}(\mathcal{Y}^{-1} \mathcal{Z}) = \text{tr}((\mathcal{U} \Sigma_Y \mathcal{V}^*)^{-1} \mathcal{Z}) = \text{tr}(\mathcal{V}^{*-1} \Sigma_Y^{-1} \mathcal{U}^{-1} \mathcal{Z}) \quad (1.48)$$

which, using the fact that \mathcal{Y} is real, and hence \mathcal{V} and \mathcal{U} are both unitary and real, can be represented as

$$\text{tr}(\Sigma_Y^{-1} (\mathcal{U}^T \mathcal{Z} \mathcal{V})). \quad (1.49)$$

Using the fact Σ is diagonal, and that $\det(\Sigma_Y) = \det(\mathcal{Y})$, we can write

$$\begin{aligned}
\text{tr}(\Sigma_Y^{-1}(\mathcal{U}^T \mathcal{Z} \mathcal{V})) \det(\Sigma_Y) &= \text{diag}(\Sigma_Y^{-1}) \cdot \text{diag}(\mathcal{U}^T \mathcal{Z} \mathcal{V}) \cdot \det(\Sigma_Y) \\
&= \left[\frac{1}{\Sigma_2}, \frac{1}{\Sigma_3}, \dots, \frac{1}{\Sigma_{N+1}} \right] \text{diag}(\mathcal{U}^T \mathcal{Z} \mathcal{V}) \prod_{n=2}^{N+1} \Sigma_n \\
&= \left[\frac{\prod_{n=2}^{N+1} \Sigma_n}{\Sigma_2}, \frac{\prod_{n=2}^{N+1} \Sigma_n}{\Sigma_3}, \dots, \frac{\prod_{n=2}^{N+1} \Sigma_n}{\Sigma_{N+1}} \right] \text{diag}(\mathcal{U}^T \mathcal{Z} \mathcal{V}) \\
&= \left[\prod_{n \neq 2}^{N+1} \Sigma_n, \prod_{n \neq 3}^{N+1} \Sigma_n, \dots, \prod_{n=2}^N \Sigma_n \right] \text{diag}(\mathcal{U}^T \mathcal{Z} \mathcal{V}). \quad (1.50)
\end{aligned}$$

Finally, using the fact that the definition of \mathcal{Y} is the same as the matrix used in the dot product of eigenstates (1.23) we know that $\det(\mathcal{Y}) = 0$ for off-diagonal states. This means that one value of Σ_n must be zero. Without loss of generality we can set this to be the element N , so we have the computationally efficient representation

$$\langle f_Q | P_{\uparrow} | f'_Q \rangle = Y_{f_Q} Y_{f'_Q} \frac{\partial}{\partial \lambda} \left(\det_N (\mathcal{Y} + \lambda \mathcal{Z}) \right) |_{\lambda=0} = Y_{f_Q} Y_{f'_Q} \prod_{n=2}^N \Sigma_n \cdot (\mathcal{U}^T \mathcal{Z} \mathcal{V})_{NN} \quad (1.51)$$

where $(\mathcal{U}^T \mathcal{Z} \mathcal{V})_{NN}$ is the final element of the $N \times N$ matrix $\mathcal{U}^T \mathcal{Z} \mathcal{V}$. This equation is only valid for off-diagonal elements, so the diagonal elements must be calculated with Equation (1.39). For the special case of $c = -\infty$ calculating the matrix elements requires accounting for the singularities in the \mathcal{Y} and \mathcal{Z} matrices. This is done by using equation (1.29) for the singular roots in equations (1.36) and (1.35).

The equations (1.39,1.25,1.31), and their special case equivalents for singular Bethe roots (1.40,1.33,1.30) were already encoded into reference [90]. This work required implementing equation (1.51) in a distributed manner, which allowed calculating the full momentum against time evolution of the impurity via Equation (1.19).

As there are an infinite number of eigenstates on the RHS of Eqn (1.19), some subset must be taken for a numerical calculation of the momentum. Given that this will inevitably introduce some error in the momentum calculated, we need

some way to ensure the subset of states we are using reproduces the actual value of Eqn (1.19) close enough for quantitative results. A quantitative bound on the error in momentum has been derived in reference [79], which depends on a bound in the absolute value of the matrix element $\bar{P} = \sup(|\langle f_Q | P_\downarrow | f'_Q \rangle|)$, and the saturation of

$$\varsigma = \sum_{i=1}^N |\langle FS | f_{Q,i} \rangle|^2. \quad (1.52)$$

This value ς must approach 1 as $N \rightarrow \infty$ due to the completeness of the Bethe eigenstates [79]. It is noteworthy that this bound on the error,

$$\sqrt{\bar{P}^2(2\varsigma(1-\varsigma) + 2(1-\varsigma)^2)} \quad (1.53)$$

is independent of time, which allows us to plot the impurity's momentum for large time with the same accuracy as any other point. We will use this attribute heavily when inspecting the momentum revivals of the system in Section 2.4, which can happen on a time scale of $t \approx 140t_F$.

Throughout the text we talk of the saturation of the sum rule ς instead of the bound on the error in the momentum. This is done to keep the relation between the number of states counted, and the value of $|\langle FS | f_Q \rangle|^2$ for those states clear. We wish to maintain the connection between these values, as while the time dependent momentum evolution has been studied before [69, 70], the isolation of eigenstate pairs responsible for each feature of the momentum in Chapter 3 is wholly novel work and can be better understood in these terms.

1.2.2 Method

Despite these pre-existing solutions and methods, the evaluation of Eqn (1.19), is still difficult, as when the system is highly excited, a reliable calculation has to account for the contribution of a large number of eigenstates [79].

In order to calculate states and choose which states to use, we use a program written in the Python programming language [92] with the Scipy and Numpy [93,

94] external libraries. The program uses a stochastic sampling algorithm to find and choose a smaller subset than in [69], that will still reliably reproduce observables, the discovered states are then accumulated with the greatest $|\langle FS|f_Q\rangle|$ first. This program has been used in work before [95], is freely available online [90], and provides not only the overlap value for every state used, but the diagonal matrix elements of the momentum operator. To this program, we add the functionality to calculate the off-diagonal matrix elements of the momentum operator $\langle f_Q|P_\uparrow|f'_Q\rangle$ for $f_Q \neq f'_Q$ (see Equation (1.51), and hence the impurity's time-dependent momentum evolution. This additional code is also freely available, an overview of its structure is given in Appendix A, and the source code can be found at [91].

Chapter 2

Observables of the System

2.1 Introduction

This chapter details the difference in $\langle P_{\downarrow}(t) \rangle$ with differing parameters of the system. The three physical parameters we can change within the restrictions of our model are the system size, the initial momentum of the impurity, and the dimensionless interaction strength parameter γ . Note the only dependency of $\langle P_{\downarrow}(t) \rangle$ on the density of the background gas $n = N/L$ or the interaction strength g is via the dependency on γ and not on the values themselves. While the momentum against time of the impurity has been discussed in other work [69, 70, 79], we look further into the revivals of the impurity's momentum that come from finite size effects in Section 2.4. We then present comparisons between $\langle P_{\downarrow}(\infty) \rangle$ as calculated from Eqn (1.20) and the momentum plateau obtained when plotting the full evolution of $\langle P_{\downarrow}(t) \rangle$ in Section 2.5. We also discuss the variation of $\langle P_{\downarrow}(t) \rangle$ with ς (see Section 1.2.2), which will provide grounding for the discussion on separating contributions provided in Chapter 3. Where this chapter overlaps with [69, 70], there is consistent agreement, corroborating their results and increasing the confidence that both our programs give the correct numerical value for the solution of this model.

2.2 Justification

As mentioned in Section 1.2.1, when calculating $\langle P_{\downarrow}(t) \rangle$, a large number of states must be accounted for in the sum of Eqn (1.19).

Reaching a high saturation of ς is easier said than done, as while $1 - \varsigma$ decreases linearly with the log of the number of states (see Fig 2.1), this relation only happens until $\varsigma \approx 0.96$, and the number of states required for a given ς strongly increases with system size, as seen in Fig 2.2.

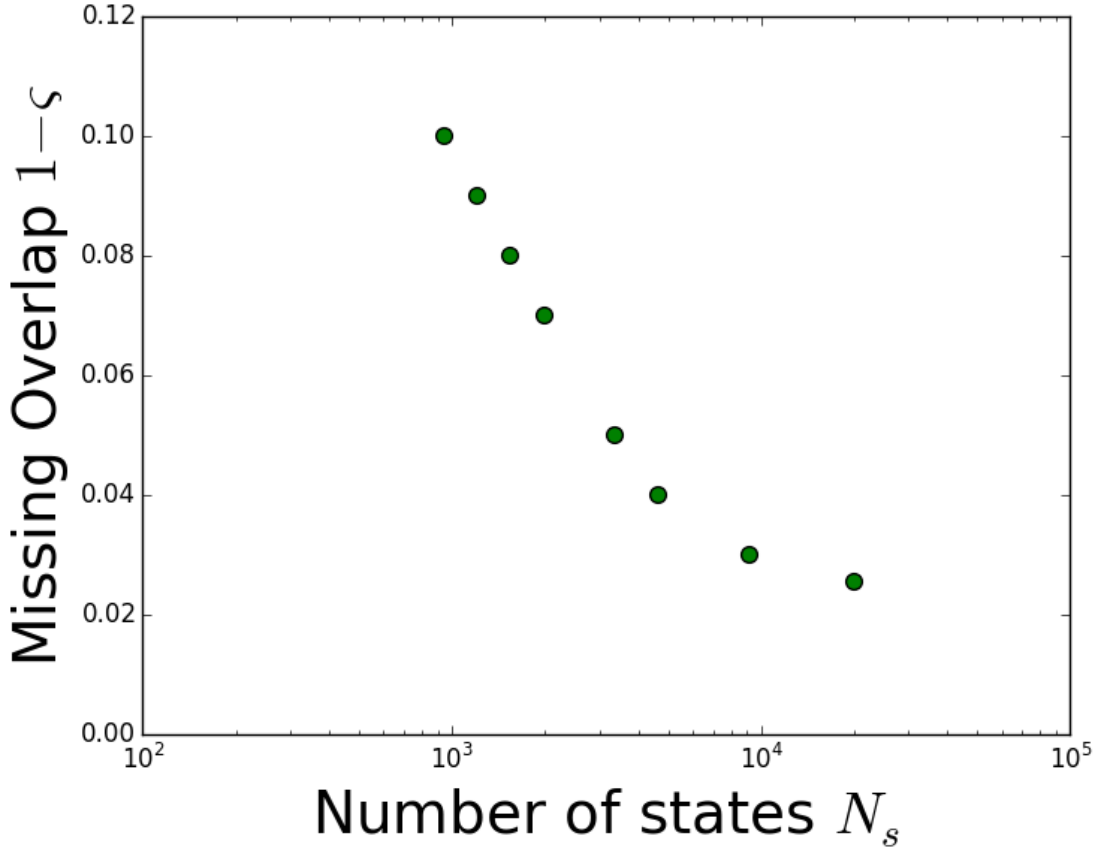


Figure 2.1: The number of states required for a range of saturation values for ς . We show the semi-log plot of how ς changes with the number of states. The progression is linear until a $\varsigma \approx 0.96$, at which point many more states are required to provide further accuracy.

Because of the computational restrictions on the number of states used and the system size (see Appendix A), calculating the impurity's momentum against time is prohibitively expensive for a number of states $N_s > 20000$ and a system size of $N = 99$, which gives an overlap of $\varsigma \approx 0.97$ which is not a large enough ς

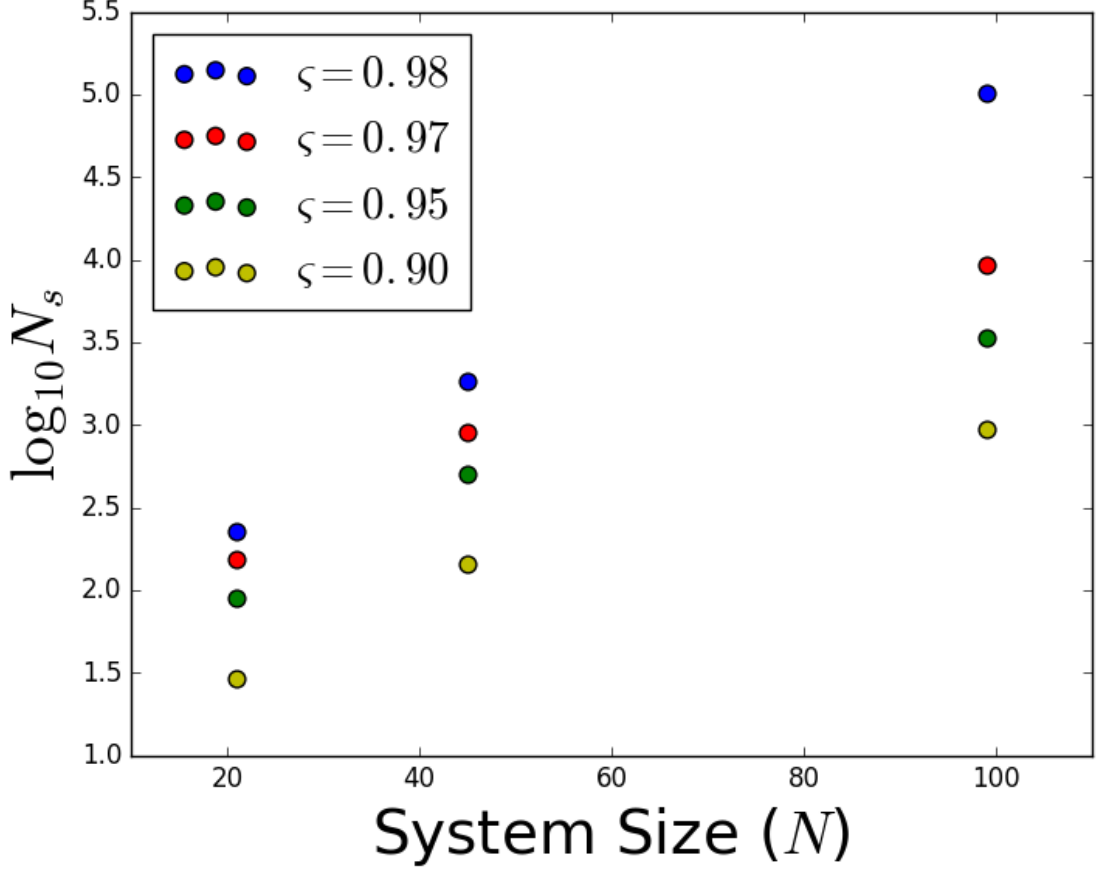
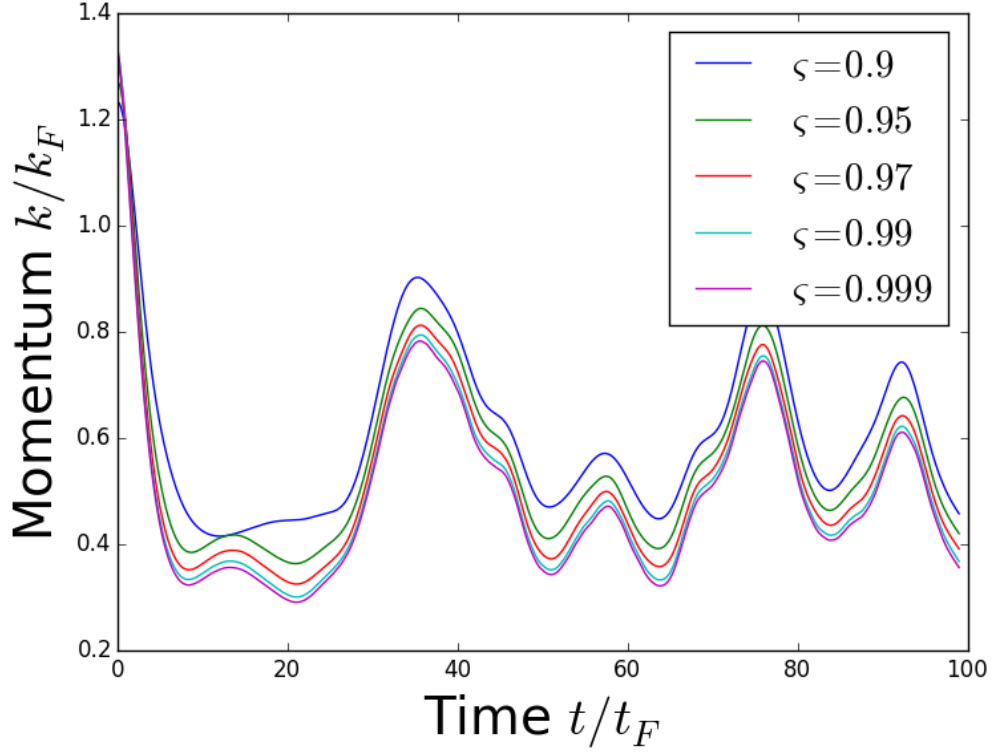


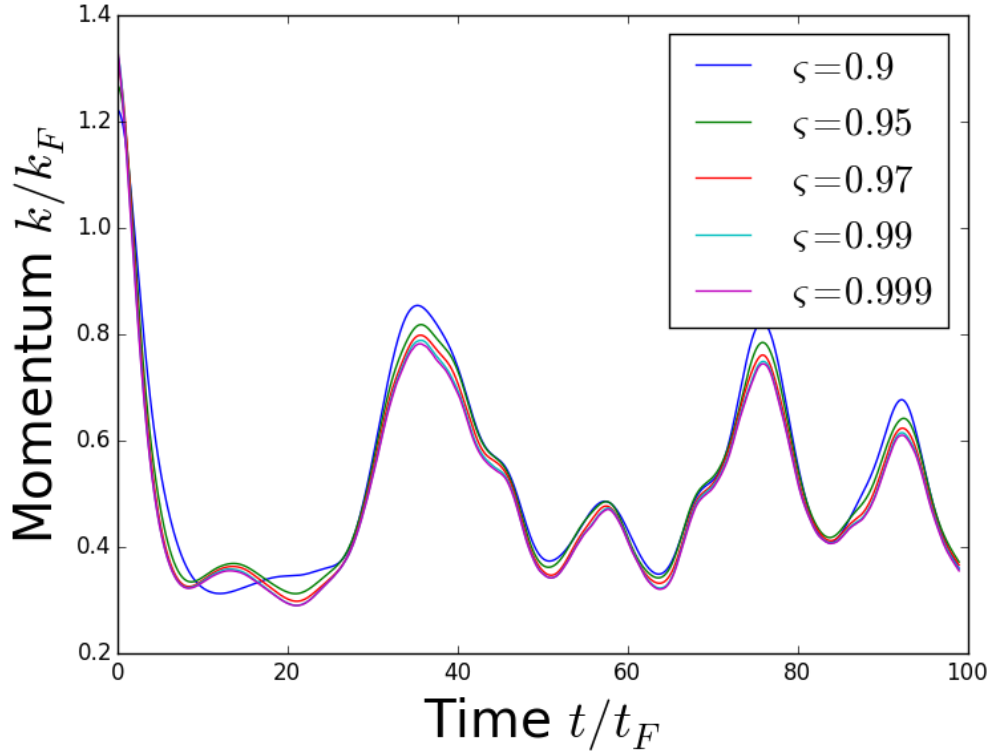
Figure 2.2: The number of states required for a range of saturation values for ζ . We show the semi-log plot of how the number of states required for a given ζ changes with increasing system size, the progression is not linear, so this is not an exponential relation, but the plot does show a large increase in the number of states required as larger systems are used.

for confidence in our results from the saturation itself. This is a problem, as for those systems where we can reach $\zeta = 0.99$ some of the more interesting features of the system are hidden by finite size effects (see Sections 2.4 2.5)

Fortunately, we find evidence in these smaller systems that a missing sum rule contribution this small does not change the general shape of the momentum evolution, but rather introduces some minor variances, and a total downwards shift in the momentum of the impurity as seen in Fig 2.3a. While the normalisation in this manner has no rigorous mathematical backing, it is a useful approximation for values of the plateau in a wider range of parameters than otherwise available. Fig 2.8 provides more details on how a change in ζ affects $\langle P_{\downarrow}(t) \rangle$.



(a)



(b)

Figure 2.3: a) As ζ is increased past 0.9 to 0.999, the main observable change in $\langle P_{\downarrow}(t) \rangle$ is a downwards shift over the entire time range. b) This downwards shift can be normalised out by the value of ζ to provide approximate results when the number of states required for a satisfactory ζ value is too high.

As our main focus in this chapter is on the momentum revivals, which are the feature least investigated in reference [69], the fact that these are stable once ς has passed $\varsigma \approx 0.9$ puts good confidence behind our results. As shown in Fig 2.3b, normalising $\langle P_{\downarrow}(t) \rangle$ by the sum rule saturation we have reached goes some way to accounting for the difference in the plateau of $\langle P_{\downarrow}(t) \rangle$. This normalisation is done with the equation

$$\widetilde{\langle P_{\downarrow}(t) \rangle} = Q - \frac{\sum_{f_Q, f'_Q} e^{it(E_f - E_{f'})} \langle FS | f_Q \rangle \langle f_Q | P_{\downarrow} | f'_Q \rangle \langle f'_Q | FS \rangle}{\sum_{f_Q} |\langle FS | f_Q \rangle|^2} \quad (2.1)$$

which would provide the total and correct $\langle P_{\downarrow}(t) \rangle$ if the set of states accounted for provided a fully representative evolution. This extends the range of system sizes we can investigate to 99 particles, beyond what has been seen previously [69, 70]. The additional range lets us view the evolution of the system for a much longer time without the intrusion of finite size effects (discussed in detail in later chapters). However, the normalisation is not sufficiently effective to allow the approach to be used for investigating systems that contain more than about 99 particles. The dependence of the properties of the momentum on ς is further explored in Sections 2.5 and 2.6.

2.3 Overall Momentum

With the previous justification, we can access a wide range of system parameters, and view how the impurity's momentum evolution changes within this extended parameter space. We reiterate that within our model we have three physical parameters: the system size N , the initial momentum of the impurity Q , and the dimensionless interaction strength γ . The difference in the impurity's momentum evolution when changing each of these parameters can be seen in Figures 2.4, 2.5 and 2.6 respectively. While there are many changes throughout the parameter space, there are consistently three main features of the momentum evolution: the regular revivals, a period of non-zero relatively constant momentum, and the small

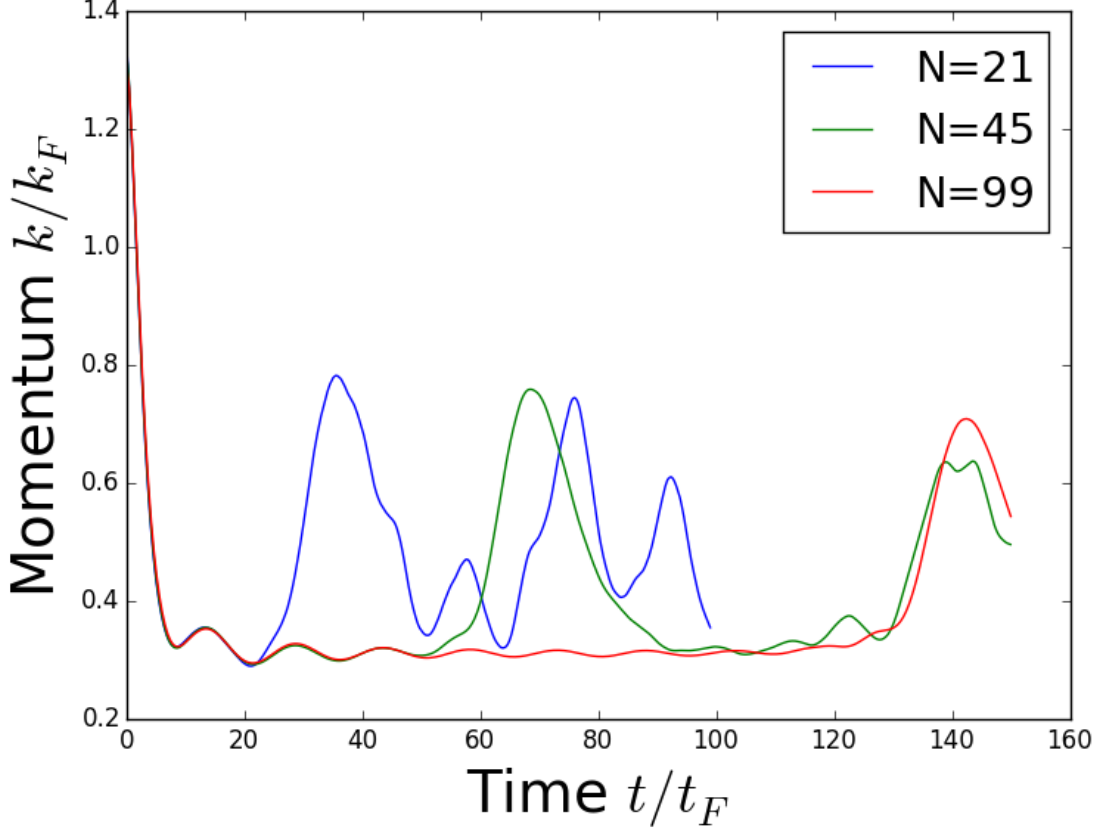


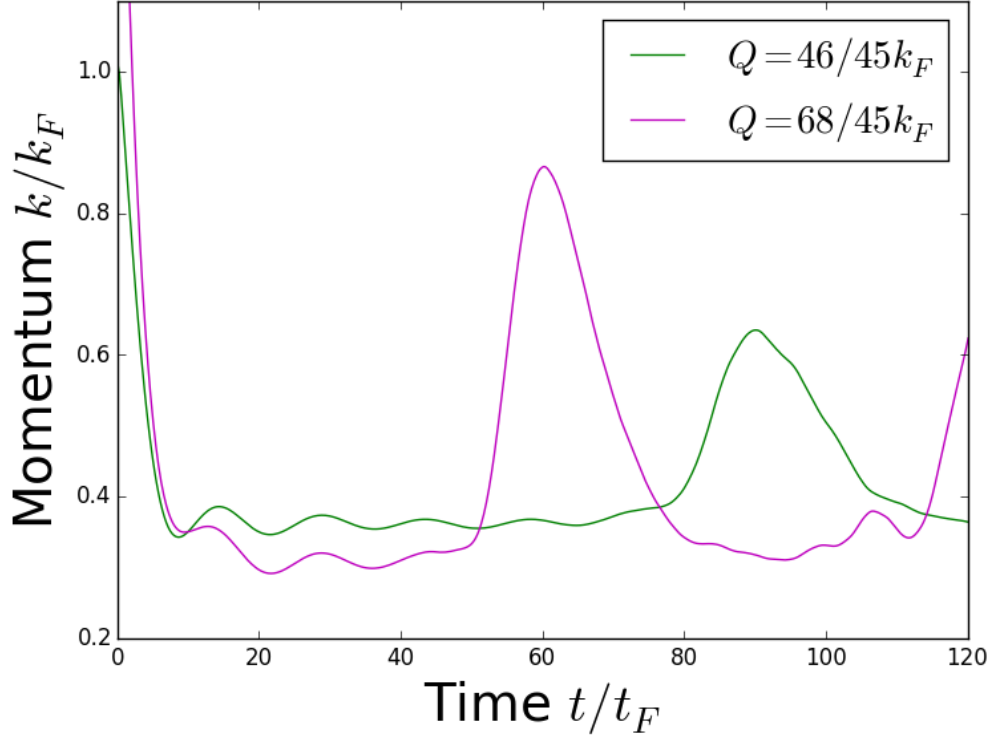
Figure 2.4: Impurity momentum evolution for multiple system sizes. Plots showing $\langle P_{\downarrow}(t) \rangle$ over systems of 21, 45, and 99 particles with constant $\gamma = 3$ and constant initial momentum of $Q = \frac{4}{3}k_F$. Until the revival in the impurity’s momentum, the evolution of the impurity is identical for all system sizes, the revivals increase in period with a linear progression on the system size (see Fig 2.9), and they are the only finite size effect apparent here. The consistency of the flutter and plateau is in agreement with [69]. In this plot we ensure ς is consistent for $N = 21$ and $N = 45$, however we were unable to match the ς for $N = 99$, so we plot all data once appropriately normalised. When not normalised by the value of ς , the only noticeable difference is a total shift downwards in the entire plot for $N = 99$.

scale oscillations in this region (dubbed “quantum flutter” in previous work [69]). These features were described in reference [69], and the same work thoroughly discussed both the phenomenology of the plateau and quantum flutter, and gave an argument for the physical cause of the features. Though previous work has thoroughly investigated two of these features, we will discuss each of them in turn over the following sections to provide a full description of the system as a setting for future chapters. The next section will discuss the momentum revivals, being the least investigated feature of the system, the plateau and flutter are discussed

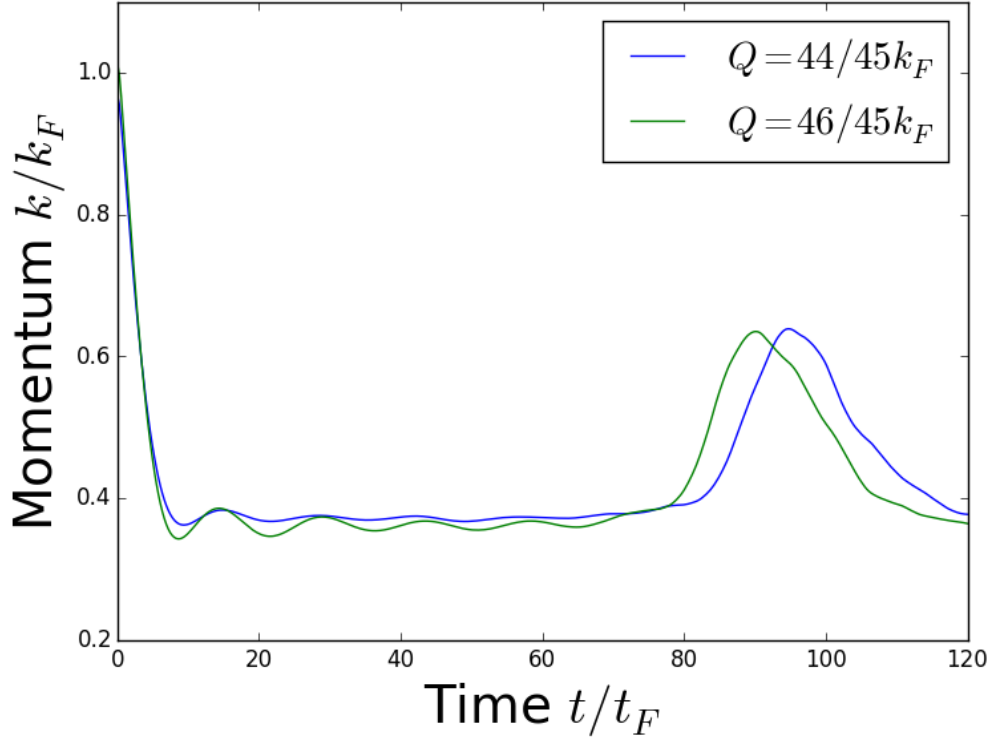
after in Sections 2.5, and 2.6.

Within these sections, we also show the change in $\langle P_{\downarrow}(t) \rangle$ over the non-physical parameter ς (of which the general shape is shown in Figures 2.7 and 2.8) where relevant. While the change in the momentum evolution with ς is not a physical property of the system, but a property of the solution we are using for this model, it is still important to know how $\langle P_{\downarrow}(t) \rangle$ changes with ς , both in order to gain insight into how the solution behaves, and because it is not always possible to reach large enough ς for a strong limit on the maximum error. Knowing how $\langle P_{\downarrow}(t) \rangle$ changes with ς means we can investigate larger systems with an understanding of what errors we are letting into our results.

As can be seen in Figures 2.7, and 2.8, the revival period is independent of the last 0.1 in the ς , though both the flutter and plateau undergo changes. While some of the change in the plateau can be normalised out by using $\widetilde{\langle P_{\downarrow}(t) \rangle}$ in place of $\langle P_{\downarrow}(t) \rangle$ as described in Section 2.2, we have no way to convert the flutter of an under-saturated ς to what would occur with perfect saturation.



(a)



(b)

Figure 2.5: $\langle P_{\downarrow}(t) \rangle$ over multiple values of Q , with a fixed system size $N = 45$ and interaction strength $\gamma = 3$. a) While $Q > k_F$, increasing Q decreases both the plateau and time to the momentum revival (see Sections 2.4 and 2.5). b) As Q decreases past k_F , the flutter goes away, which is a central feature of reference [69].

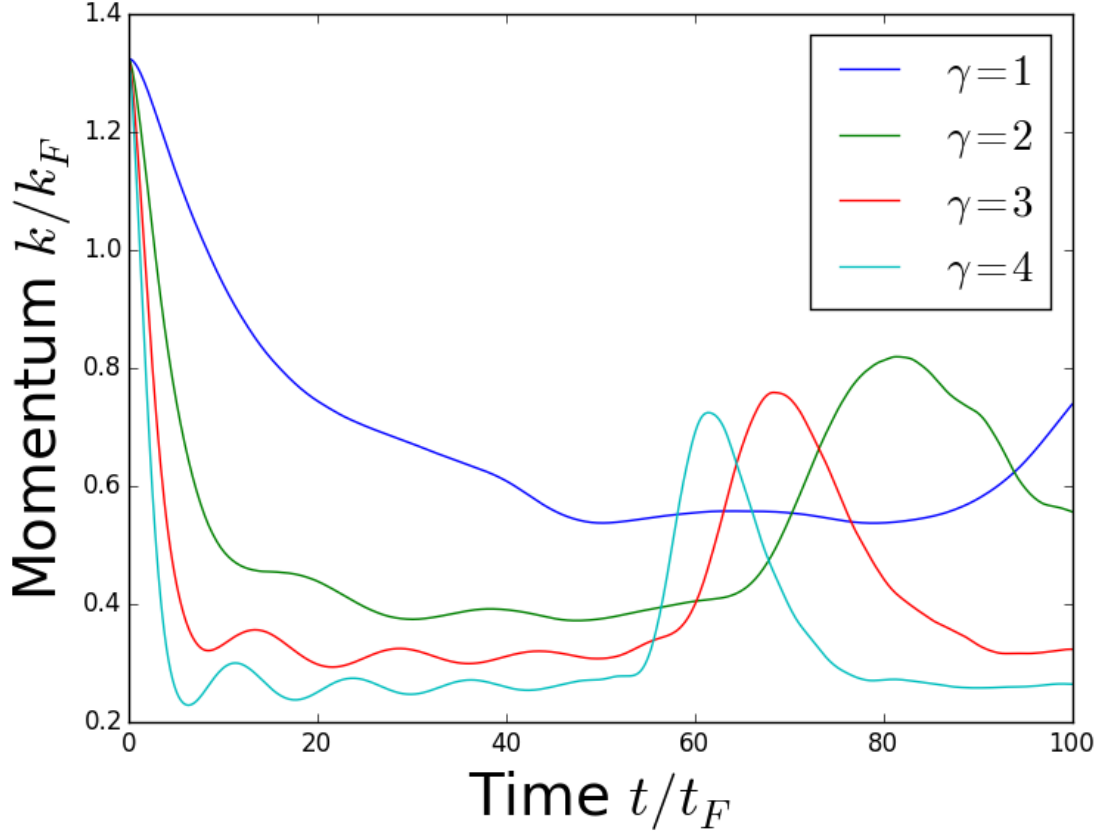


Figure 2.6: Change in $\langle P_{\downarrow}(t) \rangle$ with γ for fixed system size $N = 45$ and $Q = \frac{4}{3}k_F$. As γ increases, the revival period decreases, the plateau in the momentum decreases, and the flutter frequency increases. The change in the revival periods and the plateau can be qualitatively interpreted as an increase in the momentum transfer to the background gas, while the flutter follows the progression described in Equation (2.3), formed from the argument presented in [69, 70].

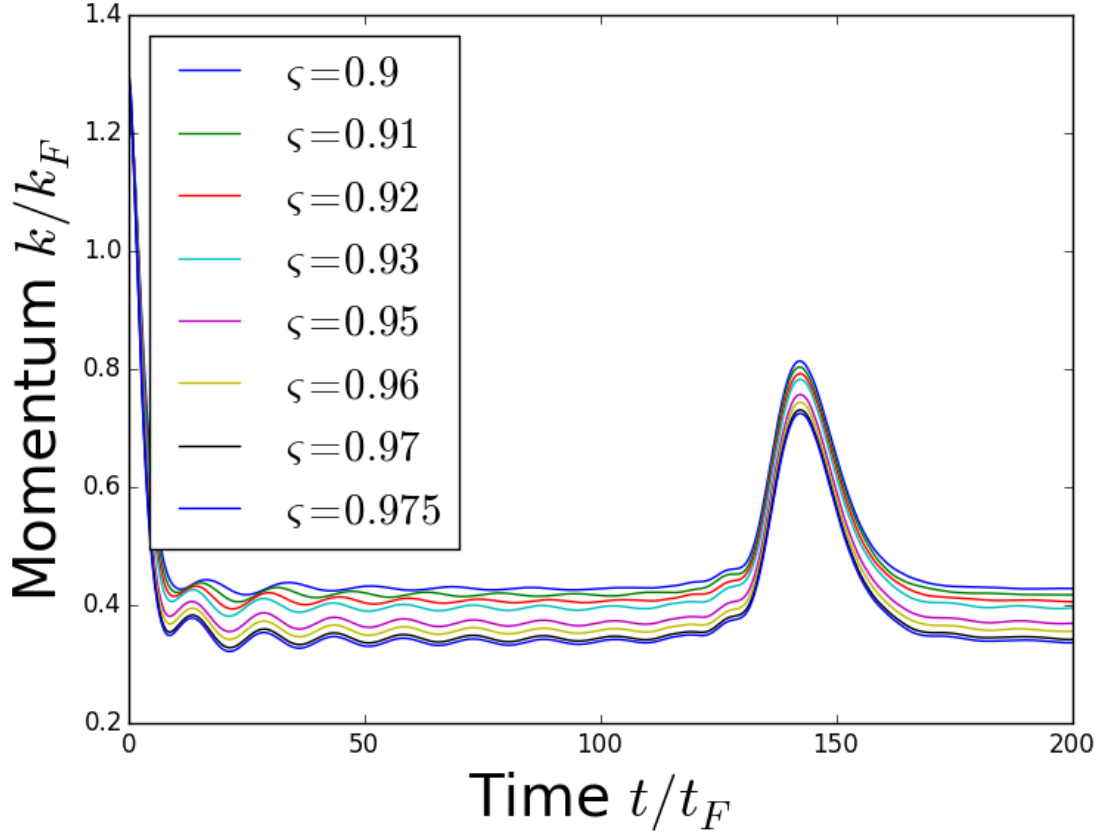


Figure 2.7: The change in $\langle P_{\downarrow}(t) \rangle$ over ζ with fixed $N = 99$, $\gamma = 3$ and $Q = \frac{4}{3}k_F$. Here a larger system size than previous is used, as the features which differ with changing overlap are sometimes obscured by finite size effects. As ζ increases, the revival period is constant, the flutter frequency increases, and the plateau decreases. The flutter frequency increases with increasing overlap, but reaches a constant value at a ζ of about 0.95, while the plateau tends to some value, but has not saturated in the ζ range shown.

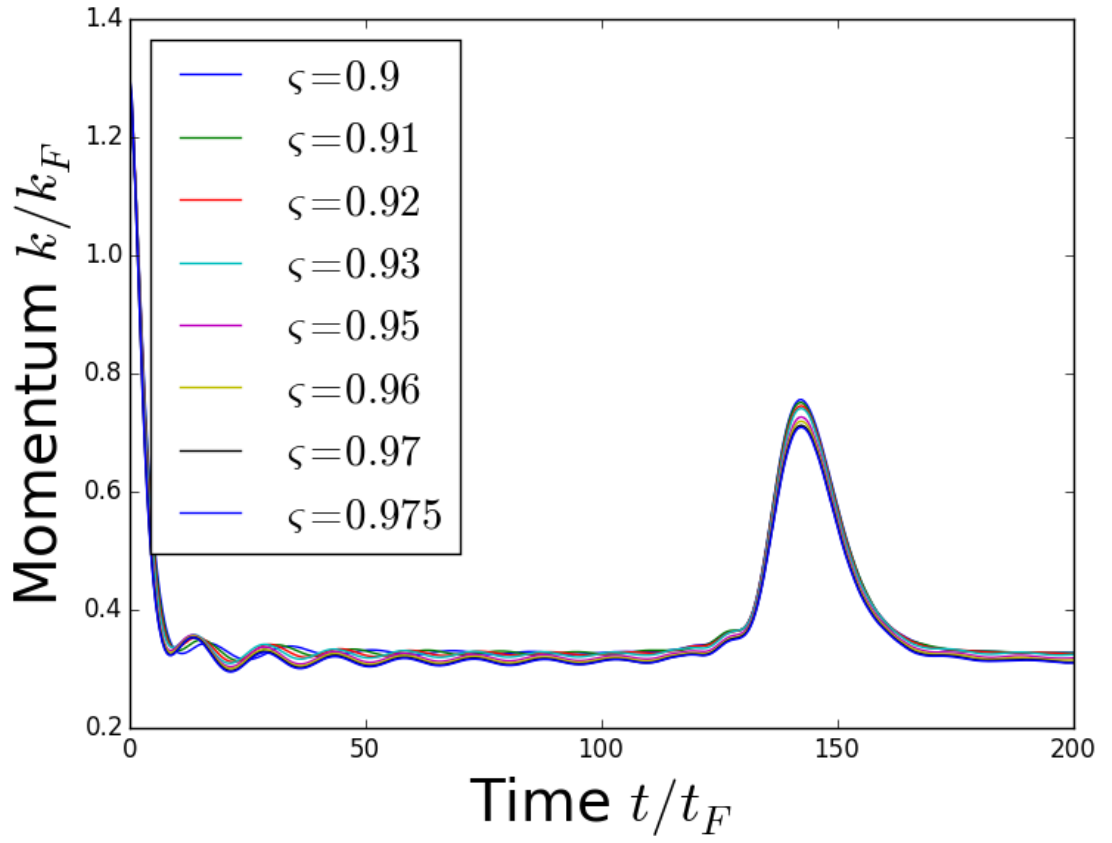


Figure 2.8: The change in $\langle \widetilde{P_{\downarrow}}(t) \rangle$ with ς with fixed $N = 99$, $\gamma = 3$ and $Q = \frac{4}{3}k_F$. Of the two features that change with ς , the plateau change can be almost factored out with normalisation.

2.4 Momentum Revivals

Of the three main features in $\langle P_{\downarrow}(t) \rangle$, the momentum plateau and the flutter are features present in the thermodynamic limit of $N \rightarrow \infty$ with constant N/L , while the revivals in the momentum are finite size effects which can only be seen in systems small enough for the given parameters and time range.

While these revivals would not be present in a macroscopic scale gas, they're relevant in experiment, which often use gases of the same order of magnitude N as we can numerically probe [12, 13, 20, 24]. The momentum revivals can be problematic, as they can mask the evolution of the other momentum features for smaller system sizes, but they are an interesting feature themselves which have not yet been thoroughly investigated.

From a semi-classical argument, we can attribute the cause of the momentum revivals to the finite size of the system, with the momentum packet put into the background gas by the impurity moving through the gas until it reaches and excites the impurity again. Were there hard boundaries in the system, the time this effect should appear would be influenced by the initial position of the impurity; however in our model, the periodic boundary conditions give us translational invariance, which means the time period of the momentum revivals is only determined by the physical parameters of the system that we have previously discussed. If we take the revival period as

$$t_{rev} \approx \frac{L}{2p_{relative}} \quad (2.2)$$

where t_{rev} is the revival period, L is the length of the system, and $p_{relative} = Q - 2p$ (for p representing the value of the plateau seen) is the momentum in the packet put into the background gas relative to that of the impurity's plateau, we can see this predicts a linear change in revival period with increasing system size, which matches what we see in Figure 2.4. A similar increase in revival period and qualitative argument for the increase with system size was presented in [79], but was not fully explored.

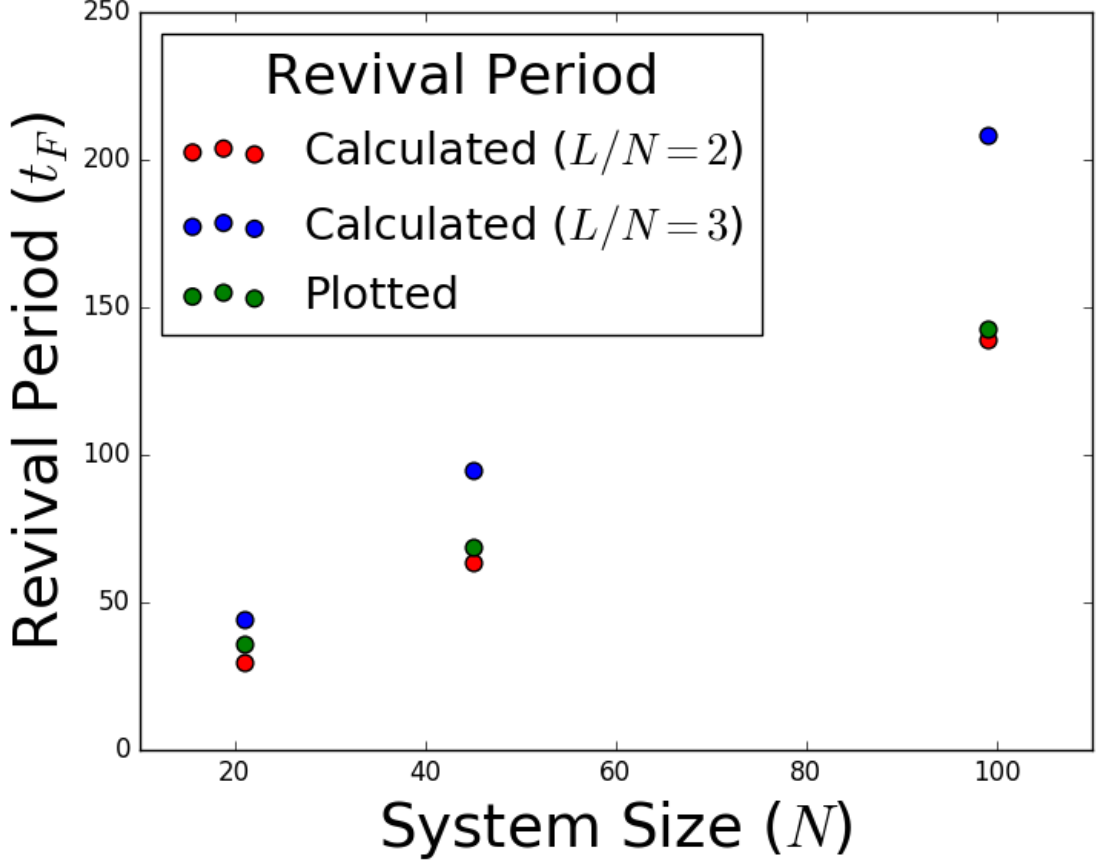


Figure 2.9: The progression of the revival period t_{rev} with changing system size N increases linearly, which is in good agreement with Eqn (2.2), and shows how the revivals are a finite size effect, diverging as $N \rightarrow \infty$. This plot was created with $Q = 4k_F/3, \gamma = 3$, but the particulars of how γ is set to its value are important for the prediction of Equation (2.2). We find empirically, that fixing $L/N = 2, g = 3$ gives the best predictions for Eqn (2.2), but for $L/N = 3, g = 2$ (as an example) the estimations are further off.

When this equation is applied to describe the change in the revivals over initial momentum Q and the interaction strength γ it qualitatively matches what we see, the change in momentum passed to the background gas contains most of the non-linearity of these changes. Though it qualitatively reproduces changes for most parameters this prediction is far from perfect, completely neglecting the fact that γ can change with both g and L , and failing to even qualitatively predict the progression for a low initial momentum $Q > k_F$ (see Figure 2.10). In Figures 2.10, 2.9, and 2.11 we show how the choice of L/N and g for a fixed γ affects the prediction of Eqn (2.2). The progression with Q indicates Eqn (2.2) should have some dependence on the initial momentum, possibly defining the ratio of g to L

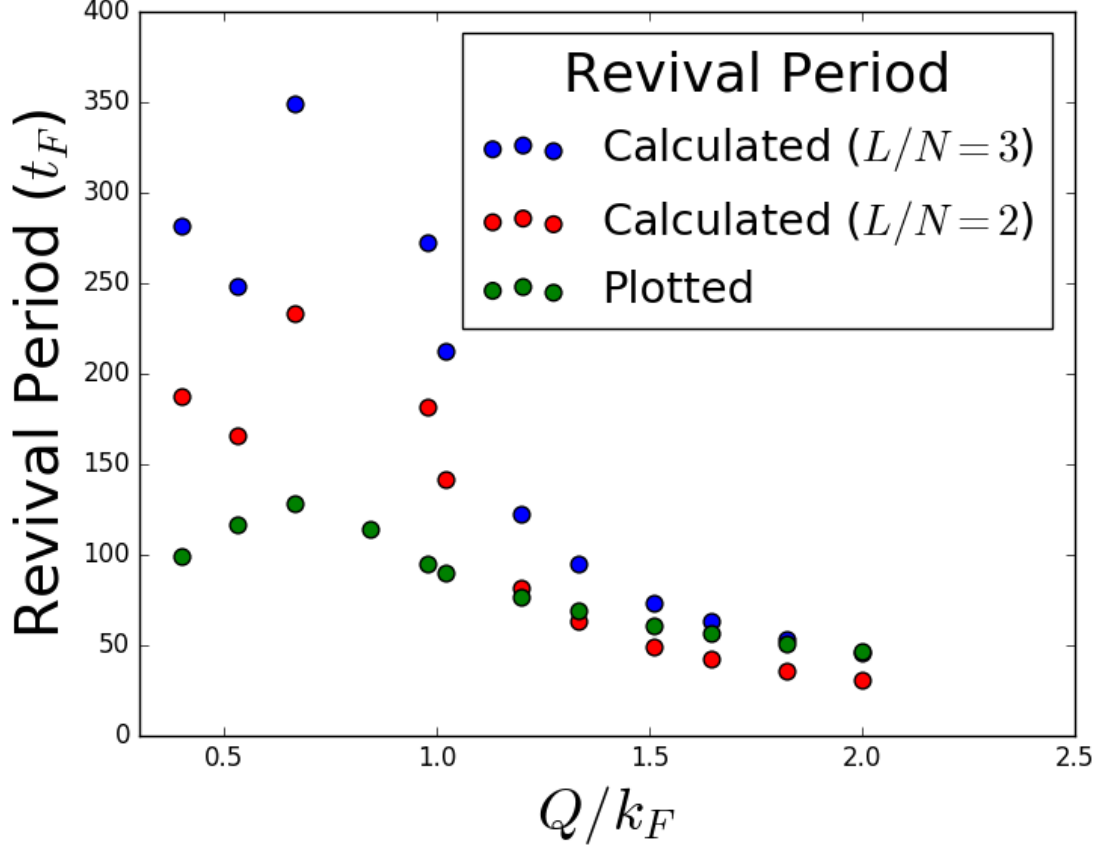


Figure 2.10: The change with Q of the revival period t_{rev} progresses in a non-trivial manner, mostly following the progression of the momentum plateau (to be shown in Section 2.5, see Figure 2.16). For a low initial momentum $Q < k_F$, the approximation in Eqn (2.2) is very poor, failing to even qualitatively reproduce the progression, but as the initial momentum becomes greater than the Fermi momentum it gives a better prediction. Note the estimated revival periods for $Q = \frac{38}{45}k_F$ are not shown as they are greater than $1000t_F$, once again demonstrating this estimate is not useful for a low initial momentum. As with Figures 2.9 and 2.11, the choice of how to set γ is important for this prediction. The current plot was created with $L/N = 2$ for the red points, and $L/N = 3$ for the blue ones. While in Figures 2.9 and 2.11, the choice of $L/N = 2$ has been shown to be the most accurate for $Q = \frac{4}{3}k_F$, this plot demonstrates a dependence of the optimum choice on the initial momentum Q , though the exact relation is currently unknown.

with which γ is formed.

The fact this prediction is dependent on the ratio of g to L , while the actual momentum is only dependent on their product shows the limitations of the simple interpretation that leads to Eqn (2.2). Nevertheless the equation remains useful for systems with high initial momentum to show the qualitative progression when this particular fault is sidestepped.

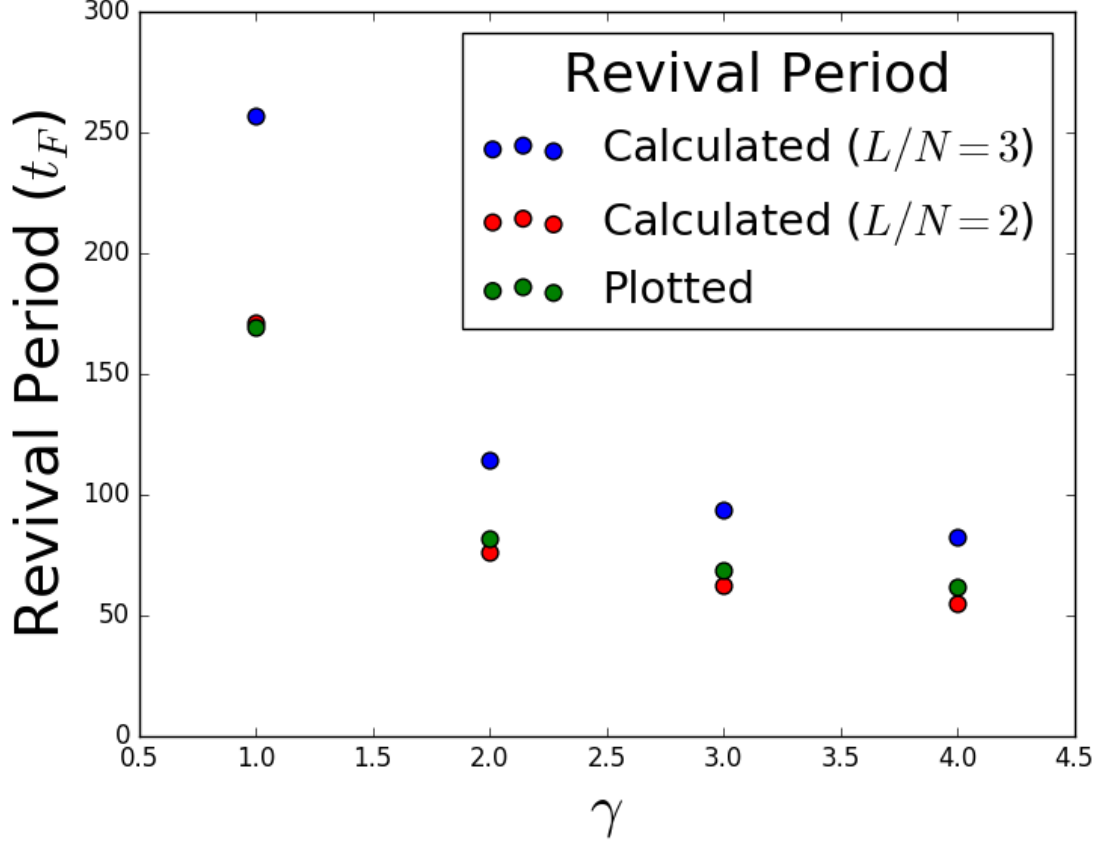


Figure 2.11: The change in revival period t_{rev} with respect to γ , shows that Eqn (2.2) qualitatively reproduces the progression of the momentum revivals. It should be noted that the revival period plotted for $\gamma = 1$ is highly suspect as the revival is not nearly as clear as other points, having a relative peak spanning $100t_F$, we chose the highest point of this peak, which was near its end. Like in Fig 2.9 and 2.10 the way γ is set has a strong influence on the accuracy of Eqn (2.2), with two example data sets shown, we fix L/N , at 2 for the red points, and 3 for the blue ones.

Figure 2.12a shows a longer term evolution of the momentum, demonstrating an initial decoherence of the revivals with increasing time. Despite this apparent progression in the short term, a plot of $\langle P_{\downarrow}(t) \rangle$ for $t \gg t_{rev}$ shows no point where they have been fully dispelled (see Fig 2.12), with some ranges of t still showing quite strong revivals. From this information, we can see that for a finite system, the impurity never reaches a fully thermalised state, only ever reaching the plateau before finite size effects set in.

As the period of the revivals is constant after a very low value of ς as seen in figure 2.8, we can infer the major contribution to this feature comes from states with among the greatest $|\langle FS|f_Q \rangle|$, as will be demonstrated alongside a thorough

exploration into attributing eigenstate pairs to each feature in $\langle P_{\downarrow}(t) \rangle$ in Chapter 3.

2.5 Infinite Time

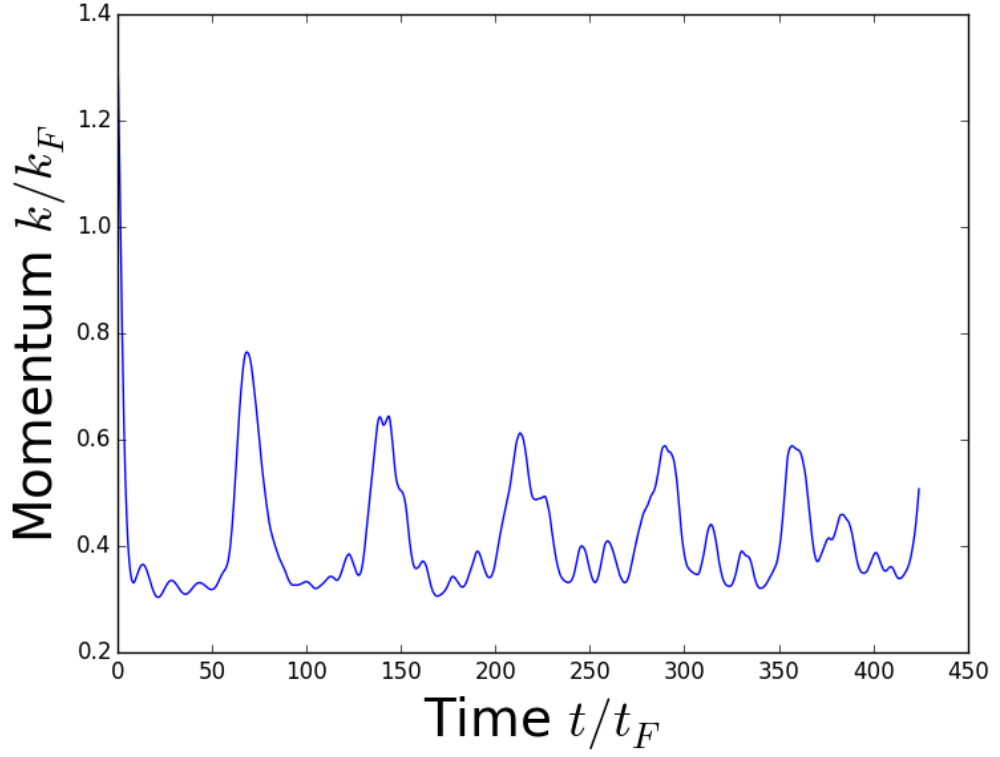
The fact the impurity's saturation momentum is non-zero is an interesting phenomenon. While a non-zero infinite time momentum inevitably draws comparisons to a superfluid, it must be stressed that typical superfluidity, like the Bose Einstein condensate, does not in general survive the transition to one dimension [96–98], and what aspects do cross over are strongly dependent on the particulars of the system [59, 99–101]. A non-zero saturation momentum has previously been predicted via ballistic transport, through an argument based on the dynamical conductivity in a system very similar system to this [102, 103], but the current feature is different. The discovery of non-zero infinite time momentum in the current system [69] has been of immediate interest, receiving further investigation and generalisation in references [70, 95, 104–106]. This section provides results corroborating what was seen in reference [69] and also discusses how the plateau found and the theoretical infinite time value $\langle P_{\downarrow}(\infty) \rangle$ relate to each other over a wide range of changing system parameters.

We describe the change in both the apparent saturation momentum of the impurity, given by the plateau in $\langle P_{\downarrow}(t) \rangle$ before the momentum revival takes place, and the theoretical saturation momentum of the impurity from summing the time-independent contributions in Eqn (1.19). The time-independent contributions are all elements in the sum where $|f_Q\rangle = |f'_Q\rangle$, as these state pairs are the only ones where the difference in energy is identically 0, and hence the exponential in Eqn (1.19) is constant over all time t . Particular care must be taken when measuring the plateau, as this is the feature of $\langle P_{\downarrow}(t) \rangle$ that most strongly depends on the value of ς reached for the simulation as can be seen in Figures 2.8 and 2.13, to mitigate this, we reach $\varsigma \geq 0.99$ where feasible, and for this section we always normalise by ς achieved, in the manner described in Section 2.2 unless otherwise specified.

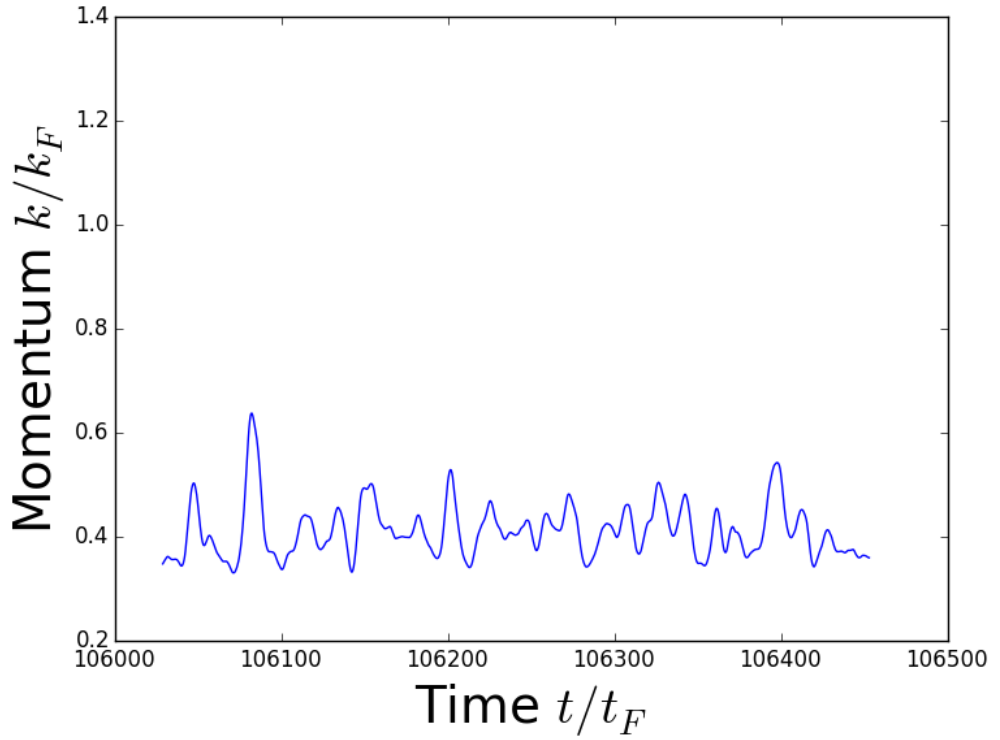
In an infinite system, the plateau would have the same value as $\langle P_{\downarrow}(\infty) \rangle$, but we find there is a difference, which decreases with the size of the system N . This difference decreases with increasing system size with a power law relation as can be seen in Fig 2.14, so the values would be equal in the thermodynamic limit as might be expected. From these differences, we have two different, yet reasonable, values for the infinite time momentum for those system parameters our program can access, which means wherever we inspect this value we have two options to choose from. Where there is a significant difference between the two values, we will mention both in the remaining text.

As noted in Section 2.4, the saturation value of the impurity's momentum changes with both Q and γ (see Figures 2.5, 2.6, 2.15, and 2.16), for both progressions the relation of the plateau matches what is described in Reference [79], but while the progression of $\langle P_{\downarrow}(\infty) \rangle$ is qualitatively the same with changing γ , it is noticeably different with the increase of N and the change in Q . As Q increases, the progression of $\langle P_{\downarrow}(\infty) \rangle$ matches that of the plateau for $Q < k_F$, but is very different once $Q > k_F$, where $\langle P_{\downarrow}(\infty) \rangle$ increases with increasing initial momentum, and the plateau decreases (Figure 2.16). This is another demonstration of how the behaviour of the system is different when Q is above the Fermi momentum. While these two momentum saturation values can be drastically different for a chosen system size, as seen in Figure 2.14, they do tend to each other in the thermodynamic limit.

The manner in which the two values converge, the plateau staying constant as $\langle P_{\downarrow}(\infty) \rangle$ decreases to meet it, is an interesting characteristic, as it implies $\langle P_{\downarrow}(\infty) \rangle$ for an infinite system will eventually reach the consistent value of the plateau, and hence can be found by looking at the plateau for a smaller system. This method can only provide an approximate value for $\langle P_{\downarrow}(\infty) \rangle$, as which point in the quantum flutter corresponds to the limit of $\langle P_{\downarrow}(\infty) \rangle$ is not well defined, making selection of the plateau by eye intrinsically imprecise.



(a)



(b)

Figure 2.12: a) A plot of $\langle P_{\downarrow}(t) \rangle$ for many revivals shows how the momentum revivals initially decohere with increasing time, but the plot of very long $t \gg t_{rev}$ in b) shows that despite this, the momentum at very long term values is not completely stable.

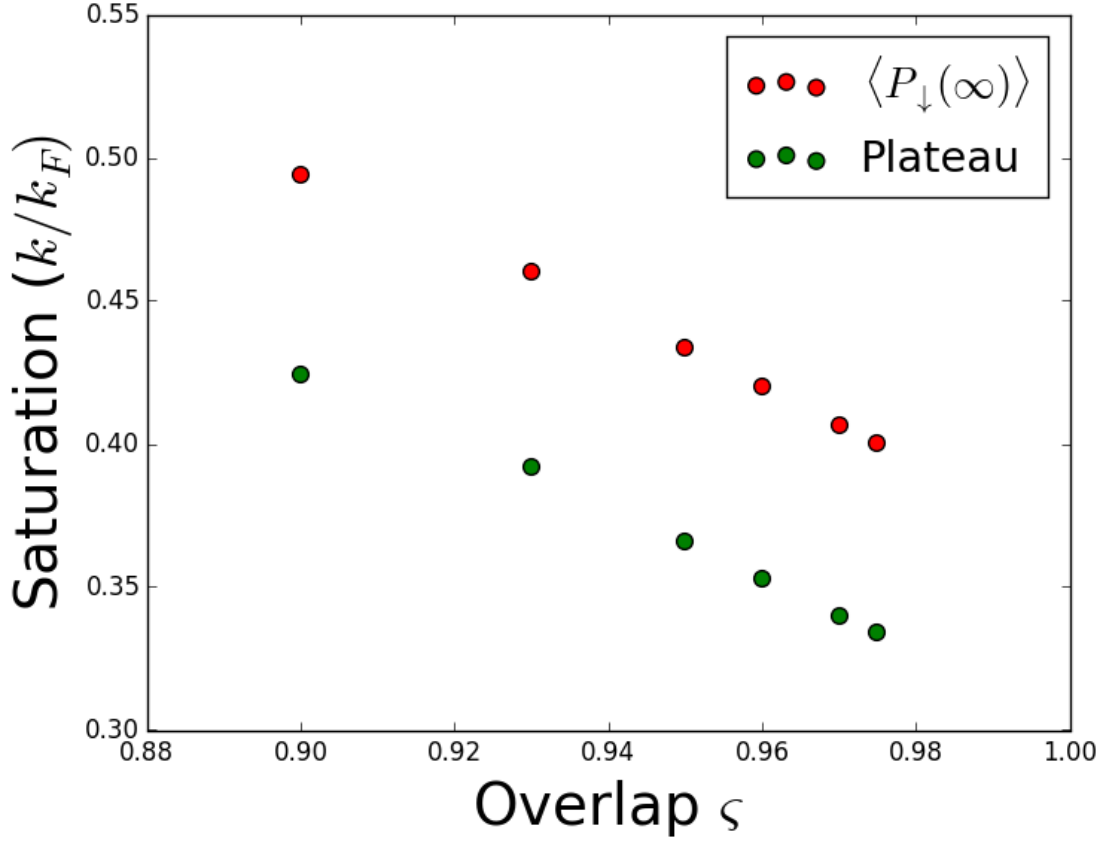


Figure 2.13: Both saturation measures have a near linear dependence on the value of ς reached in the calculation, which can be normalised out to find the limit that would be reached for $N_s = \infty$. The gradient of this progression changes with different parameters, but once the overlap is large enough, $\varsigma \gtrsim 0.95$ then the linearity has always been seen to exist. This graph has been plotted for $N = 45$, $\gamma = 3$, and $Q = \frac{4}{3}k_F$ and does not normalise the results by ς .

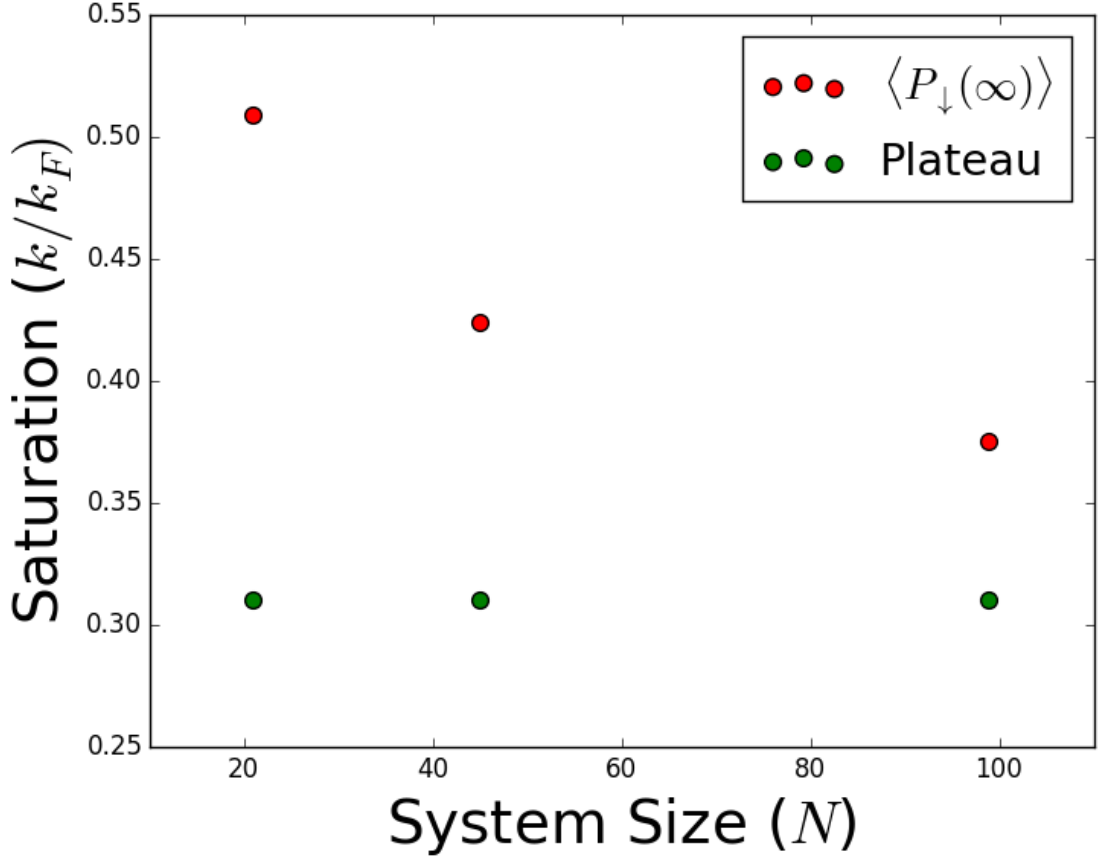


Figure 2.14: Changing time-independent and momentum plateau values with system size for constant $\gamma = 3$ and $Q = \frac{4}{3}k_F$. While the plateau value in the momentum momentum stays constant with system size, the theoretical value is initially much greater than the plateau, and decreases towards it with a power law relation as $N \rightarrow \infty$. Hence, while the momentum of the impurity is not the same as its theoretical thermalised value, this is a finite size effect, and disappears as the system moves into the thermal regime. This fact could be used to obtain an approximate value for the saturation momentum in a thermalised system by finding the plateau of a much smaller system, using less computational resources than otherwise, but measuring the plateau is intrinsically imprecise due to the flutter around it, so this is only useful as an approximation.

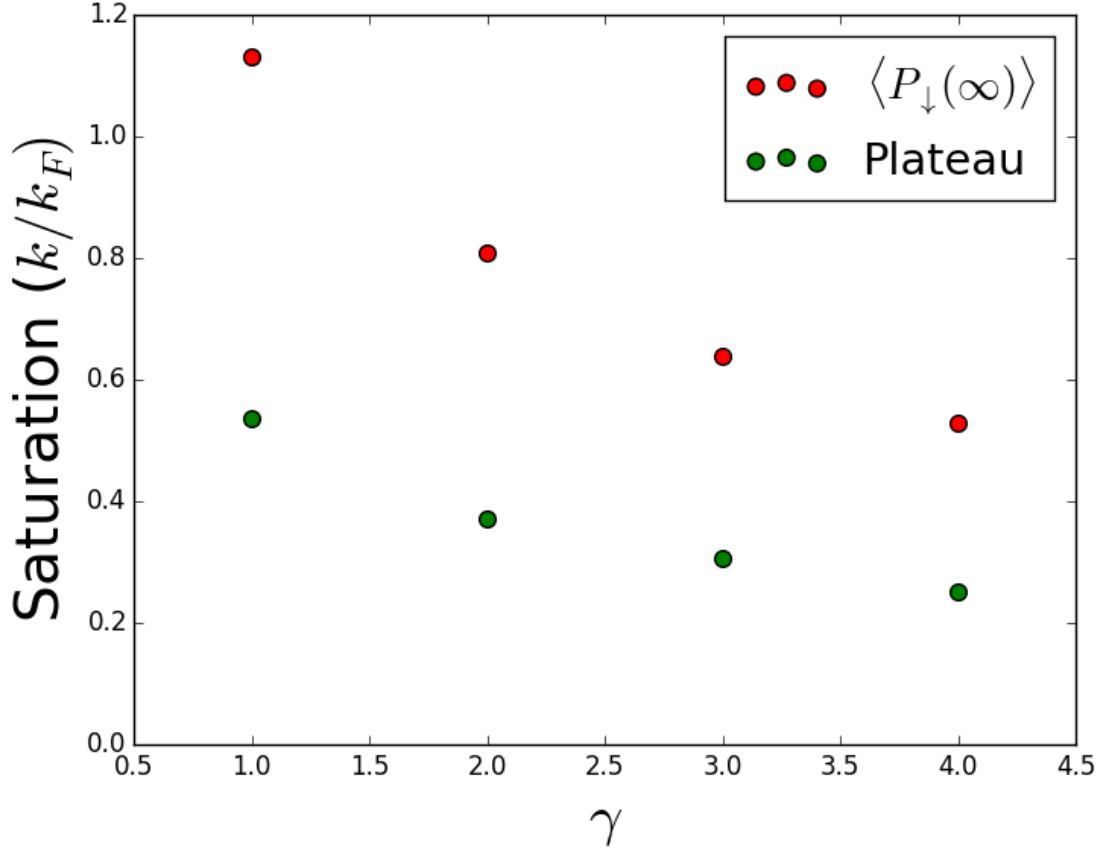


Figure 2.15: How the saturation values are modified by interaction strength γ . As γ diverges, the saturation values both converge to a non-zero value, and to each other. The progression of the theoretical infinite time value was discussed in reference [79], and the current plot shows the same progression. While the plateau is independent of the way γ is chosen, $\langle P_{\downarrow}(\infty) \rangle$, like Eqn (2.2) in Section 2.4, does depend on how γ is formed, with the current plot formed for $L/N = 2$. For $L/N = 3$ the values of $\langle P_{\downarrow}(\infty) \rangle$ follow a progression of the same shape, but between those shown in this figure.

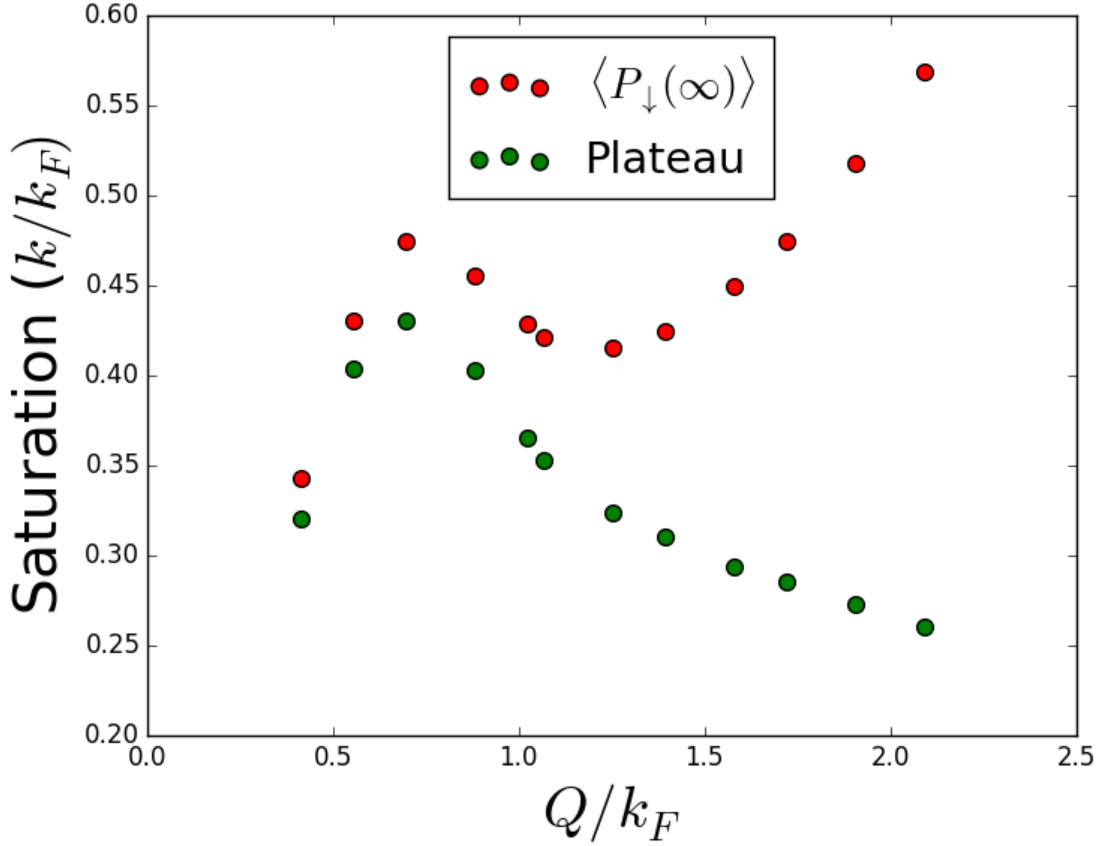


Figure 2.16: The change with Q of both $\langle P_{\downarrow}(\infty) \rangle$ and the momentum plateau. Once the initial momentum is above k_F , the plateau decreases with increasing Q , while $\langle P_{\downarrow}(\infty) \rangle$ increases. There is a maximum in the momentum plateau for an initial momentum some point below k_F as seen in [69]. The difference between $\langle P_{\downarrow}(\infty) \rangle$ and the momentum plateau increases with initial momentum, showing how the interplay between states becomes more important for the impurity's momentum as the initial momentum goes above k_F . The progression of the plateau matches what is seen in [79], the progression of $\langle P_{\downarrow}(\infty) \rangle$ was not mentioned there. This plot was created fixing $\gamma = 3$ and $N = 45$.

2.6 Quantum Flutter

Like the non-zero infinite time value, an oscillation in the momentum of an impurity is an effect that has been discussed in other one-dimensional systems, usually from Bloch oscillations in periodic structures [4, 107]. References [108–110] predicted via quantum hydrodynamics arguments based on the impurity’s dispersion relation, that application of a constant external force to an impurity would create Bloch oscillations in a 1D gas without a periodic potential, though recently the range of parameters for which this result is applicable to a Tonks-Girardeau gas has been under discussion [104, 111, 112].

In contrast to Bloch oscillations, quantum flutter is present in a system with no external potential acting on the impurity. Rather than an external potential, it has so far been attributed to the superposition of plasmon and magnon states with the impurity at momentum $Q \approx k_F$ having lost any excess momentum to the background gas [69, 70]. This physical argument results in an exact equation for the frequency of the flutter in this model [113].

$$\omega_{flutter} = 2k_F^2 \left(\frac{1}{2} - \frac{\gamma^2 \left(\frac{2\pi}{\gamma} + \arctan\left(\frac{2\pi}{\gamma}\right) + \frac{4\pi^2 \arctan\left(\frac{2\pi}{\gamma}\right)}{\gamma^2} \right)}{4\pi^3} \right) \quad (2.3)$$

Notably, the frequency is only dependent on one of the physical parameters we can change, so there should be no change with system size and with initial momentum. We show quantitative agreement with Eqn (2.3) to within the accuracy of our measurements in Fig 2.17, and see the predicted independence on system size and initial momentum.

The dependence of the flutter on the non-physical parameter ς is between the dependence of the revivals in Section 2.4, and the momentum saturation measures in Section 2.5. While the revivals reach a stable value for a relatively small ς , and the saturation momentum requires the ς to be very high (without using the normalisation from Section 2.5), the frequency and amplitude of the flutter both increase until they reach saturation at a ς value that is between those required

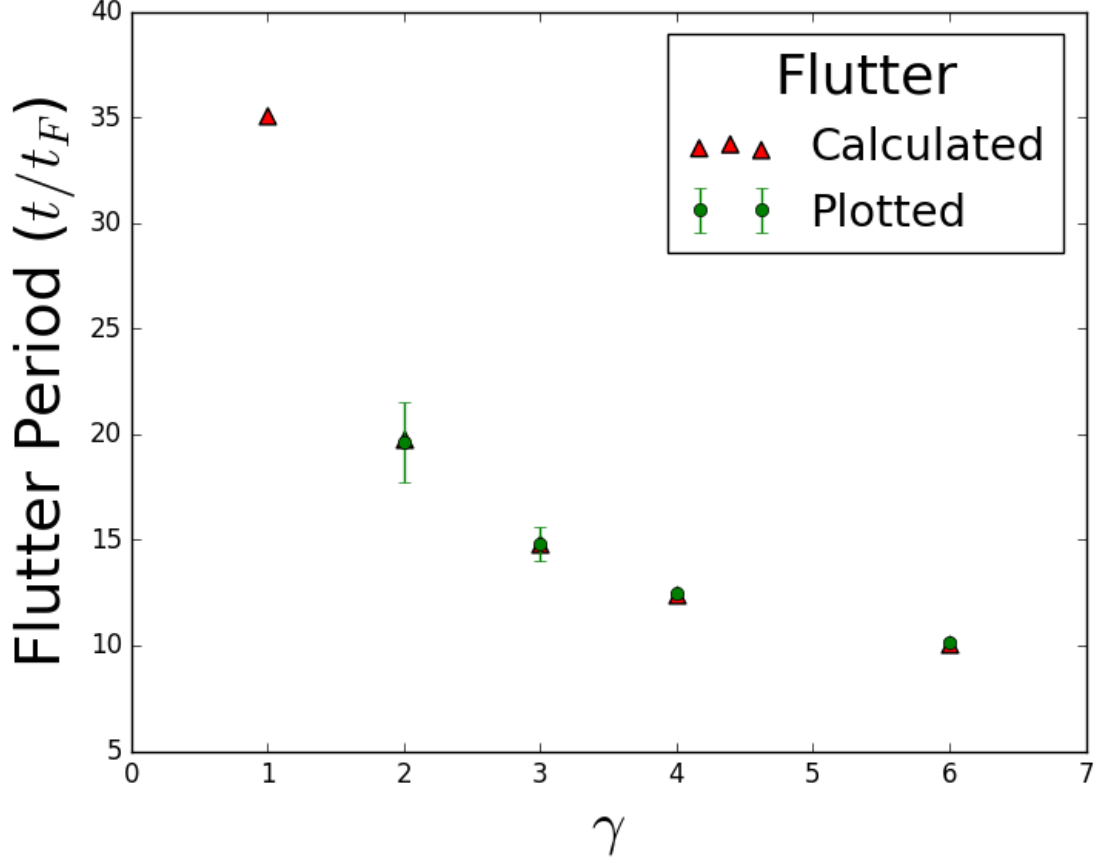


Figure 2.17: The flutter frequency we see matches what is predicted from Eqn (2.3), to a high accuracy, the error bars on the period seen show the maximum and minimum value measured for the flutter, which come from finite size effects obscuring the flutter. Note there is no “plotted” point for $\gamma = 1$ as the oscillation was completely obscured by the revival (as can be seen in Figure 2.6). Despite these difficulties, the flutter period we see closely follows the prediction from [113].

for the other two features (see Fig 2.8). As the flutter saturates before the values of the plateau and $\langle P_{\downarrow}(\infty) \rangle$, this implies there is a subset of state pairs that are the cause of the feature. From the fact the ς required for the flutter to saturate is much higher than what is required to see the momentum revivals, we might guess the eigenstate pairs that cause of the flutter have a lower overlap than those determining the revivals. This hypothesis shall be explored in detail in Chapter 3.

2.7 Conclusion

The features of the momentum evolution for our system are discussed and plotted for a range of system parameters. Agreement is found for all statements in ref-

erences [69, 70], and a further discussion has been made on both the momentum revivals and the change with the non-physical parameter ς . We push the limits of our program to system sizes of $N = 99$ (larger than seen before [69, 70]), showing the quantum flutter and momentum plateau without interference from the revivals. At this system size, we are feasibly restricted to $\varsigma \approx 0.97$ which is not large enough to provide confidence in our results by itself. For further confidence, we present an observation based justification in Section 2.2, where we show that for the systems investigated, the frequency of the momentum revivals reaches a stable point at a very low value of ς , while the flutter requires greater, but still achievable ς to stabilise. Furthermore, while the plateau in the momentum requires a very large ς to stabilise, the consistency of how it changes allows a normalisation for a reasonably accurate prediction of the plateau for systems with a low ς .

The time between revivals in the momentum of the impurity is shown to be qualitatively predicted by a semi-classical argument based on the momentum passed to the background gas and the size of the system, and though the revivals initially disperse, there is no time where they have completely gone away.

Chapter 3

Eigenstates Responsible For Momentum Features

3.1 Introduction

In the previous chapter, we discussed how the impurity's momentum evolution changes with different system parameters, both physical and non-physical. It was seen that the non-physical parameter ς changed the three different momentum features in different ways. The momentum revivals were determined at a low ς , without any noticeable change for $\varsigma > 0.9$, the quantum flutter was determined at a higher value, only settling at $\varsigma > 0.95$, while the position of the momentum plateau did not show any signs of saturation while ς progressed to its asymptotic value. This chapter presents an attribution of state pair subsets to $\langle P_{\downarrow}(t) \rangle$ features, demonstrating how different eigenstate subsets can be described, and showing which subsets cause which features of the momentum evolution. Through this attribution of subsets to features, we will see why the different $\langle P_{\downarrow}(t) \rangle$ features reach stability at different values of ς .

For this chapter we use a large system ($N = 99$) for all graphs, keeping the initial momentum constant at $Q = \frac{3}{2}k_F$, and the interaction strength constant at $\gamma = 3$. A system size this large shows the patterns we will discuss much more

clearly, as the number of states contained is limited by the size of the system in all subgroups we identify. Despite the varying clarity, all patterns shown in this chapter were seen across the range of parameters we can access with our program, with the exception of low initial momentum $Q < k_F$ where some broke down, again showing the qualitative difference between systems with large and small initial momentum. We hence limit all discussions in this chapter to systems where the impurity has been injected with initial momentum greater than the Fermi momentum, which is where the quantum flutter has been predicted.

3.2 The Pseudo Sea

We now describe a concept called the *pseudo Fermi sea* that we will use throughout the rest of the current work to categorise eigenstates. The concept comes from a representation of the Bethe roots, related to the Bethe momenta of Equation (1.15) by

$$z_i = \frac{L}{2} k_i. \quad (3.1)$$

These roots can be represented as

$$z_i = \pi n_i - \delta_i, \quad i = 1, 2, \dots, N + 1 \quad (3.2)$$

where n_i are a unique set of integers, and δ_i are bound within 0 and $-\pi$. Using this representation, the Bethe eigenstates are uniquely determined by the N integers n_i , and as the energy of a state is determined by the sum of the squares of z_i , the ground state has the integers $n_i = \{-(N + 1)/2, \dots, (N - 1)/2\}$.

An analogy can be drawn between this set of integers and the Fermi sea, as you cannot have two identical integers in the set n_i , and the ground state's set fills all the lowest magnitude integer values. We hence refer to this ground set of integers as the *pseudo Fermi sea*. Following this analogy, any excited state must have a number of pseudo particle/hole pairs, where a *pseudo hole* is defined as an integer

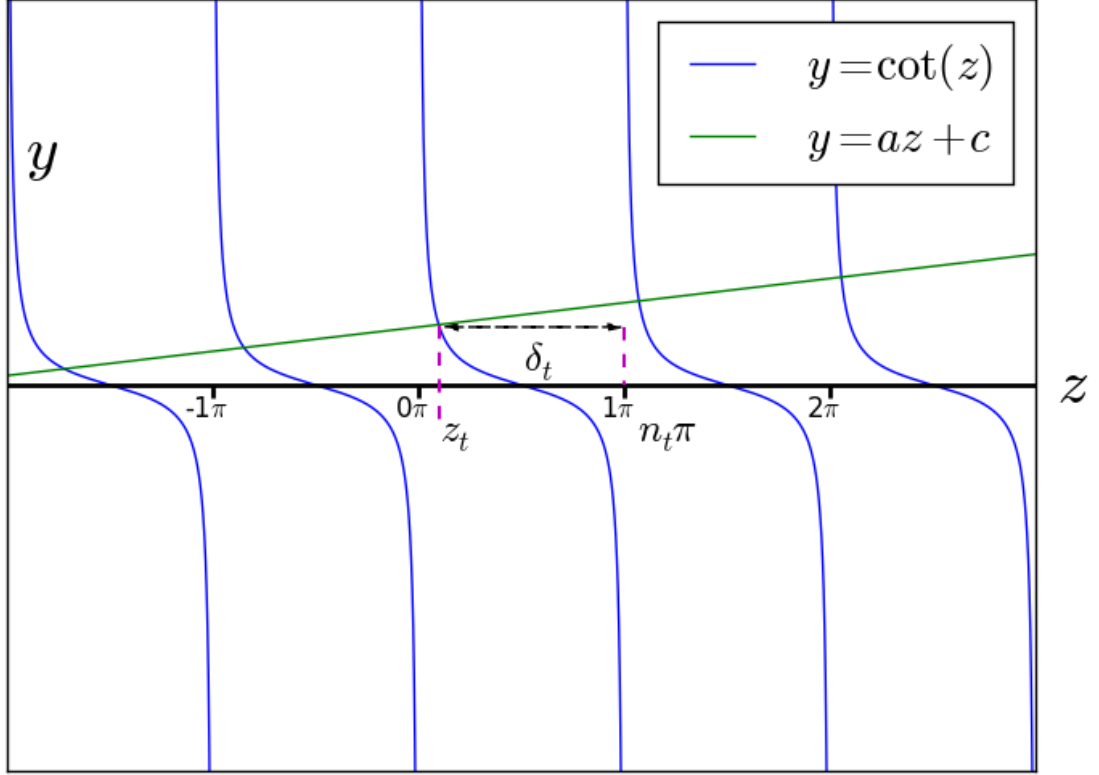


Figure 3.1: The graphical solutions of the Bethe root equations in Eqn (1.15) shows the validity of the representation for the Bethe roots given in Equation (3.2). Each root can be distinguished by the range it is in, and as the gradient of the green line here is fixed by the physical parameters of the system, then the set of ranges in which roots are found uniquely determine the roots themselves.

in the pseudo sea but absent in n_i , and a *pseudo particle* is an integer in n_i , but absent in the pseudo sea. This analogy and terminology is not new [79, 114], but provides some very fitting terms to define the eigenstate pair patterns that make up the bulk of this chapter.

3.3 Eigenstate Families

The plot of energy against $\log_{10}(|\langle FS|f_Q\rangle|^2)$ of each eigenstate shown in Figure 3.2 shows some clear branches, with a few having a much greater contribution to ς than others [95]. In Figure 3.2, (which shows the same type of plot as seen in [95]) each branch consists of two parametric families, consisting of states sharing a pseudo hole. When the pseudo hole of an eigenstate is $(N-1)/2$, it is in the branch with the greatest average overlap. If the pseudo hole is $(N-1)/2 - 1$ then the eigenstate is

in the second most important branch, and this pattern continues for all positive pseudo holes. The other family in each branch is given by those states with a matching *negative* pseudo hole, so states with a pseudo hole of $-(N+1)/2$ are in the same branch as those with a pseudo hole of $(N-1)/2$, and similarly for the two families of pseudo holes $(N-1)/2 - 1$ and $-(N+1)/2 + 1$. Eigenstates with negative pseudo holes tend to have a much lower overlap than those with positive pseudo holes, with all bar one family of these states below the cut off in $|\langle FS|f_Q\rangle|$ used for Figure 3.2. The exceptional family consists of those states with a pseudo hole from the negative edge of the pseudo sea, at $-(N+1)/2$, sharing its branch with the $(N-1)/2$ family, which is the greatest branch in Figure 3.2. For example, if the pseudo sea spans the integers $\{-50, -49, \dots, 0, \dots, 48, 49\}$ then the main branch evident in Fig 3.2 would consist of all states whose pseudo hole is either 49 or -50 , which corresponds to two parametric families, one with the pseudo hole 49, another with the hole -50 . Note that this graph demonstrates the individual states which contribute most to ς have a single pseudo excitation. This is a particular case of a “rule of thumb” in the literature [79, 114] where the contribution to ς from states with a small number of particle/hole pairs is dominant. These branches and families have been noted before, and it has been shown that in the asymptotic limit of $\gamma^2 \log N \rightarrow 0$ and $\gamma^2 N \rightarrow \infty$ the states from just the main family saturate ς [95].

As we know a subset of states can determine the momentum of the impurity at infinite time, and there is a strong pattern in the description of these states within the pseudo particle/hole terminology, a natural question to ask is whether there is a subset within the transitions between these states, and description of that subset, that determine features in the time evolution of the momentum. We shall show how there are in fact two separate (though related) subsets of transitions between eigenstates that together describe the momentum features of the system. One of these subsets describes the overall shape of $\langle P_\downarrow(t) \rangle$, including the plateau at non-zero momentum and the revivals in momentum, while the other describes the

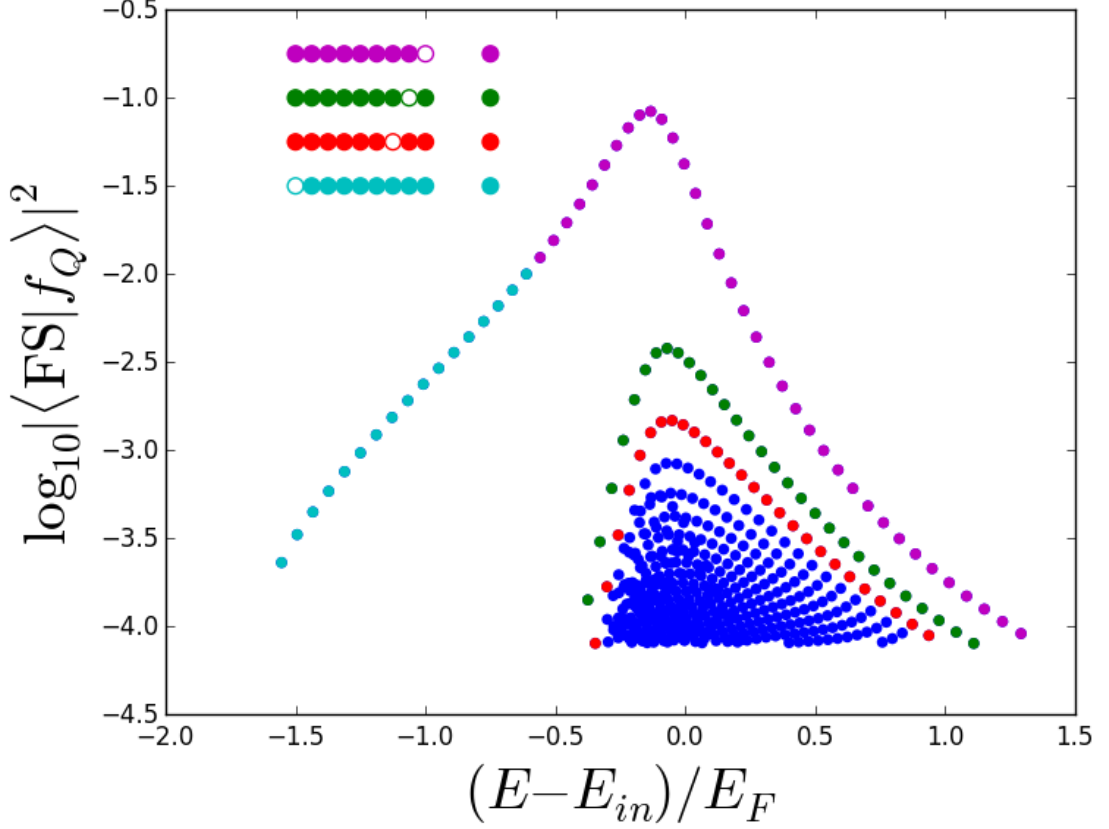


Figure 3.2: The plot of eigenstate energy against importance shows some distinct branches. These branches are comprised of parametric families defined by the pseudo hole each related state shares. For all branches other than the main one (at the top of the figure), the branch is composed of a single parametric family, where all related states have the same pseudo hole. The main branch consists of two families, one where the pseudo hole is on the positive edge of the pseudo sea, $n_{hole} = (N-1)/2$, and one where the pseudo hole is on the negative edge, $n_{hole} = -(N+1)/2$. Each successive branch consists of states from a single family, whose pseudo hole is further inside the pseudo sea the less the average $|\langle FS|f_Q\rangle|^2$, as schematically shown in the top left hand corner. The most important states shown here have a single pseudo excitation, and as a single parametric family is followed from left to right, the pseudo particle is increased by one for each element, the energy of each state being the sum of the squares of Bethe roots z_i where $0 \leq n_i - z_i \leq 1$.

flutter that occurs on top of the plateau. It is the separation of these subsets, and particulars of the state pairs in each, that cause the saturation of these different features to happen at different values of ς , as seen in Chapter 2.

3.4 General Shape

When deconstructing the individual contributions to the momentum of a system, it is natural to investigate the Fourier transform. The particulars of the method we are using make this a trivial task, as it is the Fourier transform we start with, and the momentum is calculated from there (see Equation (1.19)). This also means that each point in the Fourier transform corresponds to a transition between a specific pair of eigenstates which may then be inspected for any pattern in the pseudo particle/hole pairs that describe them.

A typical Fourier transform of our impurity's momentum is shown in Fig 3.3, which has two obvious features to the casual observer. The first is the strong peak at $\omega = 0$ that comes from all contributions in Eqn (1.19) where $|f_Q\rangle = |f'_Q\rangle$, and determines $\langle P_{\downarrow}(\infty) \rangle$ by contributing a time-independent shift in the impurity's momentum. The other is the series of negative amplitude peaks that occur at integer multiples of the revival frequency, with decreasing amplitude as the multiple increases. As the states in the peak at $\omega = 0$ have been discussed in other works [95], and we have presented our own observations on these states in Section 2.5, we now discuss the set of negative amplitude peaks and the state pairs that make them up.

Each point on the Fourier transform comes from a pair of eigenstates. Upon inspection of the state pairs that form these peaks, a simple pattern in the pseudo particle/hole representation can be found. All states, in all state pairs of these notable peaks, come from the main family in Figure 3.2, so they all share with each other N integers in the set n_i and differ in the pseudo particle they have from their excitation. Furthermore, each peak is formed by taking all possible pairs from this subset subject to the constraint that the pseudo particles of the two states are a fixed number apart, where this fixed number corresponds to the integer multiple of the revival frequency that the current peak will contribute. For example, the first peak, coloured red in Fig 3.3, consists of all state pairs where both states come from the main family (i.e. whose pseudo hole is $(N-1)/2$), and

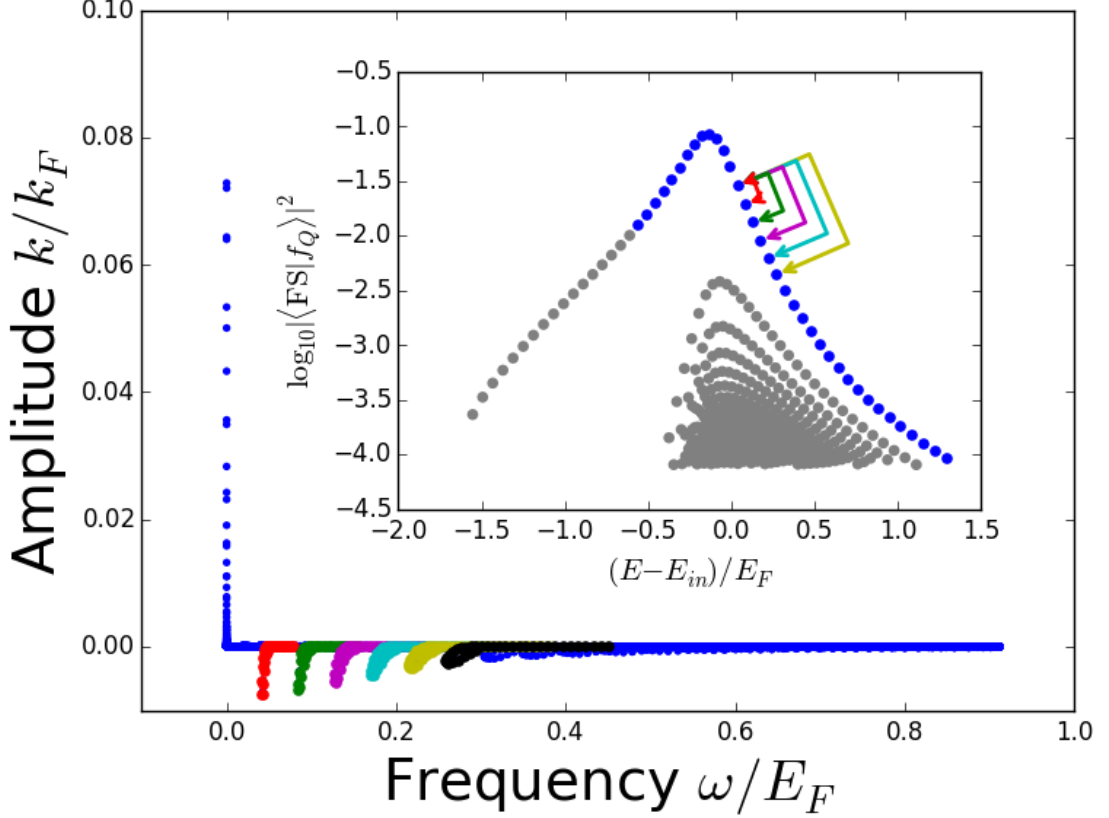


Figure 3.3: The Fourier transform of the impurity’s momentum with inset showing which state pairs cause each small peak. The main plot shows the Fourier transform of the impurity’s momentum against time. Each point here is a contribution from a single state pair to the total $\langle P_{\downarrow}(t) \rangle$. There are two strong features, the large peak at $\omega = 0$ and the set of negative amplitude peaks around each integer multiple of the revival frequency. Inset shows all states with a single pseudo excitation on the same axis as Figure 3.2 (more clearly showing the branches discussed previously), the coloured arrows show example state pairs for some of the coloured peaks in the main plot. In all state pairs from the coloured peaks, both states are in the main family (those not coloured grey), with a pseudo hole of $(N-1)/2$, so the difference between state pairs is only in the difference between the pseudo particles of each state in the pair. Transitions which give the contributions in the first negative peak of the Fourier transform are between states whose pseudo particles differ by one, while transitions causing the second peak are between states whose pseudo particles differ by two. This pattern continues for all the different peaks.

where the pseudo particles of the two states differ by one. Hence the pair of sets $\{n_i^1, n_i^2\}$, $i = 1, 2, \dots, N + 1$ that enumerate each individual contribution to the momentum in Eqn (1.19) and Fig 3.3, are of the form $\{n_i^{base} \cup \{p\}, n_i^{base} \cup \{p + n\}\}$ where p is some integer outside the pseudo sea, n_i^{base} is a shared set of integers, and n is an integer defining which peak this pair is in. This relation is diagrammatically

shown in the inset of Figure 3.3.

An initial analysis of the effect these peaks in the Fourier transform have can be done by viewing the contribution to $\langle P_{\downarrow}(t) \rangle$ that each peak makes in turn. These contributions can be seen in Fig 3.4 and show that each peak combines to add a remarkably smooth wave of period close to some integer multiple of the revival period. Though the contributions have very good alignment for the first few revivals, it is apparent that they become misaligned as time increases.

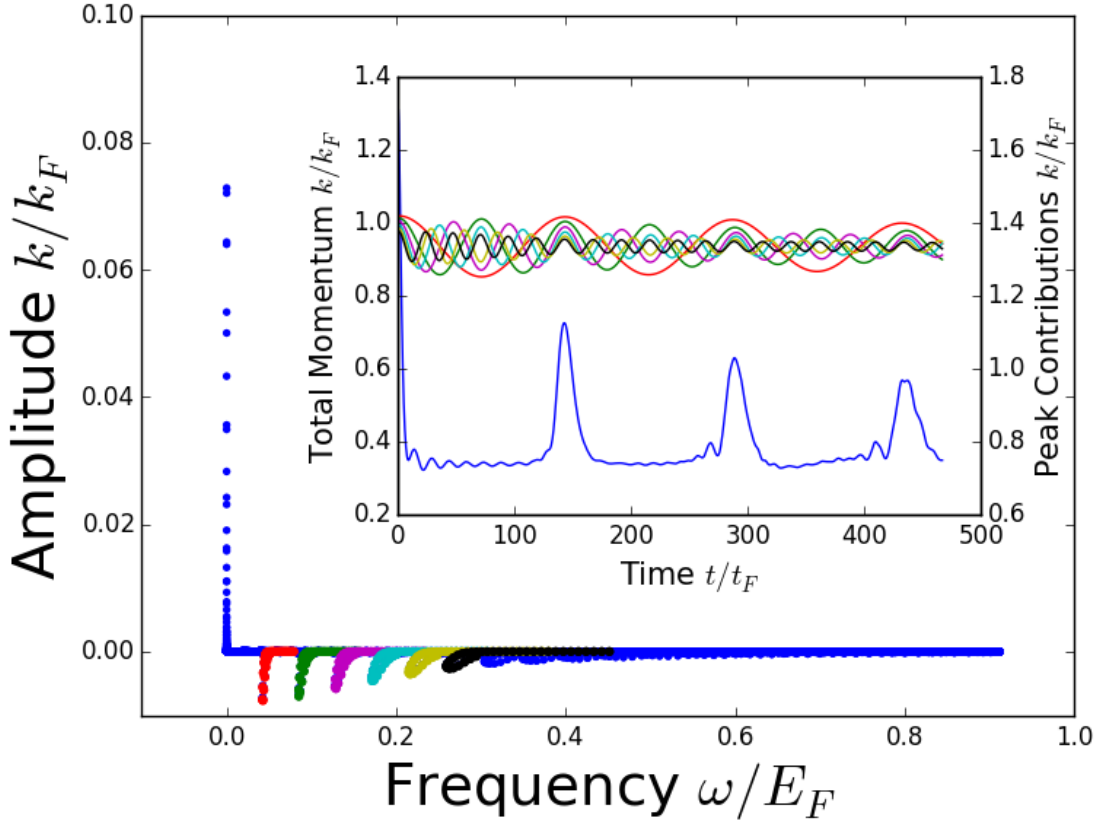


Figure 3.4: The contribution to $\langle P_{\downarrow}(t) \rangle$ from each negative amplitude peak in the Fourier transform. The main plot shows the Fourier transform of the momentum, highlighting each negative amplitude peak, while the inset compares the contribution of each of these peaks to the total momentum evolution of the impurity. The colour of each contribution in the inset correlates with the corresponding colour of the peak in the Fourier transform, and these contributions are plotted on an axis of the same scale, but shifted for clarity. Each peak adds a wave almost harmonic to the revival frequency, and Figure 3.5 shows that their superposition describes both the plateau and the revivals. Figure 3.5 shows this superposition of all peaks describes the general shape of the total $\langle P_{\downarrow}(t) \rangle$, but does not describe the flutter. Figure 3.6 demonstrates the contribution from these peaks to the plateau value of the total momentum is proportional to the ς value reached when just accounting for the eigenstates whose transitions form these peaks.

Combined, the state pairs in all of these peaks plus each diagonal element from the main family (which make up the majority of the peak at $\omega = 0$), constitute all combinations of states selected only from the main family. This contribution is what is plotted in Figure 3.5, reproducing the general shape of $\langle P_{\downarrow}(t) \rangle$, but not the flutter or the exact momentum of the plateau.

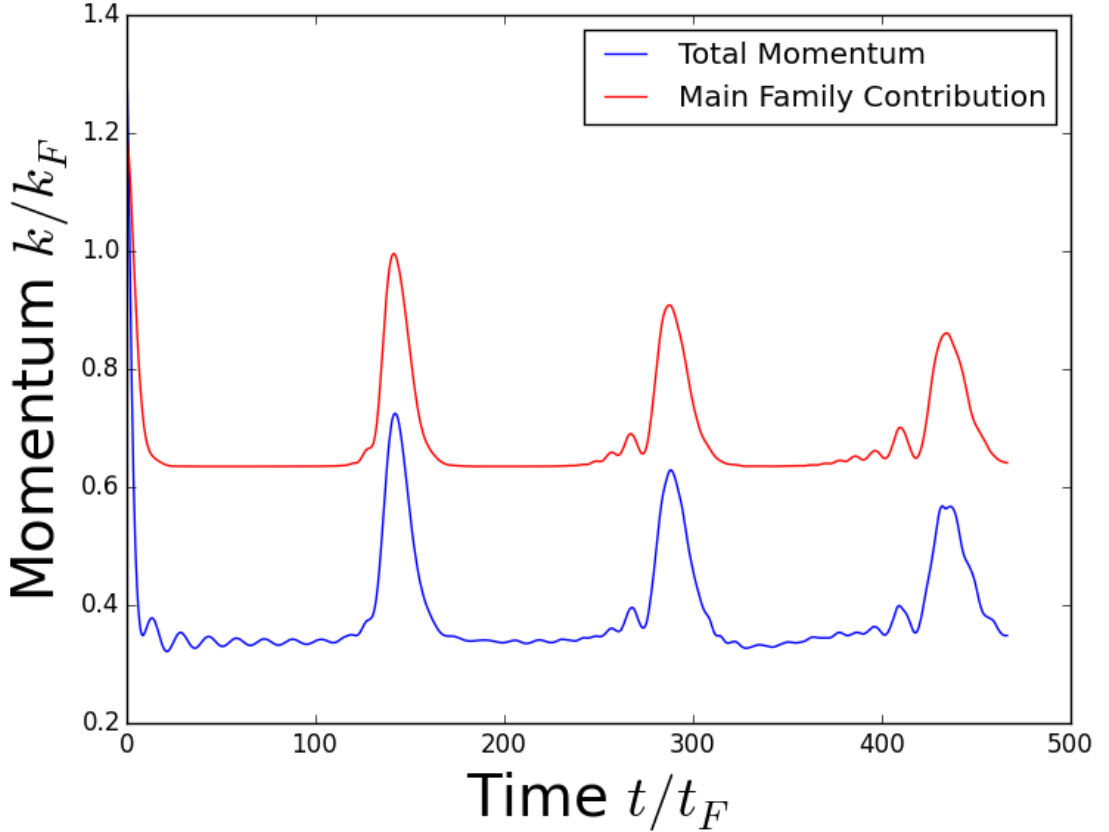


Figure 3.5: Comparison of $\langle P_{\downarrow}(t) \rangle$ to the contribution from all transitions between states in the main parametric family, which is equivalent to the contribution from all peaks seen in the Fourier transform. This comparison shows how this limited number of transitions describes the majority of features in $\langle P_{\downarrow}(t) \rangle$, their contribution provides the majority of the revival amplitude, and there is a non-zero plateau in the momentum. There are notable differences though: the plateau is not at the same momentum as the plateau of the total momentum, and there is no quantum flutter around it.

Because this subset of pairs forms all transitions between a subset of states, we can apply the normalisation from Equation (2.1) to see what momentum would occur were ς saturated by the main family alone. When this is done, we see that the normalisation does not account for the difference in the momentum plateau, with a notable gap between the normalised plateau and that of the total momentum,

showing that this main family does not contribute proportionally to the momentum plateau of the impurity. While the main family does not accurately represent the total, the main branch in the graph of Figure 3.2 consists of two parametric families, one from either edge of the pseudo sea. When both these families are accounted for, i.e. the entire branch is taken into account, the momentum plateau is much better approximated, matching to within the variation from quantum flutter.

In both normalised contributions, the revivals have a greater amplitude than the total $\langle P_{\downarrow}(t) \rangle$, which implies that the main family/branch contributes relatively more to the momentum revivals than other states. The fact the revivals are determined mainly by the transitions between states in the main branch, and hence states that have a large $|\langle FS|f_Q \rangle|^2$, explains why the revivals are determined from a low ς onward, as was seen in Section 2.4. These states are the first to be accounted for, which means the momentum revivals have been found at a very early stage in the saturation of ς . The effects of this normalisation, and hence the representative nature of the main branch, can be seen in Figure 3.6. We talk of how “representative” a momentum contribution from a set of states is to refer to how well it recreates the total momentum once normalised using Equation (2.1). The representative nature of the main branch contribution to the momentum plateau is a useful feature, allowing one to find the value of the momentum plateau only accounting for small subset of states whose description is known beforehand, meaning the calculation time required would be less than the square root of what it would be otherwise. Unfortunately, this feature is limited in scope. While it exists for all system parameters we can probe with this program, in the thermodynamic limit of $N \rightarrow \infty$ with constant $\frac{N}{L}$, the infinite time contribution of the main family tends to 0 while the total $\langle P_{\downarrow}(\infty) \rangle$ does not (see Section 4.2). It is of interest to note that the contributions from all the parametric families and branches seen in Figure 3.2 are similar, reproducing the general shape of $\langle P_{\downarrow}(t) \rangle$, however, the amplitude of each contribution decreases with the impor-

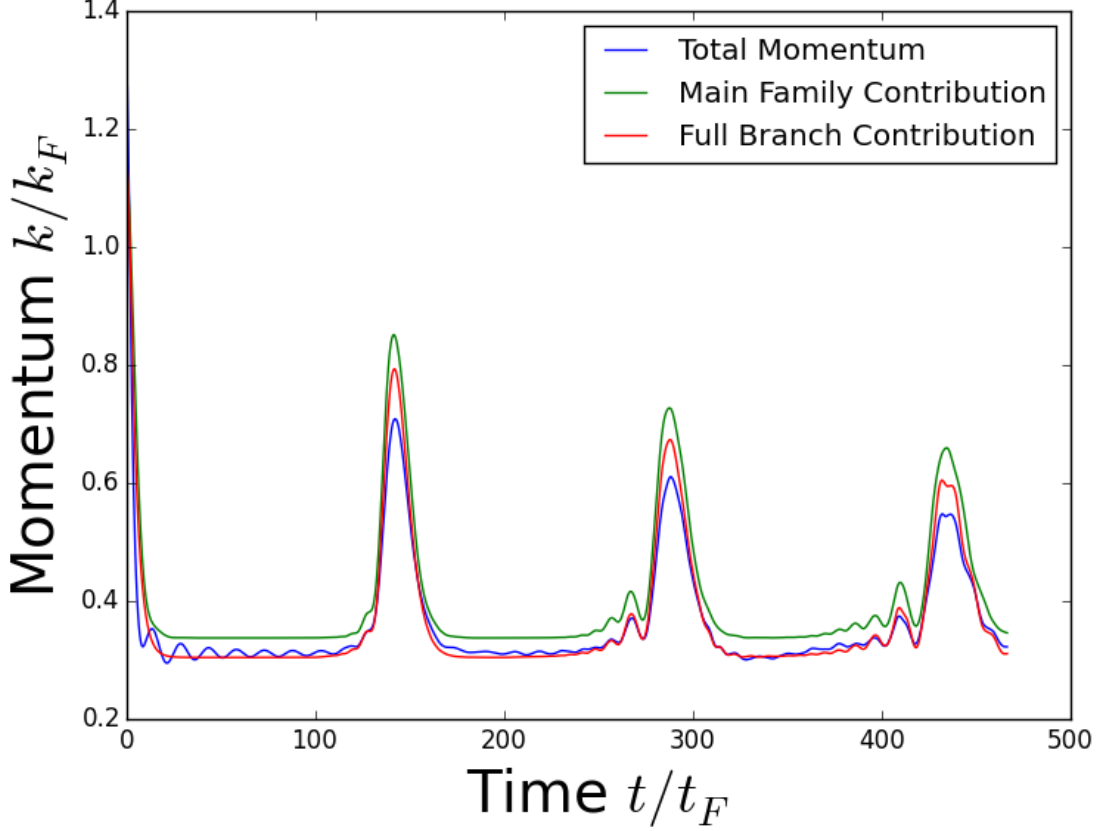


Figure 3.6: Comparison between the normalised contributions of the main parametric family, main branch in Figure 3.2, and all states calculated for a typical system. The normalised branch reproduces the plateau of the entire $\langle P_{\downarrow}(t) \rangle$ quite well, while the main parametric family does not. Both the normalised contributions from the main family and main branch have a greater revival amplitude than the actual $\langle P_{\downarrow}(t) \rangle$, demonstrating that they contribute relatively more to the momentum revivals than other states.

tance of the states, and the resulting contributions are less representative of the total. The contribution of each branch normalised by Eqn (2.1) is compared to the total momentum in Figure 3.7. While the general shape stays constant, there are notable differences. The period of the revivals is slightly larger for lesser families, the normalised amplitude of the revivals decreases, and the momentum plateau of the normalised contribution is further from the total. This shows that these families with lower $|\langle FS|f_Q \rangle|^2$ not only contribute less overall than the main one, but they also contribute less proportional to their contribution to the ς saturation. I.e. when normalised by Equation (2.1) their contribution to the total momentum is still less than the similarly normalised contribution of the main family. When

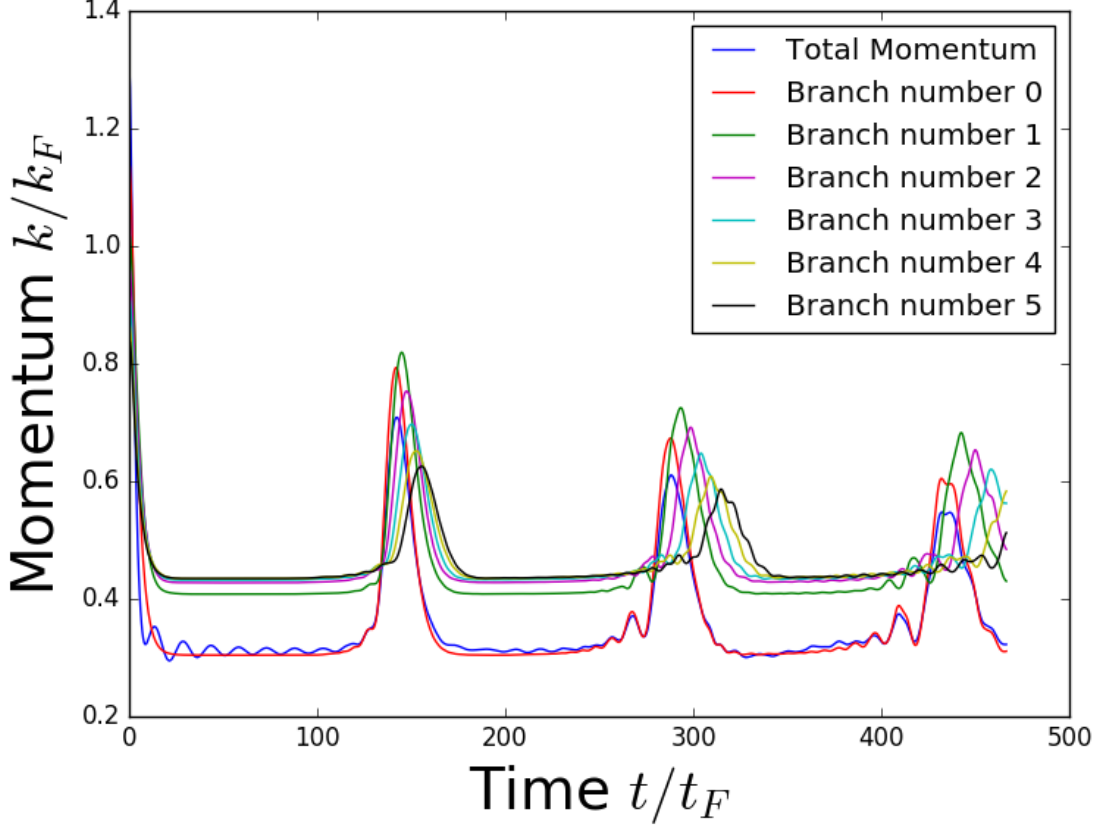


Figure 3.7: Comparison between the normalised contributions of each branch from Figure 3.2 and the total momentum contribution. Each contributes a similar shape to the momentum, though without the normalisation of each branch the shape of most would not be visible here. The gradual increase in the revival period can be attributed to the fact that the less important branches seen in Figure 3.2 have points closer together on the energy axis.

combined, the contributions from all intra-branch pairs in the parametric families create a better approximation of the momentum plateau than the main branch alone, but the normalisation applied previously cannot be applied again as this contribution does not come from all transitions within a subset of states.

The good results obtained by normalising the contribution of states in the main branch of Figure 3.2 using Equation (2.1) neglect the contribution coming from the majority of states. Using the numerical observation that the value of $\langle f_Q | P_{\uparrow} | f'_Q \rangle$ for a given state $|f_Q\rangle$ is greater when $|f'_Q\rangle = |f_Q\rangle$ than otherwise, a better approximation of the total momentum can be obtained. This approximation is made by taking the full contribution of the same subgroup of transitions as before, but rather than normalising this contribution using Equation (2.1), other states are

accounted for using just their time-independent contribution. While accounting for these extra contributions is much more time-intensive, it produces a better approximation of the total momentum evolution, especially near the momentum revivals. This can be seen in Figure 3.8, which compares the two approximations with the total, and again in Figure 3.13 where the same type of approximation is used. This alternate approximation provides a better estimate of the momentum

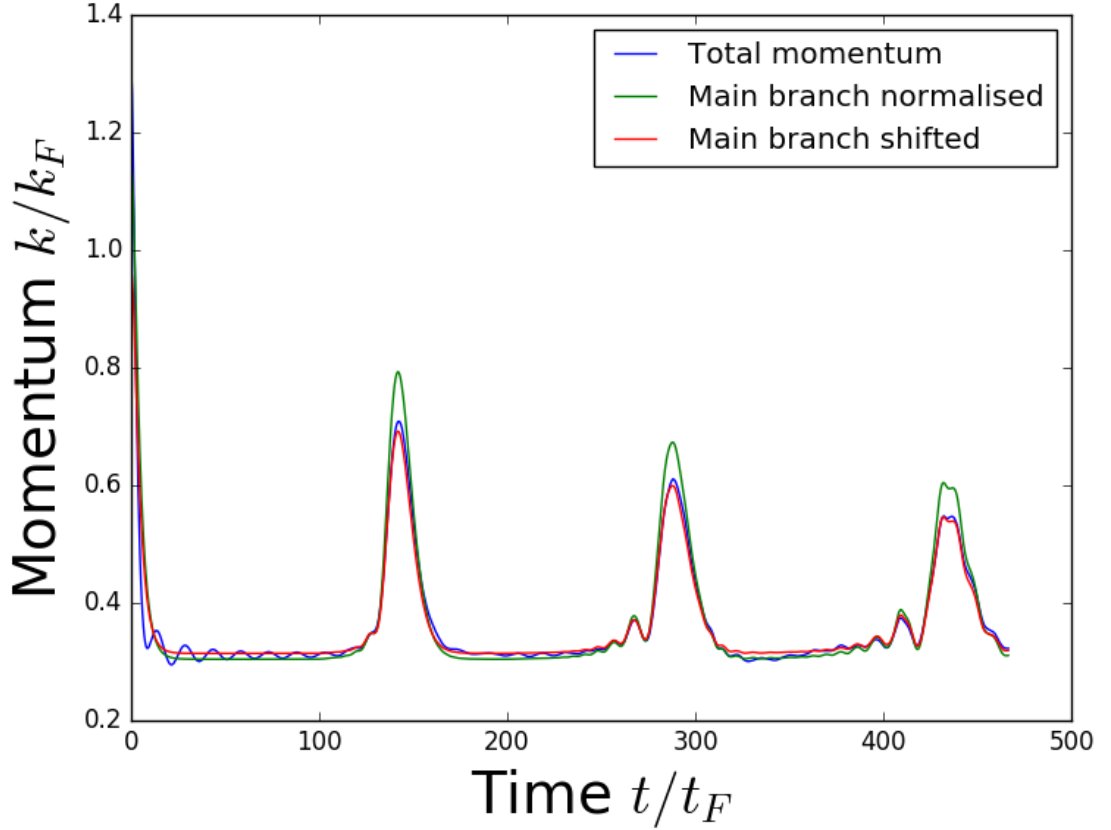


Figure 3.8: Comparison of the approximations gotten from normalising the main branch contribution via Equation (2.1) to that of adding the time-independent contribution of other states to the full contribution of the main branch. Accounting for the time-independent contributions of all states provides a better approximation around the momentum revivals.

plateau at lower initial momenta Q , as shown in Figure 3.14, where various plateau approximations are presented for a range of different Q .

3.5 Flutter

The last section showed that the overall shape of $\langle P_{\downarrow}(t) \rangle$ comes from all transitions where both states come from the same branch of Figure 3.2. This section will demonstrate that the oscillation dubbed “quantum flutter” is a feature resulting from pairs of states where each is in a different branch. While the Fourier transform highlighted the states most culpable for the general shape, we found no feature around the quantum flutter frequency in any relation we looked at. This is because the eigenstates from the branches discussed in the previous section dominated the structure of any plots taking into account all eigenstates.

It can be reasoned, given that eigenstates with a single pseudo excitation are the greatest contributors to $\langle P_{\downarrow}(t) \rangle$ and transitions between states in the same branch from Figure 3.2 describe the general shape of the impurity’s momentum without the flutter, that the flutter may come from transitions between states in different branches of Figure 3.2. This conjecture is borne out in Figure 3.9, where the contribution of the inter-branch transitions can be seen to match the flutter of the total $\langle P_{\downarrow}(t) \rangle$, barely contributing any overall shift of the impurity from the initial momentum of $\frac{4}{3}k_F$. The fact that flutter comes from these inter-branch transitions can be used to explain the observation that the quantum flutter saturates at a ς of about 0.95. The phenomenon of quantum flutter requires including many of the parametric families from Fig 3.2, but does not depend on any states that have more than a single pseudo excitation. This means that a large number of states must be accounted for to describe the flutter, but these are states that are accounted for first by the sampling algorithm of our code.

While this identification of the contribution to the flutter as the inter-branch transitions between singly excited states does cut the computational resources required to investigate this feature, this is still a large subset compared to that which we found was representative of the general shape in Section 3.4. We can find a much smaller group that still reproduces the flutter frequency using an analogy to the parametric families discussed in Section 3.3, whose intra-branch transitions

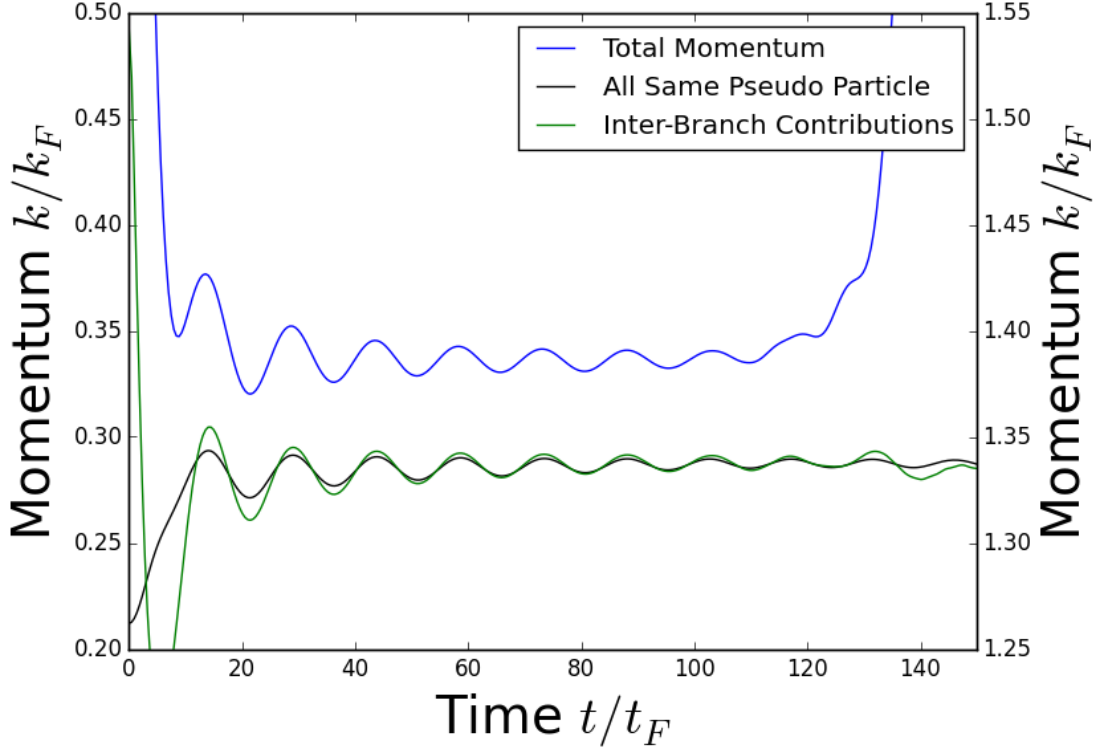


Figure 3.9: Plot comparing the quantum flutter in the total momentum evolution with the contributions to the momentum from transitions between state branches, and contributions from transitions between states in different branches, but sharing a pseudo particle as highlighted in Figure 3.10. The total quantum flutter is reproduced by all inter-branch transitions, and the restricted set of transitions between states sharing a pseudo particle reproduces the frequency, and most of the amplitude of the flutter.

were shown to determine the general shape of the impurity's momentum evolution in Section 3.4. Those representative families were defined by the set of states that share their only pseudo hole, and we find that transitions between states which share their only pseudo particle (and have different pseudo holes) determine the flutter around the momentum plateau. Hence, the transitions which cause the majority of the flutter are between pairs of states that can be represented as $\{(n^{ground} \setminus \{h\}) \cup \{p\}, (n^{ground} \setminus \{k\}) \cup \{p\}\}$, where n^{ground} is the set of integers defining the ground state, h and k are integers defining the pseudo hole missing in each state, and p is the integer defining the pseudo particle that both states share. In this representation, all three of h , k , and p can change while the state pair is still in the set of contributing transitions. Examples of these sets are highlighted in Figure 3.10, which shows the same plot as Fig 3.2, but filters out

states with more than one pseudo particle/hole excitation, and is cut off at a lower $|\langle FS|f_Q\rangle|^2$. While we could normalise the contribution from one of these sets, the combination of all transitions from each of these sets is not normalisable, hence we show the unnormalised contribution to $\langle P_\downarrow(t)\rangle$ from intra-set transitions in black, and compare it to the unnormalised total $\langle P_\downarrow(t)\rangle$ in Figure 3.9. The contribution

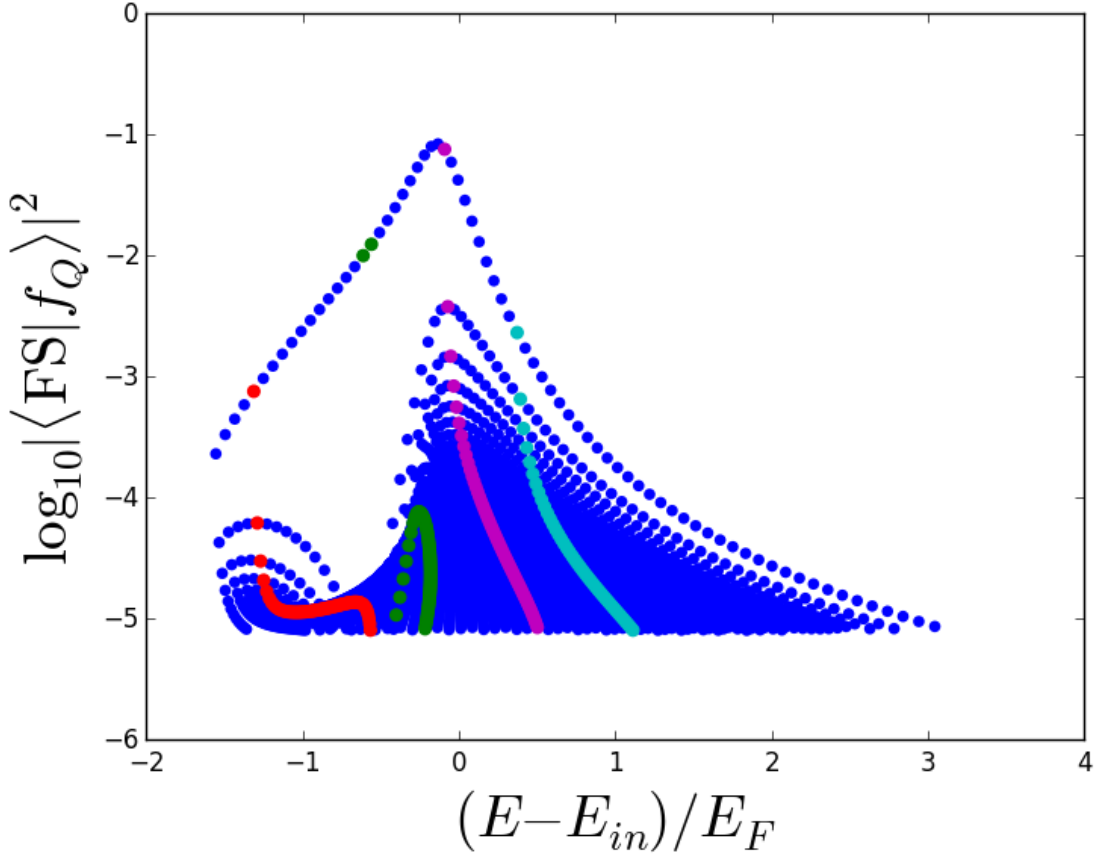
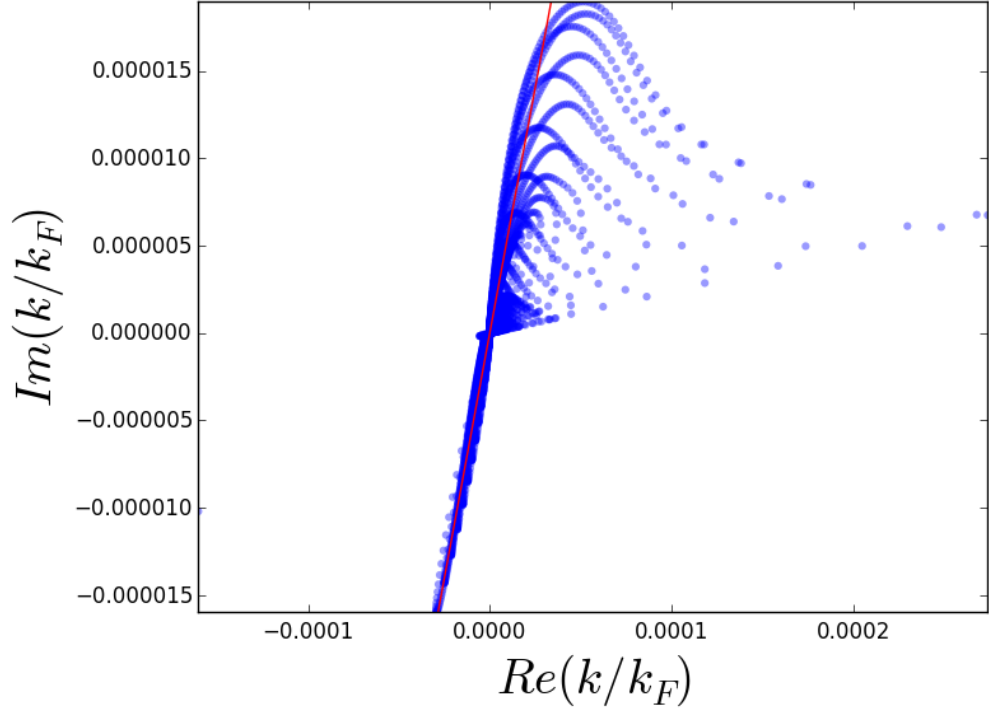


Figure 3.10: All singly excited states with a $|\langle FS|f_Q\rangle|^2$ above a certain threshold. Some parametric families different to the type discussed before are highlighted in colours other than dark blue. In these parametric families, related states share a pseudo particle and have different pseudo holes. To avoid confusion, we will not refer to these sets as parametric families in the text. Intra-family transitions from these families create the major contribution to the quantum flutter in $\langle P_\downarrow(t)\rangle$. While one family of the type described in Figure 3.2 clearly contributes more to $\langle P_\downarrow(t)\rangle$ than others, the contributions of the families shown here are relatively similar, and we cannot isolate a single one as providing the main contribution to the flutter.

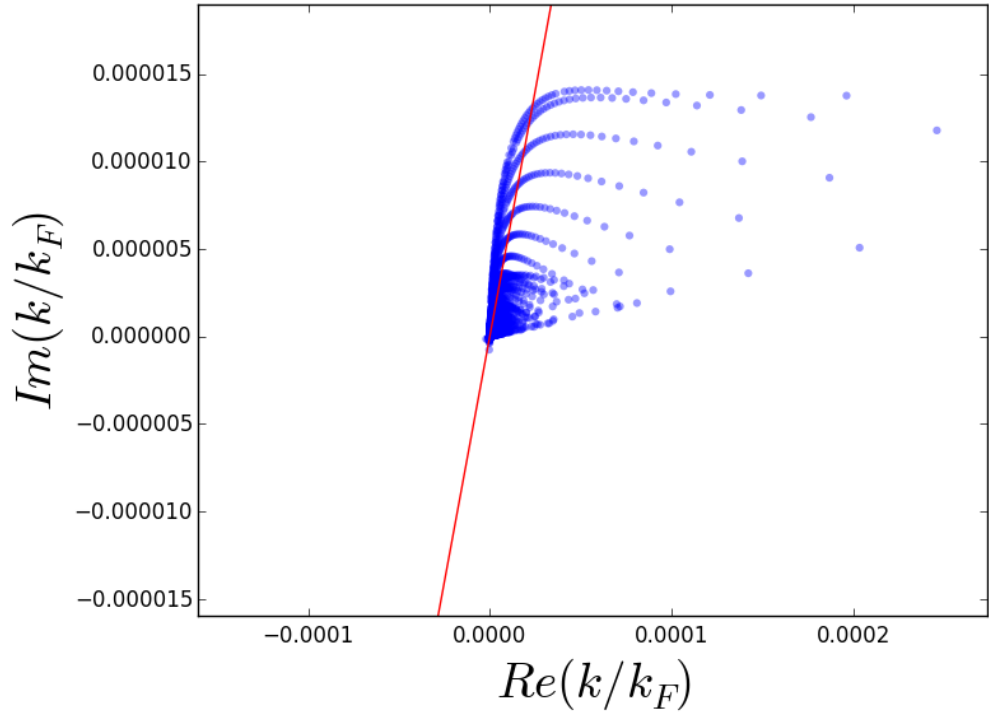
from those state pairs whose pseudo particles differ by one, two, or more has the same oscillation as shown in Figure 3.10, but with an ever decreasing amplitude as the pseudo particles are further apart.

When looking for patterns in the individual contributions before, the Fourier transform highlighted some contributions which could be used to describe the general shape of $\langle P_{\downarrow}(t) \rangle$. Using the same technique on those contributions identified as the main contributions to the flutter is not as helpful, as the largest contributions in the subset we have identified are not at the flutter frequency. A more effective visualisation of these state pairs is to plot the real and imaginary parts of each term on the RHS of Eqn (1.19) that comes from state pairs sharing a pseudo particle for a fixed time $t = 1$. This plot is effectively a polar plot, with the radius of each point determined by the amplitude of the term, and the angle anticlockwise from the positive real axis determined by the term's frequency. Two examples of such plots are shown in Figure 3.11, one from a system with a high initial momentum $Q > k_F$ and one with $Q < k_F$. Note that in Figure 3.11 we have limited the contributions to those with positive frequency for clarity in the graphs. This is done without loss of information, as each contribution is symmetric with respect to the order of the eigenstates, having equal amplitude and opposite sign frequency. These plots show another form of branch, and again, each branch consists of all entries in some parametric family. Each family of state pairs in these plots share an eigenstate, and since in every contribution shown, the states share their pseudo particle, moving along the family only changes the pseudo hole of the transitions second state. The greatest amplitude families come from the greatest amplitude individual states, and all have a frequency that is less than $\pi/4$, so the visible states with positive imaginary and real parts all have positive amplitude and those with negative imaginary and real parts have negative amplitude.

In Figure 3.11a, we see how, despite the greatest amplitude contributions coming from states with a much smaller frequency than the flutter, there is a large, negative amplitude peak around the flutter frequency. This peak consists of those families whose fixed state has a pseudo hole on the negative edge of the pseudo sea, i.e. the fixed state defining the new branch is in the negative edge parametric family of type described in Section 3.3.



(a)



(b)

Figure 3.11: The plot of the imaginary and real parts of the terms in Eqn (1.19) for those state pairs found to be major flutter contributors. a) While the contributions with the greatest amplitude are far from the flutter frequency, there is a strong peak around that frequency coming from state pairs where one state is excited from the negative edge of the pseudo sea. b) For a small initial momentum $Q < k_F$, the structure of the Bethe Ansatz means states excited from the negative edge with a positive particle can't exist, so the branches are lost. In both plots, the red radial line denotes the flutter frequency.

Using the insight given to us by Figure 3.11 where the greatest amplitude states with a frequency near that of the flutter observed come from an even smaller subset of those state pairs identified previously, we plot the sum of the contributions from transitions in this peak. Figure 3.12 shows just taking those state pairs where one of the states has a pseudo hole on the negative edge of the Fermi sea doesn't actually decrease the flutter contribution further from that obtained when limiting the state pairs to those sharing a pseudo particle. With this final filter we have found a subset of state pair contributions that describe the flutter, at a lower amplitude to the total, yet require accounting for a much smaller number of contributions in Equation (1.19).

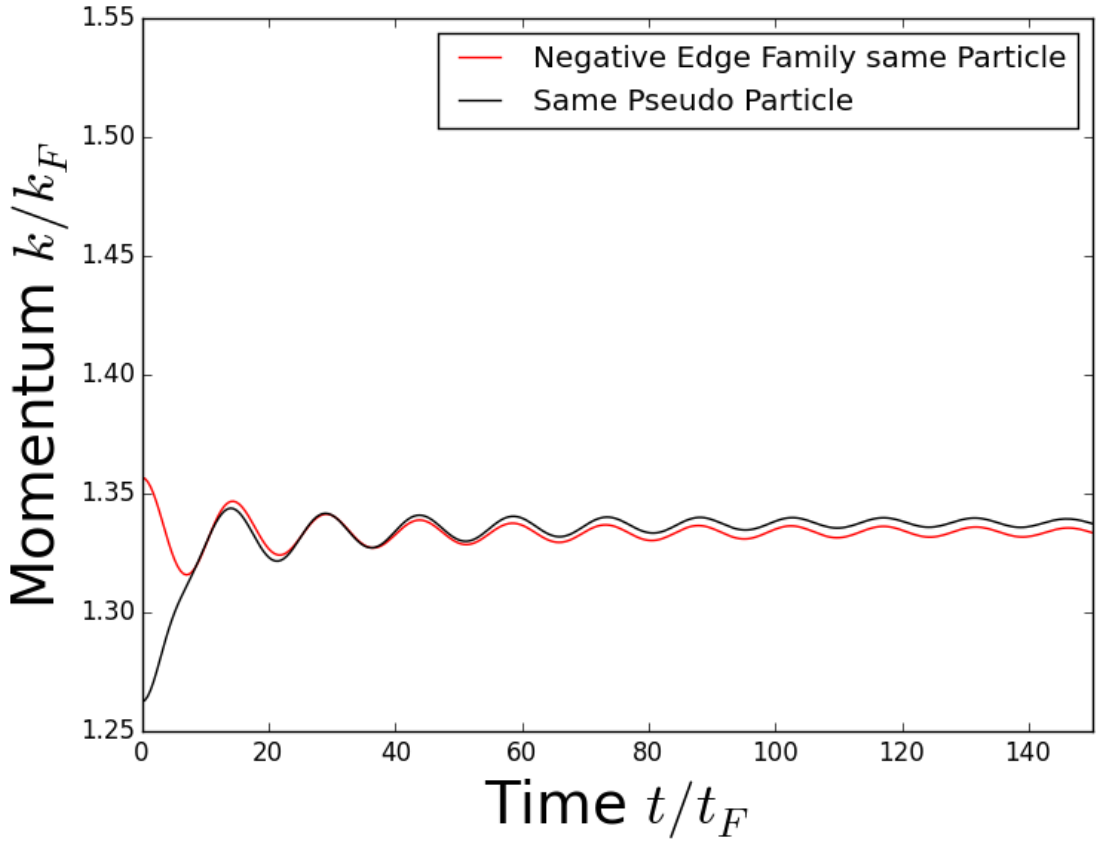


Figure 3.12: Comparison of the contribution from all state pairs sharing a pseudo particle, to the further subset of these state pairs where one of the states has its pseudo hole as the negative edge of the pseudo sea. The oscillation that relates to the flutter is the same between these two subsets, sharing both the amplitude and frequency. This shows how the state pairs contributing to the flutter in the subset of state pairs who share a pseudo particle all have one state from the negative edge of the pseudo sea.

It should be stressed that though this small subset of transitions reproduces the flutter frequency, there are other contributors within the larger subset of inter-branch transitions that increase the amplitude of said oscillation. When the initial momentum is only slightly greater than the Fermi momentum, these states contribute more to the amplitude than otherwise, and though the transitions to and from states on the negative edge between others with the same pseudo particle still reproduce the frequency, the proportion of the flutter observed is less.

In the previous sections we have shown that the main contribution to both time-dependent features of the system come from transitions between states which only have a single pseudo excitation. In order to stress this point, Figure 3.13 compares the total momentum evolution of the system to what occurs when assuming the time-dependent contribution of all states with more than a single pseudo excitation is 0. This is done by taking all transitions between singly excited states, and adding to that the time-independent contribution of all other states.

The approximations presented in this section are generally only useful in the regime where $Q > k_F$. The shape of the momentum evolution and the plateau obtained using the normalisation approach become unacceptably inaccurate when $Q < k_F$. However, the plateau approximation from discarding the time-dependent contribution of states outside the two main subgroups identified here is still reasonably accurate, as demonstrated in Figure 3.14.

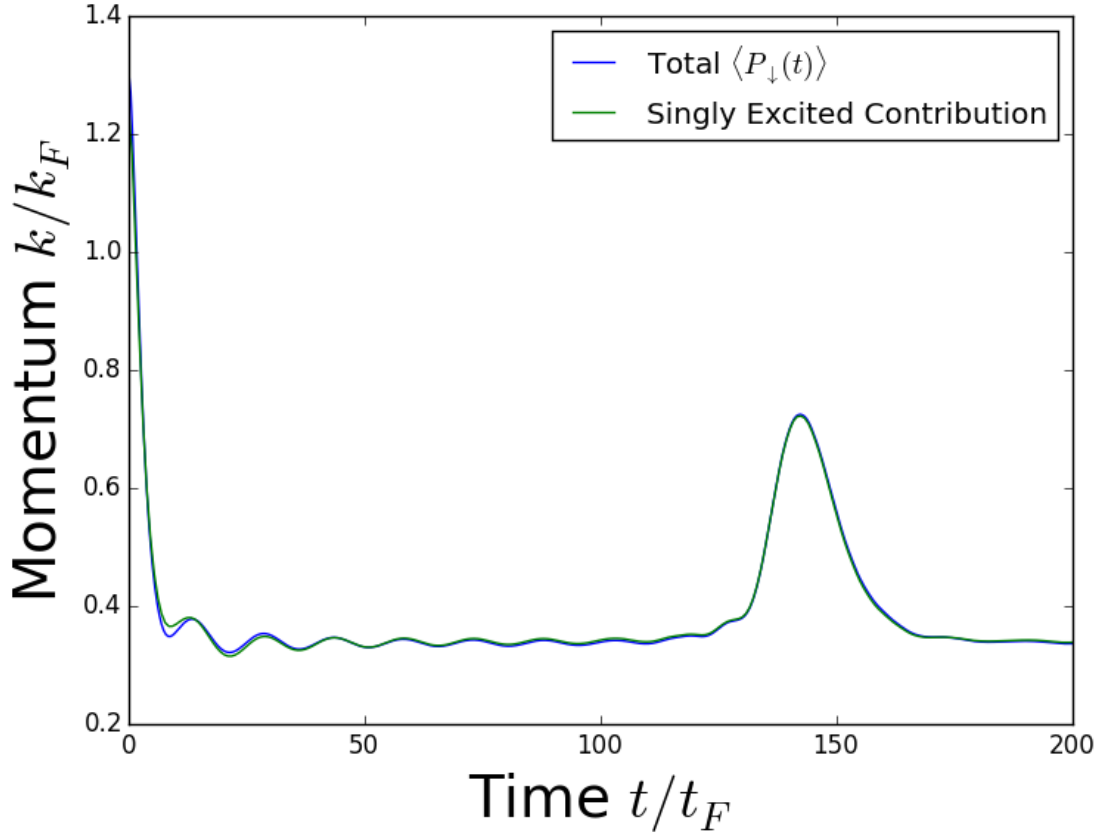


Figure 3.13: Comparison of the unnormalised total momentum evolution of the impurity to the momentum evolution that comes from assuming the only time-dependent contributions come from transitions between states with a single pseudo excitation. While the plateau of the approximation is not as level as the total, the majority of all features are shown, with both the flutter and revivals presenting good approximation in both amplitude and frequency.

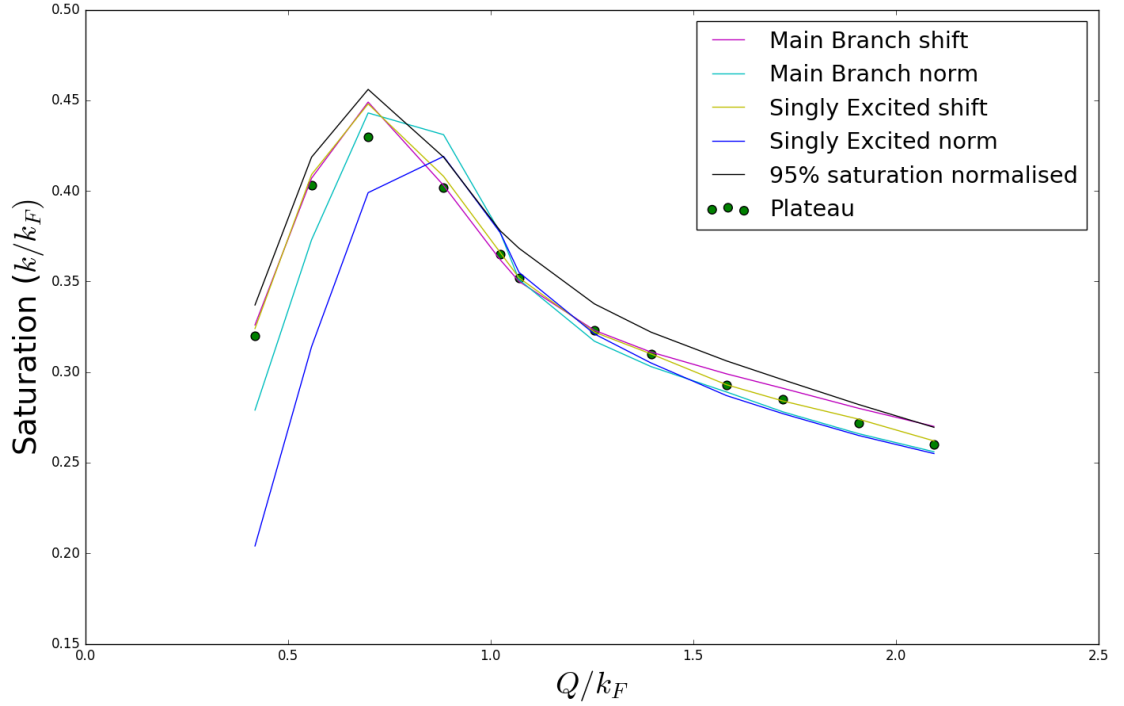


Figure 3.14: The plateau values of different approximations and their progression with the initial momentum Q . We can see that the approximation from normalising a subgroup defined via pseudo excitation patterns becomes progressively less accurate as the initial momentum of the impurity decreases. On the other hand, the approximations from taking account of the time-independent contributions of all states still provides a reasonable plateau value. Moreover, normalising the contribution found from only obtaining a saturation of $\varsigma = 0.95$ also provides a reasonable plateau over all initial momenta Q .

3.6 Conclusion

While reference [95] showed that in the limit $\gamma^2 \log N \rightarrow 0$ and $\gamma^2 N \rightarrow \infty$, states in the main family saturate the sum rule, we demonstrate that for those system parameters reachable by our program, transitions within these states describe the overall shape of the impurities momentum. More generally, we show transitions between states in a branch contribute to the general shape of the momentum evolution and transitions between states in different branches contribute to the flutter, with their combination describing the non-negligible contributions to the time dependent motion of the impurity. I.e., the set of contributions from intra-branch transitions, where a branch is defined by the pseudo hole of an excitation, determines the overall $\langle P_{\downarrow}(t) \rangle$ shape, while the contributions from inter-branch transitions determine the flutter.

Within those transitions causing the flutter, the main contribution comes from transitions between state pairs where one state has its pseudo hole on the negative edge of the pseudo sea, and both states have the same pseudo particle. Similarly, the main contribution to the general shape can be found from those state pairs where both states are in the main family. A final decomposition can be made, as the revival frequency is seen from contributions between states in the main family which differ by a nearest-neighbour displacement of one pseudo particle.

These observations can be used to approximate any individual feature of the momentum evolution with a much smaller computational expense than has previously been possible, paving the way to more research on the physics of the system without as much focus on how said physics must be calculated. From the approximately $\binom{N^2}{2}$ state pairs that come from all states with a single pseudo excitation, we have identified two distinct subsets of approximately N^2 states which can be used to find each of the different features of the impurity's momentum evolution.

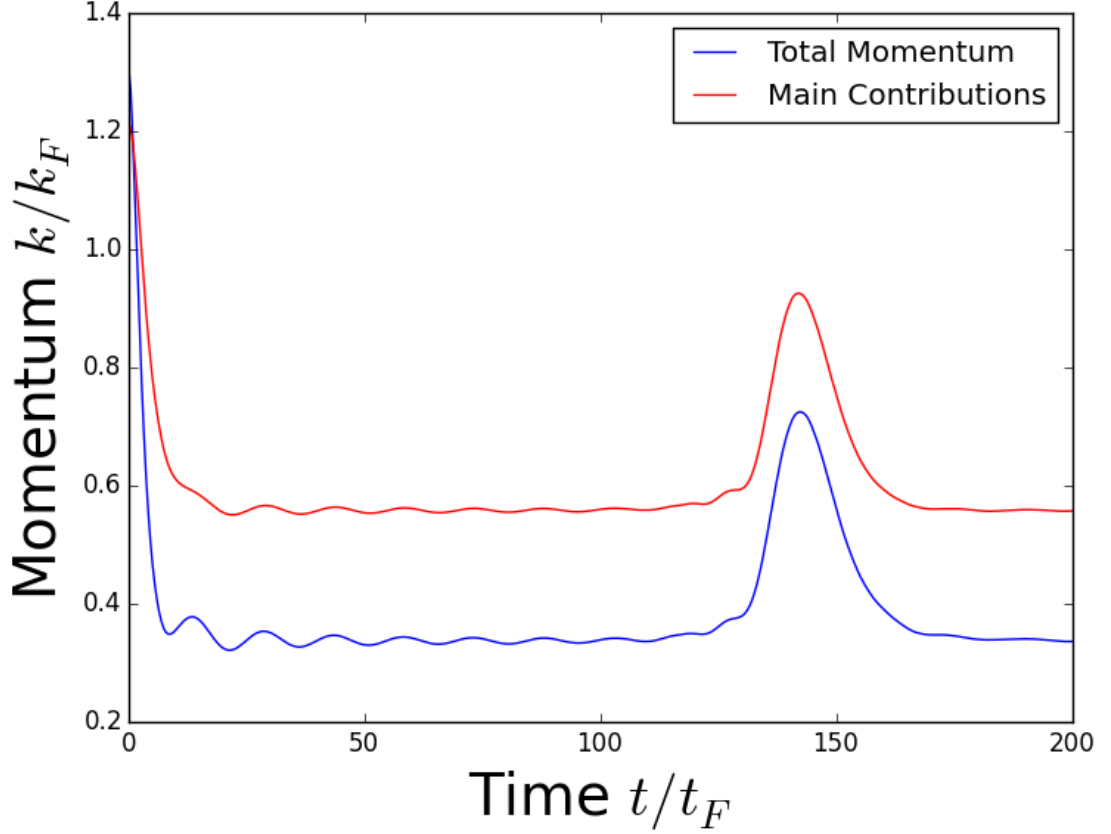


Figure 3.15: Comparison of $\langle P_{\downarrow}(t) \rangle$ to the sum over transitions between the two main state pair contributors identified. The inclusion of all transitions between states in the main branch matches the overall shape of the momentum evolution, while the inclusion of those transitions between states excited from the negative edge of the pseudo sea and those which share a pseudo particle with them, add flutter to the plot. The approximate flutter does not reproduce the same amplitude as the total, and the value of the momentum plateau is not matched, but the frequency of the revivals and flutter are accurately reproduced. In this graph, the total plot required calculating 400000000 state pairs, while the approximate value required calculating only 11865 state pairs, a computational speedup of about 4 orders of magnitude.

Chapter 4

Other Investigations

4.1 Thermalisation

The question of if and how a one-dimensional system thermalises from its initially excited state is interesting and open [115]. Experimental data has shown that such systems do not always relax into a thermalised state [14, 120], and theoretical work on the subject has shown there can be a non-thermal steady state that a system can relax into [115, 121–127], while other work has inspected the locality of this state and how looking at a wider scope affects conclusions [128, 129]. Within this area the effects of dimensionality and whether a system is closed or integrable seem to be strong [122, 123, 130–133]

Recently it has been argued [134] that in the thermodynamic limit, the expectation value of an operator \mathcal{O} which is local in space can be found using the projection of the ground state onto a single eigenstate of the system Φ_s (see Eqn (4.1)). Also that as $t \rightarrow \infty$ expectation values of observables in the system can be found from the expectation of that single state [134] as shown in Eqn (4.2)

$$\lim_{N \rightarrow \infty} \langle \mathcal{O}(t) \rangle = \lim_{N \rightarrow \infty} \left[\frac{\langle \Psi | \mathcal{O}(t) | \Phi_s \rangle}{2 \langle \Psi | \Phi_s \rangle} + \Phi_s \leftrightarrow \Psi \right] \quad (4.1)$$

$$\lim_{t \rightarrow \infty} \lim_{N \rightarrow \infty} \langle \mathcal{O}(t) \rangle = \lim_{N \rightarrow \infty} \frac{\langle \Phi_s | \mathcal{O} | \Phi_s \rangle}{\langle \Phi_s | \Phi_s \rangle}. \quad (4.2)$$

Here the item $\Phi_s \leftrightarrow \Psi$ denotes the previous term in the equation with terms Φ_s and Ψ swapped.

The current system, being integrable, one-dimensional, and evolving from an initial state far from equilibrium, is a good example of those that have been of such interest. Though Eqn (4.2) was derived under assumptions that don't hold in our system, we can make some numerical observations about whether it may hold for the momentum operator here, providing complementary information in a similar system. The first steps of such an analysis have been made, and our limited results are presented below.

While no claim has been made of the relative import of Φ_s one might guess that it is a state with a large contribution to the momentum of the impurity, so looking only at those states with a single pseudo excitation seems a reasonable starting point. Plotting $\langle \Phi_s | P_{\uparrow} | \Phi_s \rangle$ against $|\langle FS | f_Q \rangle|$ for each such eigenstate found in the system gives the graph shown in Fig 4.1. While there clearly are states whose momenta are near the two values for infinite time momentum we have (the plateau on our plots and the theoretical $\langle P_{\downarrow}(\infty) \rangle$), none have a particularly notable $|\langle FS | f_Q \rangle|$, and there is no obvious feature leading to some state we can take as an initial guess for Φ_s .

Though these plots don't provide any conclusive data on the thermalisation hypothesis, they do give some more information about the structure of the singly excited eigenstates. We can see the states in this subset are bounded in momentum, and those states where the impurity has a positive momentum (i.e. the impurity is travelling in the same direction as it was initially going) have a greater $|\langle FS | f_Q \rangle|^2$ on average than those where it is negative. This asymmetry can be seen in Figure 4.2, which shows a much stronger directionality than is obvious in Figure 4.1, Figure 4.2 shows the import of each range of momentum, plotting a histogram showing the value of the equation

$$\sigma = \sum_{f_Q} \langle f_Q | P_{\uparrow} | f_Q \rangle |\langle FS | f_Q \rangle|^2 \quad (4.3)$$

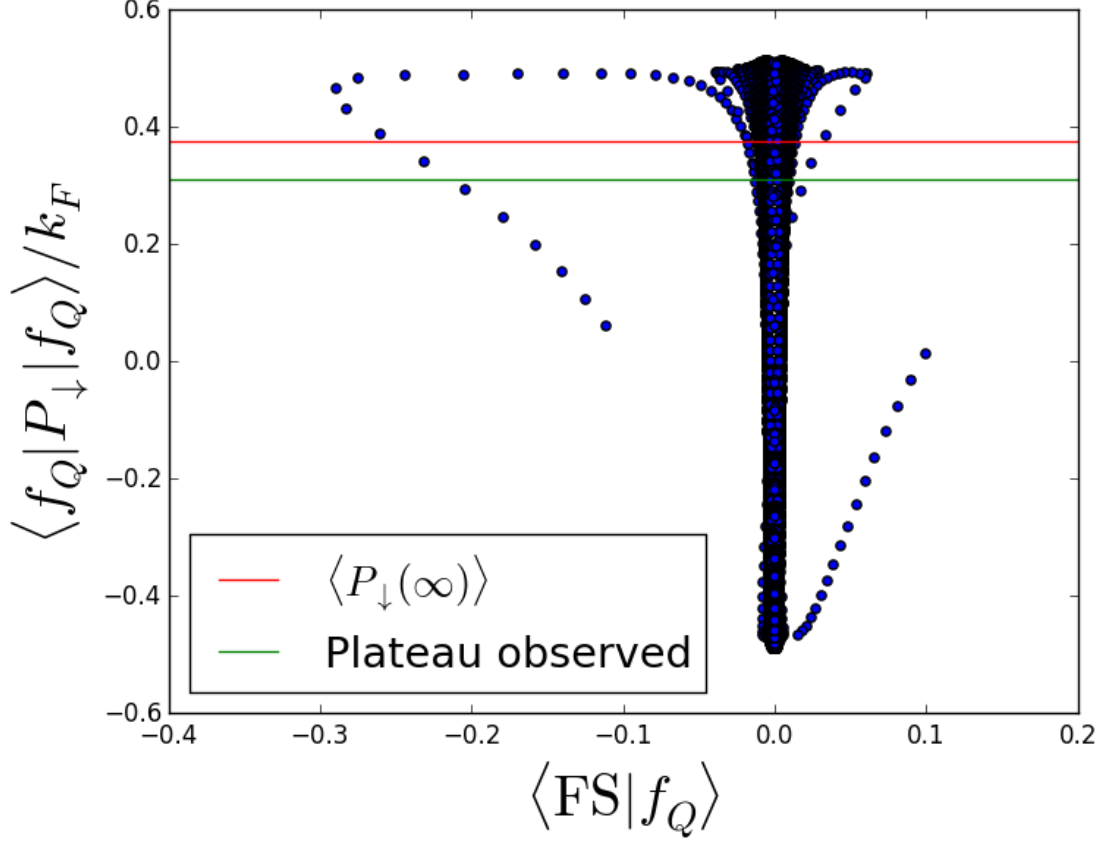


Figure 4.1: Distribution of each state’s momentum contribution, and the weight that contribution has. This plot is limited to states that are singly excited for clarity, as the structure in states with extra excitations can’t be seen at this scale. The red line shows the time-independent contribution of all states, and the green line denotes the plateau seen in the momentum. While there are states that have the momentum which would occur at infinite time (whichever of the two definitions we use), there is no obvious feature in the distribution around this point.

for each bucket, where the sum is over those $|f_Q\rangle$ whose momentum is within the bucket’s range. Not only does this figure show a very strong directionality, but it also demonstrates two separate progressions in σ : one that follows the contribution of the main branch, and another from all states in different branches of Fig 3.2.

While there is a much stronger positive contribution to the impurity’s momentum seen by accounting for the importance of each state there are actually more eigenstates where the impurity has a negative momentum than otherwise. We show this in Figure 4.3, which plots the number of states over the same buckets as used for Figure 4.2. It can be seen in this figure that while there are peaks in the number of states at both bounds in the momentum, the number of states near

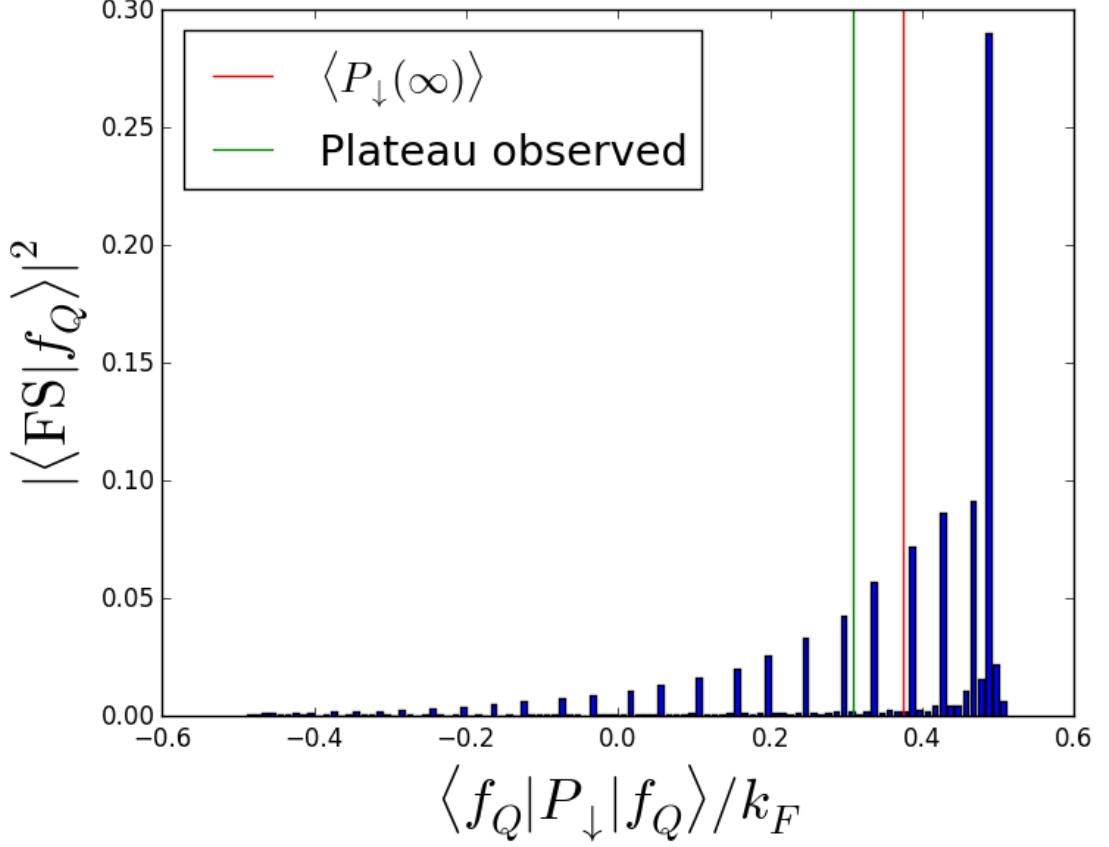


Figure 4.2: Contribution to infinite time momentum from singly excited states. Each bar is the sum of the $|\langle FS | f_Q \rangle|^2$ for the states in that region, the red vertical line denotes the infinite time contributions from all states, and the green line denotes the position of the plateau seen when the total momentum against time is plotted. While the contributions increase markedly near the upper bound on the momentum, the peak is slightly beforehand. There are two apparent contributions: one from the progression of the most important family, and one from others, but both have a peak at the same point.

the negative bound is much larger than at the positive one.

4.2 Asymptotic $\langle P_\downarrow(\infty) \rangle$

The discussion presented in section 3.4 on the representative nature of the contribution from the main parametric branch (seen in Fig 3.2) is necessarily restricted to the range of parameters our code can reach. Naturally, the question of whether this behaviour persists to the thermal regime of $N \rightarrow \infty$ has been raised. As the computational expense of calculating the full $\langle P_\downarrow(t) \rangle$ for a large system is prohibitively expensive for system sizes greater than $N \approx 99$, we looked at how repre-

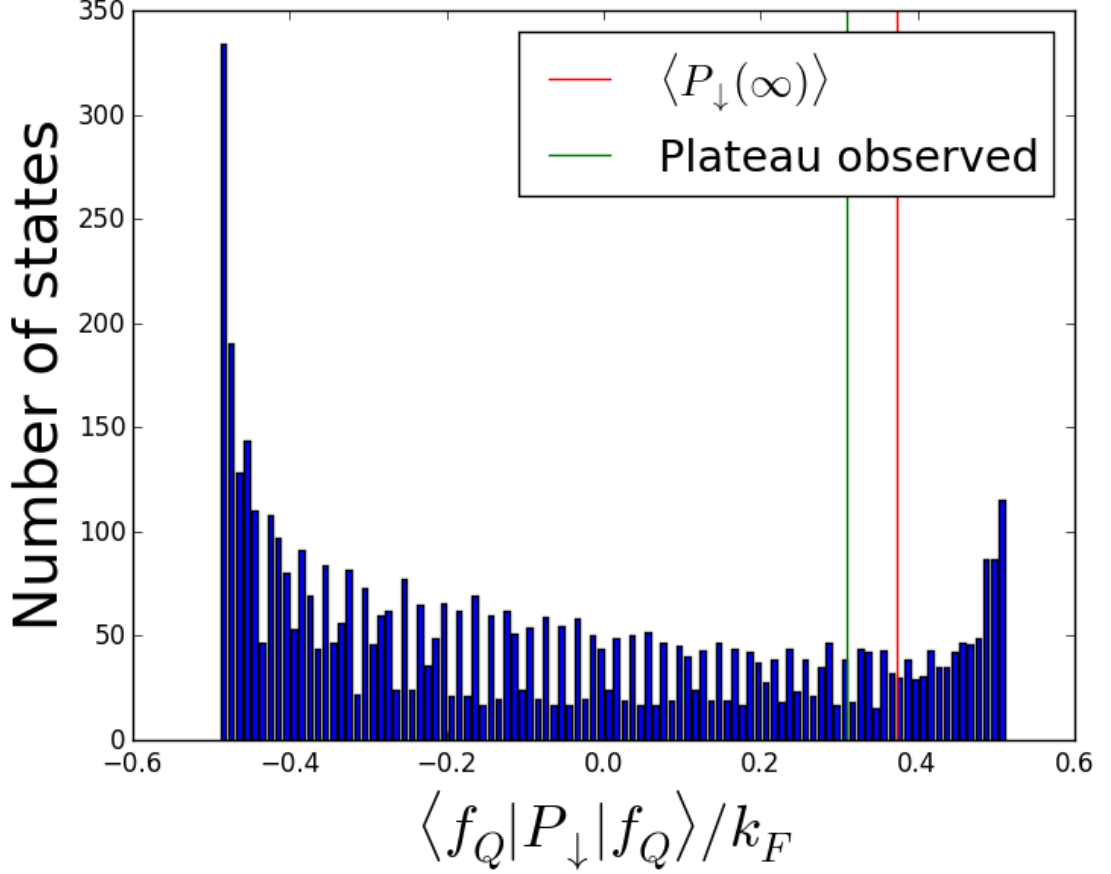


Figure 4.3: Distribution of the singly excited states across their expectation values of the impurity’s momentum. Each bar represents the number of states within that region of momentum, the red vertical line denotes the infinite time contributions, and the green line denotes the position of the plateau when the total momentum against time is plotted. The momentum of these states is bounded in both directions, and there are more states near these bounds than elsewhere. While the number of states with negative momentum is greater than those with positive momentum, the $|\langle FS | f_Q \rangle|^2$ weights mean the contribution from positive momentum states is much greater (see Fig 4.2).

sentative the infinite time contribution of the main branch $\langle P_\downarrow^1(\infty) \rangle$ is of the total value as the system grows larger. While the normalised values of the main branch seem to tend towards $\langle P_\downarrow(\infty) \rangle$ for the range of system sizes we can calculate the momentum evolution for, as we progress into larger systems, $\langle P_\downarrow^1(\infty) \rangle$ continues to decrease, as shown in Figure 4.4. An analytical approach made by Oleksandr Gamayun [135] has shown this is how they behave as the system moves into the thermal regime $N \rightarrow \infty$, with the contribution of the main branch continually decreasing, and eventually disappearing $\langle P_\downarrow^1(\infty) \rangle \rightarrow 0$.

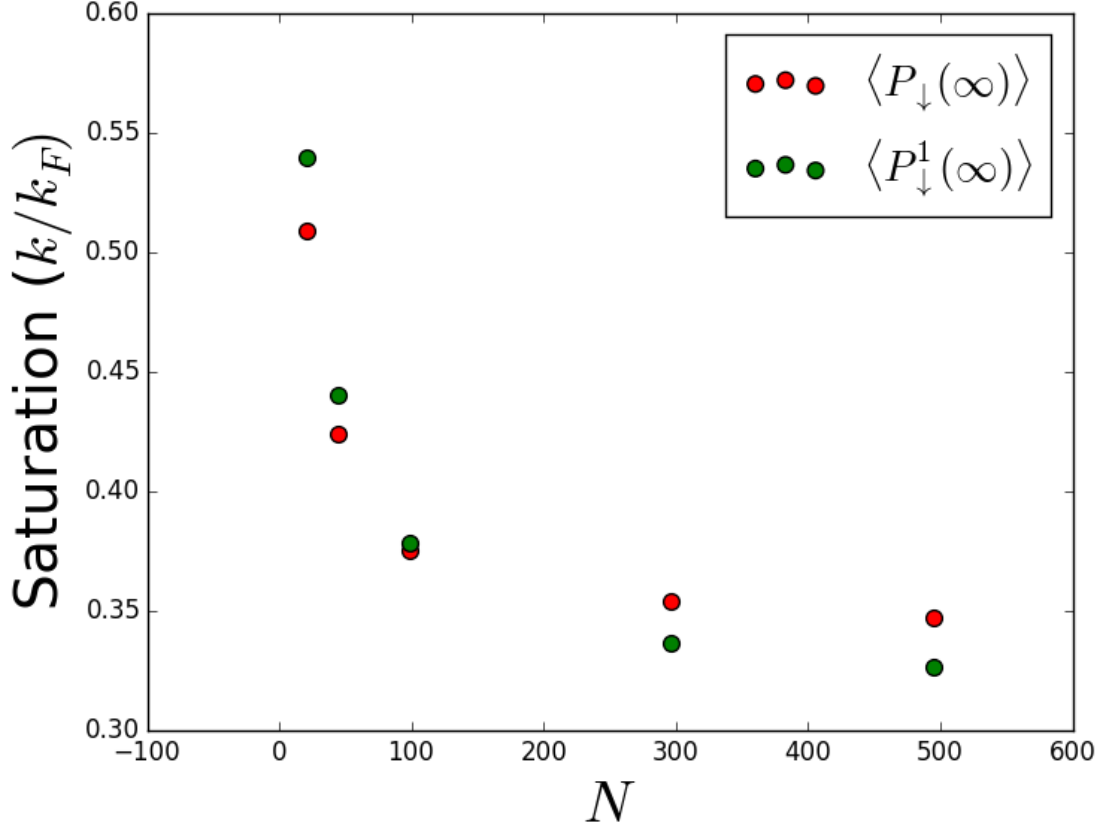


Figure 4.4: How the normalised time-independent contributions to the momentum from the main family compare with the total as the system size changes. For those systems which we can plot the time evolution of the momentum (with $N < 100$), the infinite time contributions of the main branch are almost representative of the total, and their representative nature increases with increasing system size. For larger systems, outside of this calculable range, the infinite time contribution of the main branch decreases further, away from the total. An analytical analysis shows that this progression continues, and as the system size diverges, the main branch's contribution tends to zero [135].

4.3 Conclusion

While we have no conclusive results on the thermalisation hypothesis in our system, the code we have should provide an adequate platform for research into the area. Initial plots show that if some representative eigenstate Φ_s exists, it does not have a standout value of $\langle FS|f_Q\rangle$, and the distribution of states does not show any standout feature near where it should be. The plots created in order to find Φ_s shed some light on the infinite time momentum of the impurity, while there are actually more states with a negative momentum, the impurity's directionality comes from the strong asymmetry in the contribution to ς .

The discovery in Section 3.4, that the main family is representative of the total momentum contribution without the flutter, should only be relevant to finite systems, as its infinite time contribution does not stay representative. As $N \rightarrow \infty$, then $P_1(\infty) \rightarrow 0$, but this progression is slow and can be discounted for the systems investigable by our program.

Chapter 5

Concluding Remarks

5.1 Results

To conclude, this work has discussed the momentum evolution of an impurity quenched into a one dimensional Tonks-Girardeau liquid. We find agreement with the statements made in reference [69] on the momentum evolution of the impurity, reproducing all progressions in the plateau and quantum flutter. Section 2.4 presented progressions in the momentum revivals that come from finite size effects, and show that for a large initial momentum they can be qualitatively described using a classical argument based on the momentum imparted to the background gas by the impurity. Though useful, this argument cannot be complete as it fails to describe the equivalency in the change to $\langle P_{\downarrow}(t) \rangle$ that comes from modifying γ via either the density of the background gas or the interaction strength between the background gas and the impurity. The relationship between the momentum plateau and the theoretical infinite time value obtained from time averaging $\langle P_{\downarrow}(\infty) \rangle$ was explored in Section 2.5, and it was shown that while the momentum plateau is constant with changing system size, $\langle P_{\downarrow}(\infty) \rangle$ starts out much higher and decreases towards the value of the plateau, the difference decreasing with a power law relation.

Chapter 3 described patterns observed in the eigenstates and eigenstate pair contributions to the momentum of the impurity, and used them to explain why

different features of the momentum evolution saturate at a different accuracy as measured by ς . We find that the overall shape of the evolution is determined by eigenstate transitions within the same branch of Figure 3.2, with those in the main branch contributing the most, though the contribution from this branch becomes less representative with large systems. These contributions can be normalised using Equation (2.1), to account for the difference in ς between subsets of states used and the total. This shows that the states in the main branch are representative of the total in setting the momentum plateau, but contribute more to the momentum revivals than their ς would suggest. The quantum flutter which is the main topic of references [69, 70] was shown to come from inter-branch transitions, which demonstrates that the contribution from those states with more than one pseudo excitation is negligible. While the entire flutter requires all inter-branch transitions, the frequency at about a quarter of the amplitude can be obtained from just looking at those transitions between states excited from the negative edge of the pseudo sea and those in other branches, under the condition that both states share a pseudo particle. This can provide an intuitive explanation for how the numerics describes the loss of flutter when the initial momentum drops below the Fermi momentum, as the structure of the Bethe Ansatz inhibit any states excited from the negative edge when $Q < k_F$.

These patterns can explain the stability of each feature once ς has passed a given point. Figure 3.2 shows that states from the main branch have a much greater contribution to ς than others, and hence are counted first. Similarly, states with more than one pseudo excitation are accounted for much later when stepping up ς . Because transitions between states in the main branch define the general shape of the momentum evolution, and more concretely, define the frequency of the momentum revivals, these features stabilise much earlier than the exact value of the momentum plateau and the flutter around it. The inter-branch transitions that define the frequency of the flutter require the lesser contributing branches to be accounted for, this naturally results in a greater value of ς before the feature

has been fully described. However as all eigenstates of the system contribute to the momentum plateau, that value shows no saturation at $\varsigma < 1$.

Finally, the distribution of the singly excited eigenstates in the momentum was shown in Chapter 4, demonstrating no significant pattern around the thermal value of the impurity's momentum. In the same chapter, the contribution to $\langle P_{\downarrow}(\infty) \rangle$ from the main branch of Figure 3.2 is shown to decrease relative to the total $\langle P_{\downarrow}(\infty) \rangle$ as the system size increases. While this doesn't necessarily mean the momentum plateau from the normalised main branch contribution decreases relative to the total plateau, it has been found elsewhere that this is the case [135], so the representative nature of the main families contribution to the momentum plateau found in Section 3.4 is only valid in finite systems.

5.2 Limitations and Further Work

The current work only directly applies to the integrable case in the Tonks-Girardeau regime, and much of the results are on the structure of the Bethe Ansatz solution to the system, without a known physical interpretation. Despite this limitation it is hoped that these results can allow others to probe this regime with much less computational expense, from which more physical results can be found. The ubiquitous nature of the Bethe Ansatz in integrable one-dimensional systems also lends credibility to a hope that such patterns may occur in different models, both on a lattice and in the continuum.

An alternate direction of further study might be into the case of an attractive potential between the impurity and background gas. While requiring changing the code which solves the Bethe Ansatz to account for complex Bethe roots [136] this route should not require changing the code which finds the impurity's momentum.

Overall we have presented novel research in this system, writing code and discovering relations that can aid any research of others in this area.

Appendices

Appendix A

Code Details

A.1 Introduction

As the central tool used throughout this thesis, the code written for calculating off-diagonal elements in the matrix of the background gas momentum operator deserves some discussion, and is provided here. While our method of finding eigenstates of our system is novel, it is beyond the scope of this thesis, being written by Evgeni Burovski and not the current author. Instead this chapter discusses the process of finding the time dependent momentum contributions from a given set of eigenstates. We will neglect the details of encoding those equations presented in Section 1.2.1 and discuss the challenges faced when scaling to large systems, how they have been circumvented and what trade-offs have been made. Hence this chapter contains no information on the physics or maths of the problem, focusing solely on the implementation details of this research.

There are two main discussions in this chapter, 1) How to efficiently spread the work required over multiple processes, and 2) the benefits and disadvantages of storing different data structures, though there is no clear separation between them, as different methods often make different compromises between these values.

Throughout this chapter we will refer to two stages, the *calculation stage* and the *analysis stage*, with the assumption that the majority of the calculation is done on a larger machine, such as a computing cluster, and the analysis done on a much

smaller personal computer. Note all judgement calls on when a data structure was too large, or took too much computation for the analysis stage, were made to account for a personal computer with 2GB of RAM and one hyperthreaded 2.20GHz processor. The most notable decision was whether calculating $\langle P_{\downarrow}(t) \rangle$ from the amplitudes and frequencies in the RHS of Eqn (1.19) should be part of the calculation stage or if it could be done during analysis.

In order to simplify the discussion, we shall compare and contrast the approaches to two different systems: one small system (e.g. $N = 15$) accounting for $N_s = 400$ states, and one large system (e.g. $N = 45$) accounting for $N_s = 20000$ states. To give the reader an idea of how the time required to find $\langle P_{\downarrow}(t) \rangle$ from the eigenstates of the system changes with increasing system size N a description of the calculation bottlenecks is required. The bottleneck in calculating each individual amplitude from a pair of states comes from the calculation of the singular value decomposition of an $N \times N$ matrix. This scales with N^3 , while the number of amplitudes that must be calculated in this manner scales with N_s^2 . The number of states N_s here has a non-trivial but strongly increasing relationship with N and this relationship is shown in Figure 2.2.

A.2 Data Structures

When working on a small system, worries about computational expense and memory usages are much lower than otherwise. Hence most design decisions were made based on the ease of analysis once all terms on the RHS of Eqn (1.19) have been found. The data required for the analysis made in this work are the amplitude, frequency, and pair of eigenstates for each term on the RHS of Eqn (1.19), along with the system parameters (both physical and non-physical) described in Chapter 2. Note however, that the form of a stored eigenstate changes throughout the process of reading from a stored cache, calculating amplitudes, and storing with amplitudes and frequencies for a given contribution. In order to save calculation, many values which must be calculated once for each eigenstate and used to find

the amplitude of each transition to or from that state are cached in the eigenstate structures during the calculation step. However, in analysis, the only identification required for a state are the pseudo excitations that create it (see Section 3.2). This section describes the form of data structures written to disk in the calculation step for use in analysis.

In a system near our “small” example, N_s is low enough that all these values can be simultaneously stored in RAM. Because of this ability, data structures for these systems are designed with the primary objective of being easy to read and manipulate during analysis, storing all values required in a single file, with no recalculation required (see Figure A.1a). From this data $\langle P_{\downarrow}(t) \rangle$ for any period of time is easily created, and any subsets can be found by filtering contributions by the relevant eigenstate pairs, providing good flexibility in analysis within reasonable time frames. For a larger system size, and the correspondingly larger number of states used, such an approach is no longer viable, as the calculation time of $\langle P_{\downarrow}(t) \rangle$ from the elements of the Fourier transform, and the space required to store all individual contributions both become prohibitively expensive. The consequences of these restrictions are twofold: first, the process of finding the total $\langle P_{\downarrow}(t) \rangle$ from all contributions must be moved into the calculation stage, and second, a method of only reading in those contributions required for a subset analysis must be implemented.

Implementing the first of these restrictions is a simple manner, simply choosing a range of time values to plot before calculation, and saving the momentum and time values for each of the points requested, on disk for analysis. Moving the calculation of $\langle P_{\downarrow}(t) \rangle$ from the analysis step to the calculation one is not as much of a hindrance as one might initially suppose as the calculation of the total $\langle P_{\downarrow}(t) \rangle$ is rarely done more than once.

The latter of these two consequences is implemented by storing the amplitudes on disk in a dense two dimensional array, with each row and column corresponding to the eigenstates which create the amplitude. As this matrix is made in

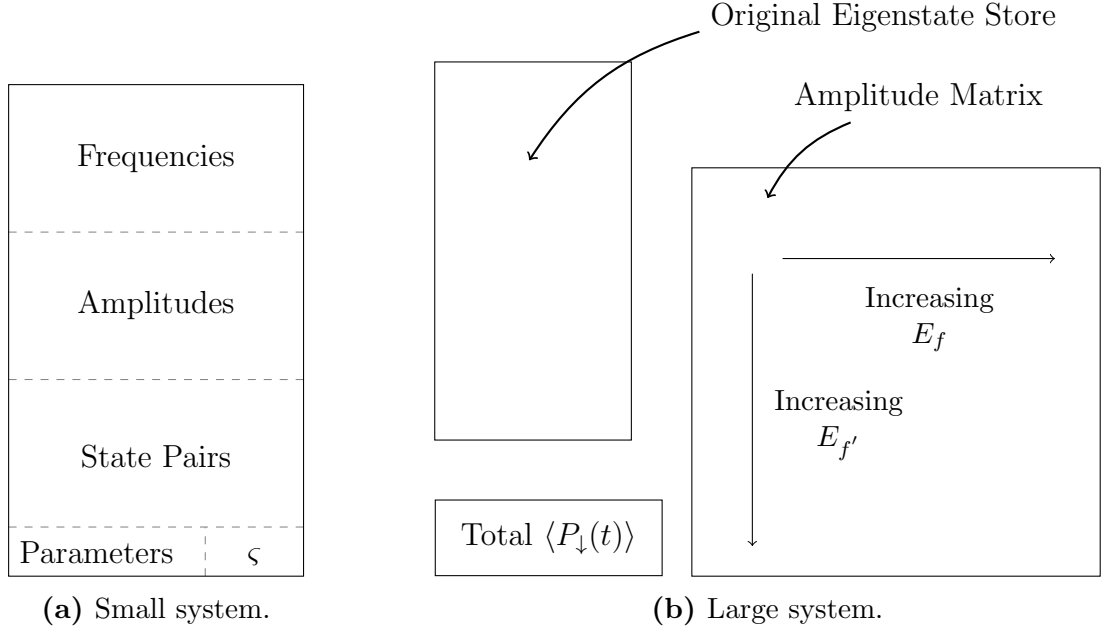


Figure A.1: Schematics of data structures serialised for both large and small systems. For small systems a hash table containing all data required for analysis was directly serialised to disk and unserialised when required. This had the advantage of simplicity, and would not easily result in un-synchronised data, as the calculation stage created the data in one step, and no modifications are needed in the analysis stage. Frequencies, amplitudes, and eigenstate pairs are kept ordered by increasing energy, and can hence be matched accordingly, this means only information required for choosing interesting states is needed in the state pairs. When the system is large, storing all data in RAM at the same time in the analysis stage is impossible, so a different method of reading in data was devised (see Figure A.2). Said method centred around calculating the position in the stored amplitude matrix where each interesting eigenstate pair will be, and only reading the data stored in those positions. As this new method of reading those amplitudes required for partial contributions took time and required the calculation of each eigenstates' energies, storing the frequencies associated with each amplitude became redundant, and was removed for storage space concerns.

order, with the eigenstate energy for each column/row increasing with increasing element index, the amplitude for a given pair of eigenstates can be obtained by calculating the corresponding position in the array and only reading the value in that position. A decision to forgo storing the frequencies of each state pair was made, as the recalculation of this value is trivial, and faster than reading a value from disk, especially after the energies for each eigenstate have been found when finding corresponding positions in the amplitude matrix. We also decided to keep checkpoint files for eigenstates and amplitudes separate, rather than joining them together. This helped in parsing the data structures, reusing existing code to read eigenstates from their original structure, but created a danger which the user must be aware of. The two files may get out of sync if eigenstates are added to the cache which would have been accounted for in the matrix of amplitudes. Keeping these two sets of values separate also meant that spreading the work of calculating amplitudes across multiple processors could be kept simple, memory mapping our matrix onto a file as will be described in Section A.3. The data structures saved to disk when in this large system regime, and hence those that define the majority of our codes structure, are shown in Figure A.1b. These consist of a packed two-dimensional array of amplitudes, ordered by the energy of each state in the transition, an SQLite database storing the eigenstates of the system (in the same format as delivered by the eigenstate calculation), and a numpy named array containing the impurity’s momentum and time over a predefined time period.

A.3 Multiple Processors

With a large system, the need to spread work over more processors becomes much greater, as the amount of computation increases dramatically (the manner in which it increases is discussed at the start of this Chapter). Luckily, the form of the equations solved means the bottleneck in the computation can be written in an embarrassingly parallel manner. Each process takes a different set of eigenstate pairs to work with, and works independently to find the background gas’ momen-

tum contribution from that set of transitions. They then sum these contributions with the other processes before subtracting the total from the total momentum to obtain the momentum of the impurity. This method, schematically shown in Figure A.2, lends itself very well to the packed data structure of amplitudes we store on disk (see Section A.2). Each process can memory map a chunk of the

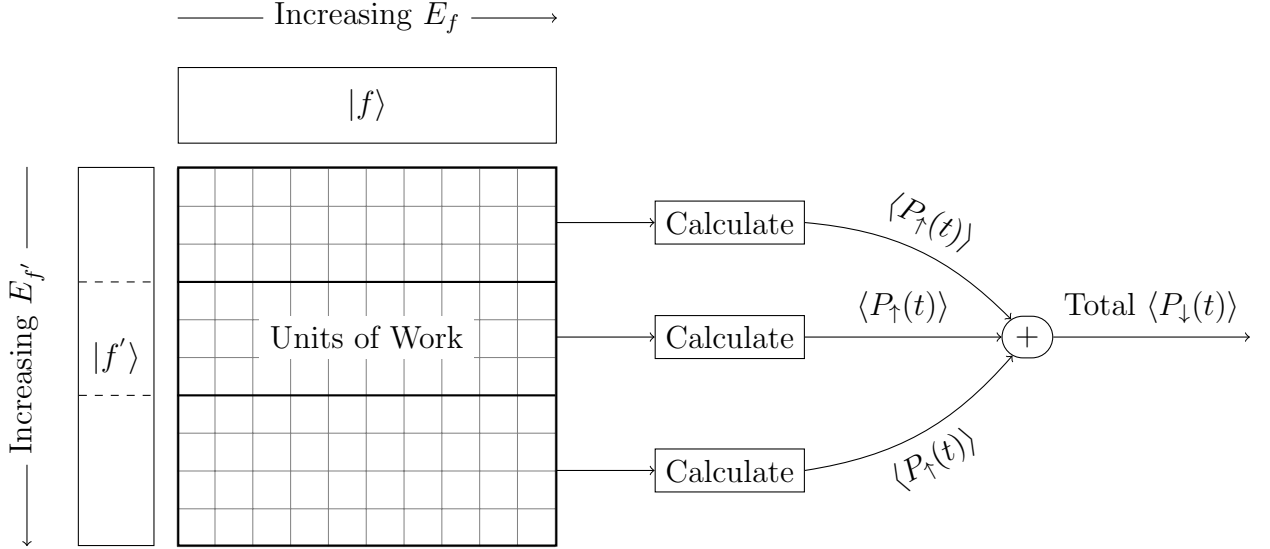


Figure A.2: Schematic of how work is spread over multiple processors, in this example 3 processors are used. The distribution of work across multiple processors is done in a simple manner; each processor takes a block of the amplitude matrix and calculates the contribution to the RHS of Equation (1.19) for a set of time points. Each of these contributions is then summed, and taken from the total momentum of the system Q to find the momentum of the impurity over the range in time calculated over.

file as its assigned part of the matrix, and when this chunk has been flushed to disk the amplitudes are saved in their assigned positions. Assigning the work in this manner means the number of processes used when the amplitude matrix was initially created is completely opaque to the user, keeping the data structures general, and allowing a user to reuse the amplitude matrix over a different number of processes without manual intervention.

The lower level spreading of processes has been implemented in two different ways, one uses the built in Python multiprocessing module, and the other uses mpi4py [137]. Dual implementations are maintained as the default multiprocessing module in Python can not spread load over more than one node in a cluster, but

we see less of an overhead when using it to manage different processes on a single node.

We observe a near-linear scaling from 1 to 64 processes used, calculating $\langle P_{\downarrow}(t) \rangle$ for 1000 points in time of our large system, greater numbers of processes have not been investigated as the wait for job scheduling becomes a limiting factor.

A.4 Improvements

While the current formulation of this code has been proved useful and reliable when working through this project, there are a few improvements which should have noticeable benefits, yet have not been made due to time constraints. The simplest of these is to save the packed matrix of amplitudes ordered by eigenstate overlap $|\langle FS|f_Q \rangle|^2$ rather than energy. This different ordering would help when inspecting how the system changes with differing ς saturation. When a set of amplitudes has been calculated for a saturation of e.g. $\varsigma = 0.999$, the higher overlap eigenstates from this set that provide a saturation of $\varsigma = 0.9$ could be read from the original data file in the simple manner shown in Figure A.3. Currently, calculating the contribution from a smaller set requires saving another matrix of amplitudes in a separate file that simply contains a subset of the information in the original: this results in needless duplication. Storing the amplitude matrix ordered by energy has no inherent benefit, but the amount of programmatic complexity in order to realise the benefits of an alternate order has so far delayed this change.

Another possible yet unimplemented feature is the filtering of eigenstate pairs in the initial computational run. The trade-off on using this hypothetical feature would be sacrificing future flexibility in analysis for a shorter initial computational run. Thus certain contributions would not be calculated initially on the assumption that they will never be needed in the analysis stage. While the results presented in Chapter 3 suggest that such restrictions can be made when looking at specific features of the momentum evolution, the focus of this work never moved to using these statements, and this feature was hence not implemented.

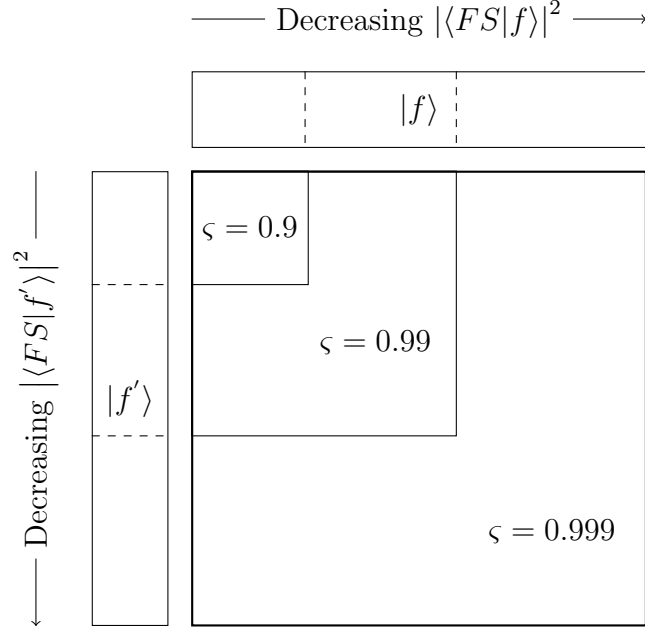


Figure A.3: Alternate order of amplitude matrix. Currently amplitudes of contributions are stored ordered by the energy of the eigenstates in each transition shown in Figure A.2. If the matrix were ordered by $|\langle FS|f\rangle|^2$ instead, then finding the amplitudes for a smaller subset of eigenstates, taken in this order, would be much simpler. This would mean finding the contribution from a smaller set of eigenstates could be done without recalculation of their amplitudes.

One final compromise which a future researcher may wish to reverse has been made to sacrifice close to a factor of 2 in program speed for code simplicity. As the amplitude matrix is symmetric, the direction of transition not affecting the value, there is no reason to find every possible transition as is currently done. Finding the amplitudes of all off-diagonal transitions in a given order and doubling the contribution would decrease both the required RAM and CPU time dramatically. An equivalent optimisation is already implemented in the code for subset analysis, but it is not accounted for when calculating the total amplitudes. The decision has been done solely for the sake of code clarity and speed of development, and as such is a strong candidate for change in the future. Furthermore, in obtaining this factor of 2 speedup, it is highly likely that a quirk in implementation can be removed, reducing the RAM required by yet another factor of 3. The details of this are discussed in the code comments and are based around the use of the `numpy.frompyfunc` command.

Overall the structure of the current program makes what the author believes to be reasonable compromises between flexibility of analysis and computational resources, scaling well with multiple processors yet still allowing for easy selection of transition subsets by the researcher during analysis. There are some obvious possible improvements which the author sincerely hopes are made, and anyone wishing to use this code is encouraged to contact the author with any questions.

Bibliography

- [1] A. Lenard. “Momentum Distribution in the Ground State of the One-Dimensional System of Impenetrable Bosons”. *J. Math. Phys.* 5.7 (1964), pp. 930–943.
- [2] F. Calogero. “Solution of the one-dimensional N-body problems with quadratic and/or inversely quadratic pair potentials”. *J. Math. Phys.* 12.1971 (1971), pp. 419–436.
- [3] R. Scheunemann, F. S. Cataliotti, T. W. Hänsch, and M. Weitz. “Resolving and addressing atoms in individual sites of a CO₂-laser optical lattice”. *Phys. Rev. A* 62.5 (2000), p. 051801.
- [4] O. Morsch, J. H. Müller, M. Cristiani, D. Ciampini, and E. Arimondo. “Bloch oscillations and mean-field effects of Bose-Einstein condensates in 1D optical lattices”. *Phys. Rev. Lett.* 87.14 (2001), p. 140402.
- [5] H. Moritz, T. Stöferle, M. Köhl, and T. Esslinger. “Exciting Collective Oscillations in a Trapped 1D Gas”. *Phys. Rev. Lett.* 91.25 (2003), p. 250402.
- [6] L. Fallani, L. De Sarlo, J. E. Lye, M. Modugno, R. Saers, et al. “Observation of dynamical instability for a Bose-Einstein condensate in a moving 1D optical lattice”. *Phys. Rev. Lett.* 93.14 (2004), p. 140406.
- [7] B. L. Tolra, K. M. O’Hara, J. H. Huckans, W. D. Phillips, S. L. Rolston, et al. “Observation of reduced three-body recombination in a correlated 1D degenerate bose gas”. *Phys. Rev. Lett.* 92.19 (2004), p. 190401.

- [8] B. Paredes, A. Widera, V. Murg, O. Mandel, S. Fölling, et al. “Tonks-Girardeau gas of ultracold atoms in an optical lattice”. *Nature* 429.6989 (2004), pp. 277–281.
- [9] T. Stöferle, H. Moritz, C. Schori, M. Köhl, and T. Esslinger. “Transition from a strongly interacting 1D superfluid to a Mott insulator”. *Phys. Rev. Lett.* 92.13 (2004), p. 130403.
- [10] T. Kinoshita, T. Wenger, and D. S. Weiss. “Observation of a one-dimensional Tonks-Girardeau gas.” *Science* 305.5687 (2004), pp. 1125–1128.
- [11] M. Köhl, T. Stöferle, H. Moritz, C. Schori, and T. Esslinger. “1D Bose gases in an optical lattice”. 2014. arXiv:0406397v2 [cond-mat].
- [12] T. Kinoshita, T. Wenger, and D. S. Weiss. “Local pair correlations in one-dimensional Bose Gases”. *Phys. Rev. Lett.* 95.19 (2005), p. 190406.
- [13] C. D. Fertig, K. M. O’Hara, J. H. Huckans, S. L. Rolston, W. D. Phillips, et al. “Strongly inhibited transport of a degenerate 1D bose gas in a lattice”. *Phys. Rev. Lett.* 94.12 (2005), p. 120403.
- [14] T. Kinoshita, T. Wenger, and D. S. Weiss. “A quantum Newton’s cradle.” *Nature* 440.7086 (2006), pp. 900–903.
- [15] C. Ryu, M. F. Andersen, P. Cladé, V. Natarajan, K. Helmerson, et al. “Observation of persistent flow of a Bose-Einstein condensate in a toroidal trap”. *Phys. Rev. Lett.* 99.26 (2007), p. 260401.
- [16] S. Hofferberth, I. Lesanovsky, B Fischer, T Schumm, and J. Schmiedmayer. “Non-equilibrium coherence dynamics in one-dimensional Bose gases.” *Nature* 449.7160 (2007), pp. 324–327.
- [17] S. E. Olson, M. L. Terraciano, M. Bashkansky, and F. K. Fatemi. “Cold-atom confinement in an all-optical dark ring trap”. *Phys. Rev. A* 76.6 (2007), p. 061404.

- [18] a. H. Van Amerongen, J. J. P. Van Es, P. Wicke, K. V. Kheruntsyan, and N. J. Van Druten. “Yang-Yang thermodynamics on an atom chip”. *Phys. Rev. Lett.* 100.9 (2008), p. 090402.
- [19] X. Du, L. Luo, B. Clancy, and J. E. Thomas. “Observation of anomalous spin segregation in a trapped fermi gas”. *Phys. Rev. Lett.* 101.15 (2008), p. 150401.
- [20] S. Palzer, C. Zipkes, C. Sias, and M. Köhl. “Quantum Transport through a Tonks-Girardeau Gas”. *Phys. Rev. Lett.* 103.15 (2009), p. 150601.
- [21] E. Haller, M. Gustavsson, M. J. Mark, J. G. Danzl, R. Hart, et al. “Realization of an excited, strongly correlated quantum gas phase.” *Science* 325.5945 (2009), pp. 1224–1127.
- [22] D. Chen, M. White, C. Borries, and B. DeMarco. “Quantum Quench of an Atomic Mott Insulator”. *Phys. Rev. Lett.* 106.23 (2011), p. 235304.
- [23] S. Whitlock, P. Wicke, and N. J. Van Druten. “Controlling spin motion and interactions in a one-dimensional Bose gas” (2011). arXiv:1010.4545 [cond-mat.quant-gas].
- [24] S. Trotzky, Y.-A. Chen, A. Flesch, I. P. McCulloch, U. Schollwöck, et al. “Probing the relaxation towards equilibrium in an isolated strongly correlated 1D Bose gas”. *Nat. Phys.* 8.4 (2011), pp. 325–330.
- [25] J. Catani, G. Lamporesi, D. Naik, and M. Gring. “Quantum dynamics of impurities in a one-dimensional Bose gas”. *Phys. Rev. A* 85.2 (2012), p. 023623.
- [26] T. Fukuhara, A. Kantian, and M. Endres. “Quantum dynamics of a mobile spin impurity”. *Nat. Phys.* 9.4 (2013), pp. 235–241.
- [27] F. Meinert, M. J. Mark, E. Kirilov, K. Lauber, P. Weinmann, et al. “Quantum Quench in an Atomic One-Dimensional Ising Chain”. *Phys. Rev. Lett.* 111.5 (2013), p. 053003.

- [28] S. Tomonaga. “Remarks on Bloch’s Method of Sound Waves applied to Many-Fermion Problems”. 5.4 (1950), pp. 544–569.
- [29] J. M. Luttinger. “An Exactly Soluble Model of a Many-Fermion System”. *J. Math. Phys.* 4.9 (1963), pp. 1154–1162.
- [30] D. C. Mattis and E. H. Lieb. “Exact Solution of a ManyFermion System and Its Associated Boson Field”. *J. Math. Phys.* 6.2 (1965), pp. 304–312.
- [31] F. Calogero. “Solution of a Three-Body Problem in One Dimension”. *J. Math. Phys.* 10.12 (1969), pp. 2191–2196.
- [32] B. Sutherland. “Quantum Many-Body Problem in One Dimension: Ground State”. *J. Math. Phys.* 12.2 (1971), pp. 246–250.
- [33] E. H. Lieb and W. Liniger. “Exact Analysis of an Interacting Bose Gas. I. The General Solution and the Ground State”. *Phys. Rev. Lett.* 130.2 (1963), pp. 1605–1616.
- [34] E. H. Lieb. “Exact analysis of an interacting bose gas. II. the excitation spectrum”. *Phys. Rev.* 130.4 (1963), pp. 1616–1624.
- [35] C. N. Yang and C. P. Yang. “Thermodynamics of a One-Dimensional System of Bosons with Repulsive Delta-Function Interaction”. *J. Math. Phys.* 10.1969 (1969), pp. 1115–1122.
- [36] C. N. Yang. “Some exact results for the many-body problem in one dimension with repulsive delta-function interaction”. *Phys. Rev. Lett.* 19.23 (1967), pp. 1312–1315.
- [37] B. Sutherland. “Further results for the many-body problem in one dimension”. *Phys. Rev. Lett.* 20.3 (1968), pp. 98–100.
- [38] E. H. Lieb and F. Wu. “Absence of Mott transition in an exact solution of the short-range, one-band model in one dimension”. *Phys. Rev. Lett.* 20.25 (1968), pp. 1445–1448.

- [39] F. D. M. Haldane. “‘Luttinger liquid theory’ of one-dimensional quantum fluids. I. Properties of the Luttinger model and their extension to the general 1D interacting spinless Fermi gas”. *J. Phys. C Solid State Phys.* 14 (1981), pp. 2585–2609.
- [40] A. O. Gogolin, A. A. Nersesyan, and A. M Tsvelik. *Bosonization and Strongly Correlated Systems*. Cambridge University Press, 1999.
- [41] T. Giamarchi. *Quantum Physics in One Dimension*. Oxford University Press, 2003.
- [42] M. A. Cazalilla, R. Citro, T. Giamarchi, E. Orignac, and M. Rigol. “One dimensional bosons: From condensed matter systems to ultracold gases”. *Rev. Mod. Phys.* 83.December (2011), pp. 1405–1466.
- [43] M. Pustilnik, M. Khodas, A. Kamenev, and L. I. Glazman. “Dynamic response of one-dimensional interacting fermions”. *Phys. Rev. Lett.* 96.19 (2006), p. 196405.
- [44] G. a. Fiete. “Colloquium: The spin-incoherent Luttinger liquid”. *Rev. Mod. Phys.* 79.3 (2007), pp. 801–820.
- [45] M. B. Zvonarev, V. V. Cheianov, and T. Giamarchi. “Spin Dynamics in a One-Dimensional Ferromagnetic Bose Gas”. *Phys. Rev. Lett.* 99.24 (2007), p. 240404.
- [46] A. Imambekov and L. I. Glazman. “Exact Exponents of Edge Singularities in Dynamic Correlation Functions of 1D Bose Gas”. *Phys. Rev. Lett.* 100.20 (2008), p. 206805.
- [47] A. Imambekov and L. I. Glazman. “Universal theory of nonlinear Luttinger liquids.” *Science* 323.5911 (2009), pp. 228–231.
- [48] A. Imambekov, T. L. Schmidt, and L. I. Glazman. “One-dimensional quantum liquids: Beyond the Luttinger liquid paradigm”. *Rev. Mod. Phys.* 84.3 (2012), pp. 1253–1306.

- [49] H. Bethe. “On the Theory of Metals . I. Eigenvalues and eigenfunctions of a linear chain of atoms.” *Z. Phys.* 71.1931 (1931), pp. 205–226.
- [50] M. Gaudin. *La fonction d’onde de Bethe*. Masson, Paris, 1983.
- [51] A. H. C. Neto and M. P. A. Fisher. “Dynamics of a heavy particle in a Luttinger liquid”. 53.15 (1995), pp. 9713–9718. arXiv:9510094 [cond-mat].
- [52] H. Castella. “Effect of Finite Impurity Mass on the Anderson Orthogonality Catastrophe in One Dimension”. *Phys. Rev. B* 54.24 (1996), pp. 17422–17430.
- [53] A. Lamacraft. “Dispersion relation and spectral function of an impurity in a one-dimensional quantum liquid”. *Phys. Rev. B* 79.24 (2009), p. 241105.
- [54] M. D. Girardeau and A. Minguzzi. “Motion of an impurity particle in an ultracold quasi-one-dimensional gas of hard-core bosons.” *Phys. Rev. A* 82.3 (2009), p. 033610. arXiv:1003.0652.
- [55] M. Punk, P. T. Dumitrescu, and W. Zwerger. “Polaron-to-molecule transition in a strongly imbalanced Fermi gas”. *Phys. Rev. A* 80.5 (2009), p. 053605.
- [56] S. Giraud and R. Combescot. “Highly polarized Fermi gases: One-dimensional case”. *Phys. Rev. A* 79.4 (2009), p. 043615.
- [57] S. Giraud and R. Combescot. “Comment on ”motion of an impurity particle in an ultracold quasi-one-dimensional gas of hard-core bosons”” (2010), pp. 2–4. arXiv:1003.0652.
- [58] J. Goold, H. Doerk, Z. Idziaszek, T. Calarco, and T. Busch. “Ion-induced density bubble in a strongly correlated one-dimensional gas”. *Phys. Rev. A* 81.4 (2010), p. 041601.
- [59] M. Ovchinnikov and A. Novikov. “Microscopic computational model of a superfluid”. *J. Chem. Phys.* 132.21 (2010), p. 214101.

- [60] T. Johnson, S. Clark, M. Bruderer, and D. Jaksch. “Impurity transport through a strongly interacting bosonic quantum gas”. *Phys. Rev. A* 84.2 (2011), p. 023617.
- [61] N. Spethmann, F. Kindermann, S. John, C. Weber, D. Meschede, et al. “Dynamics of Single Neutral Impurity Atoms Immersed in an Ultracold Gas”. *Phys. Rev. Lett.* 109.23 (2012), p. 235301.
- [62] C. Recher and H. Kohler. “From Hardcore Bosons to Free Fermions with Painlevé V”. *J. Stat. Phys.* 147.3 (2012), pp. 542–564.
- [63] P. Windpassinger. “Quantum transport: Spins on the move”. *Nat. Phys.* 9.4 (2013), pp. 209–210.
- [64] G. Astrakharchik and I. Brouzos. “Trapped one-dimensional ideal Fermi gas with a single impurity”. *Phys. Rev. A* 88 (2013), p. 021602.
- [65] F. Massel, A. Kantian, a. J. Daley, T. Giamarchi, and P. Törmä. “Dynamics of an impurity in a one-dimensional lattice”. *New J. Phys.* 15 (2013), p. 045018.
- [66] E. V. H. Doggen and J. J. Kinnunen. “Energy and contact of the one-dimensional fermi polaron at zero and finite temperature”. *Phys. Rev. Lett.* 111.2 (2013), p. 025302.
- [67] E. V. H. Doggen, A. Korolyuk, P. Törmä, and J. J. Kinnunen. “One-dimensional Fermi polaron in a combined harmonic and periodic potential”. *Phys. Rev. A* 89.5 (2014), p. 053621.
- [68] P. Massignan, M. Zaccanti, and G. M. Bruun. “Polarons, dressed molecules and itinerant ferromagnetism in ultracold Fermi gases.” *Rep. Prog. Phys.* 77.3 (2014), p. 034401.
- [69] C. J. M. Mathy, M. B. Zvonarev, and E. Demler. “Quantum flutter of supersonic particles in one-dimensional quantum liquids”. *Nat. Phys.* 8.12 (2012), pp. 881–886.

- [70] M. Knap, C. J. M. Mathy, M. Ganahl, M. B. Zvonarev, and E. Demler. “Quantum Flutter: Signatures and Robustness”. *Phys. Rev. Lett.* 112.1 (2014), p. 015302.
- [71] M. Gaudin. “Un System a Une Dimension de Fermions en Interaction”. *Phys. Lett. A* 24.1 (1967), pp. 55–56.
- [72] X. W. Guan, M. T. Batchelor, and C. Lee. “Fermi gases in one dimension: From Bethe ansatz to experiments”. *Rev. Mod. Phys.* 85.4 (2013), pp. 1633–1691.
- [73] J. B. McGuire. “Study of Exactly Soluble One-Dimensional N-Body Problems”. *J. Math. Phys.* 5.5 (1964), pp. 622–636.
- [74] J. B. McGuire. “Dynamics of interacting fermions in one dimension.” *Phys. Rev. A* 41.2 (1990), pp. 739–753.
- [75] D. M. Edwards. “Magnetism in Single-Band Models”. *Prog. Theor. Phys. Suppl.* 101 (1990), pp. 453–461.
- [76] H. Castella and X. Zotos. “Exact calculation of spectral properties of a particle interacting with a one-dimensional fermionic system”. *Phys. Rev. B* 47.24 (1993), pp. 16186–16193.
- [77] O. Gamayun, A. G. Pronko, and M. B. Zvonarev. “Impurity Green’s function of a one-dimensional Fermi gas”. *Nucl. Phys. B* 892 (2015), pp. 83–104.
- [78] M. D. Girardeau. “Relationship between Systems of Impenetrable Bosons and Fermions in One Dimension”. *J. Math. Phys.* 1.6 (1960), pp. 516–523.
- [79] C. J. M. Mathy, M. B. Zvonarev, and E. Demler. “Supplementary Material of Mathy2012”. *Nat. Phys.* 8 (2012), pp. 881–886.
- [80] J. B. McGuire. “Interacting Fermions in One Dimension. I. Repulsive Potential”. *J. Math. Phys.* 6.3 (1965), pp. 432–439.

- [81] B. Sutherland. *Beautiful Models*. World Scientific Publishing Co. Pte. Ltd., 2004.
- [82] M. T. Batchelor. “The Bethe ansatz after 75 years” (2007).
- [83] M. Flicker and E. H. Lieb. “Delta-Function Fermi Gas with Two-Spin Deviates.” *Phys. Rev.* 161.1962 (1967), pp. 179–188.
- [84] L. A. Takhtadzhan and L. D. Faddeev. “The Quantum Method of the Inverse Problem and the Heisenberg XYZ Model.” *Russ. Math. Surv.* 34.5 (1979), pp. 10–68.
- [85] E. K. Sklyanin. “Quantum Inverse Scattering Method. Selected Topics”. October (1991), pp. 63–97. arXiv:9211111v1 [arXiv:hep-th].
- [86] V. E. Korepin, N. M. Bogoliubov, and A. G. Izergin. *Quantum Inverse Scattering Method and Correlation Functions*. Cambridge University Press, 1993.
- [87] L. D. Faddeev. “How Algebraic Bethe Ansatz works for integrable model.” (1996). arXiv:9605187v1 [arXiv:hep-th].
- [88] S Belliard and E Ragoucy. “The nested Bethe ansatz for ‘all’ closed spin chains”. *J. Phys. A Math. Theor.* 41 (2008), p. 295202.
- [89] F. Franchini. “Notes on Bethe Ansatz Techniques” (2011). arXiv:9605187v1 [arXiv:hep-th].
- [90] E. Burovski. <https://bitbucket.org/burovski/mcba>.
- [91] M. Malcomson. <https://bitbucket.org/mmalcomson/mcba>.
- [92] P. S. Foundation. <https://www.python.org/>.
- [93] <http://www.scipy.org>.
- [94] <http://www.numpy.org>.
- [95] E. Burovski, V. V. Cheianov, O. Gamayun, and O. Lychkovskiy. “Momentum relaxation of a mobile impurity in a one-dimensional quantum gas”. *Phys. Rev. A* 89.4 (2014), p. 041601.

- [96] H. P. Büchler, V. B. Geshkenbein, and G. Blatter. “Superfluidity versus Bloch oscillations in confined atomic gases.” *Phys. Rev. Lett.* 87.10 (2001), p. 100403. arXiv:cond.
- [97] A. G. Sykes, M. J. Davis, and D. C. Roberts. “Drag force on an impurity below the superfluid critical velocity in a quasi-one-dimensional Bose-Einstein condensate”. *Phys. Rev. Lett.* 103.8 (2009), p. 085302.
- [98] A. Y. Cherny, J.-S. Caux, and J. Brand. “Theory of superfluidity and drag force in the one-dimensional Bose gas”. *Front. Phys.* 7.1 (2012), pp. 54–71.
- [99] G. Astrakharchik and L. P. Pitaevskii. “Motion of a heavy impurity through a Bose-Einstein condensate”. *Phys. Rev. A* 70.1 (2004), p. 013608.
- [100] J. Brand and A. Y. Cherny. “Dynamic structure factor of the one-dimensional Bose gas near the Tonks-Girardeau limit”. *Phys. Rev. A* 72.3 (2005), p. 033619.
- [101] A. Y. Cherny, J.-S. Caux, and J. Brand. “Decay of superfluid currents in the interacting one-dimensional Bose gas”. *Phys. Rev. A* 80.4 (2009), p. 043604.
- [102] H. Castella, X. Zotos, and P. Prelovsek. “Integrability and Ideal Conductance at Finite Temperatures”. *Phys. Rev. Lett.* 74.6 (1995), pp. 972–975.
- [103] X. Zotos. “Ballistic transport in classical and quantum integrable systems”. 126.February (2002), pp. 1185–1194.
- [104] O. Gamayun, O. Lychkovskiy, and V. Cheianov. “Kinetic theory for a mobile impurity in a degenerate Tonks-Girardeau gas” (2014). arXiv:1402.6362.
- [105] O. Gamayun. “Quantum Boltzmann equation for a mobile impurity in a degenerate Tonks-Girardeau gas”. *Phys. Rev. A* 89.6 (2014), p. 063627.
- [106] O. Lychkovskiy. “Perpetual motion of a mobile impurity in a one-dimensional quantum gas”. *Phys. Rev. A* 89.3 (2014), p. 033619.
- [107] X. Zotos. “On the nonlinear response of a particle interacting with fermions in a 1D lattice”. *J. Stat. Mech. Theory Exp.* 2010.12 (2010), p. L12003.

- [108] D. M. Gangardt and A. Kamenev. “Bloch Oscillations in a One-Dimensional Spinor Gas”. *Phys. Rev. Lett.* 102.7 (2009), p. 070402.
- [109] M. Schecter, A. Kamenev, D. M. Gangardt, and A. Lamacraft. “Critical Velocity of a Mobile Impurity in One-Dimensional Quantum Liquids”. *Phys. Rev. Lett.* 108.20 (2012), p. 207001.
- [110] M. Schecter, D. M. Gangardt, and A. Kamenev. “Dynamics and Bloch oscillations of mobile impurities in one-dimensional quantum liquids”. *Ann. Phys. (N. Y.)* 327.3 (2012), pp. 639–670.
- [111] M. Schecter, A. Kamenev, and D. M. Gangardt. “Comment on ”Kinetic theory for a mobile impurity in a degenerate Tonks-Girardeau gas”” (2014). arXiv:1404.4366v1.
- [112] O. Gamayun, O. Lychkovskiy, and V. V. Cheianov. “Reply to ”Comment on ’Kinetic theory for a mobile impurity in a degenerate Tonks-Girardeau gas””” (2014). arXiv:1407.4433.
- [113] M. B. Zvonarev. personal communication. 2015.
- [114] J.-S. Caux. “Correlation functions of integrable models: A description of the ABACUS algorithm”. *J. Math. Phys.* 50.9 (2009), p. 095214.
- [115] M. Kollar and M. Eckstein. “Relaxation of a one-dimensional Mott insulator after an interaction quench”. *Phys. Rev. A* 78.1 (2008), p. 013626.
- [116] A. Faribault, P. Calabrese, and J.-S. Caux. “Bethe ansatz approach to quench dynamics in the Richardson model”. *J. Math. Phys.* 50.9 (2009), p. 095212.
- [117] A. Polkovnikov, K. Sengupta, A. Silva, and M. Vengalattore. “Colloquium: Nonequilibrium dynamics of closed interacting quantum systems”. *Rev. Mod. Phys.* 83.3 (2011), pp. 863–883.
- [118] M. C. Bañuls, J. I. Cirac, and M. B. Hastings. “Strong and weak thermalization of infinite nonintegrable quantum systems”. *Phys. Rev. Lett.* 106.5 (2011), p. 050405.

- [119] J.-S. Caux and R. M. Konik. “Constructing the generalized Gibbs ensemble after a quantum quench”. *Phys. Rev. Lett.* 109.17 (2012), p. 175301.
- [120] M. Gring, M. Kuhnert, T. Langen, T. Kitagawa, B. Rauer, et al. “Relaxation and Prethermalization in an Isolated Quantum System”. *Science* 337.6100 (2012), pp. 1318–1322.
- [121] M. A. Cazalilla. “Effect of suddenly turning on interactions in the Luttinger model”. *Phys. Rev. Lett.* 97.15 (2006), p. 156403. arXiv:0606236 [cond-mat].
- [122] M. Rigol, V. Dunjko, V. Yurovsky, and M. Olshanii. “Relaxation in a completely integrable many-body Quantum system: An Ab initio study of the dynamics of the highly excited states of 1D lattice hard-core bosons”. *Phys. Rev. Lett.* 98.5 (2007), p. 050405.
- [123] S. R. Manmana, S. Wessel, R. M. Noack, and A. Muramatsu. “Strongly correlated fermions after a quantum quench”. *Phys. Rev. Lett.* 98.21 (2007), p. 210405.
- [124] C. Kollath, A. Läuchli, and E. Altman. “Quench Dynamics and Nonequilibrium Phase Diagram of the Bose-Hubbard Model”. *Phys. Rev. Lett.* 98.18 (2007), p. 180601.
- [125] M. Eckstein and M. Kollar. “Nonthermal steady states after an interaction quench in the Falicov-Kimball model”. *Phys. Rev. Lett.* 100.12 (2008), p. 120404.
- [126] J. Mossel and J.-S. Caux. “Exact time evolution of space- and time-dependent correlation functions after an interaction quench in the one-dimensional Bose gas”. *New J. Phys.* 14 (2012), p. 075006.
- [127] N. Nessi and A. Iucci. “Quantum quench dynamics of the Coulomb Luttinger model”. *Phys. Rev. B* 87.8 (2013), p. 063619.
- [128] D. M. Gangardt and M. Pustilnik. “Correlations in an expanding gas of hard-core bosons”. *Phys. Rev. A* 77.4 (2008), p. 041604.

- [129] M. Cramer, C. M. Dawson, J. Eisert, and T. J. Osborne. “Exact relaxation in a class of nonequilibrium quantum lattice systems”. *Phys. Rev. Lett.* 100.3 (2008), p. 030602.
- [130] T. Barthel and U. Schollwöck. “Dephasing and the steady state in quantum many-particle systems”. *Phys. Rev. Lett.* 100.10 (2008), p. 100601.
- [131] M. Rigol. “Breakdown of Thermalization in Finite One-Dimensional Systems”. *Phys. Rev. Lett.* 103.10 (2009), p. 100403.
- [132] J. Mossel and J.-S. Caux. “Relaxation dynamics in the gapped XXZ spin-1/2 chain”. *New J. Phys.* 12 (2010), p. 055028.
- [133] M. Rigol. “Quantum Quenches in the Thermodynamic Limit”. *Phys. Rev. Lett.* 112.17 (2014), p. 170601.
- [134] J.-S. Caux and F. H. L. Essler. “Time Evolution of Local Observables After Quenching to an Integrable Model”. *Phys. Rev. Lett.* 110.25 (2013), p. 257203.
- [135] O. Gamayun. personal communication. 2015.
- [136] J. B. McGuire. “Interacting Fermions in One Dimension. II. Attractive Potential”. *J. Math. Phys.* 7.1 (1966), p. 123.
- [137] L. Dalcin. <http://mpi4py.scipy.org>.